# Functional Ultrasound Imaging of the Avian Brain

**Dissertation zur Erlangung des akademischen Grades eines Doktors der Naturwissenschaften (Dr. rer. nat.)**


vorgelegt von

Richard Rau

an der

**Universität Konstanz**

Mathematisch-Naturwissenschaftliche Sektion
Fachbereich Physik


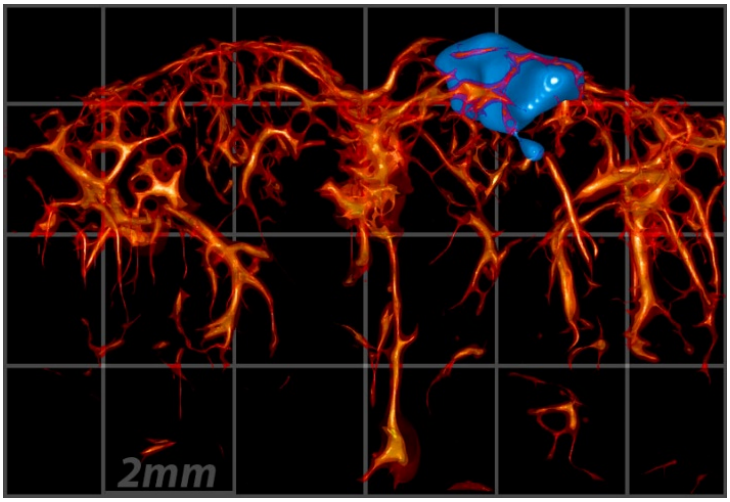


Konstanz, 2017

Tag der mündlichen Prüfung: 20.12.2017

1. Referent: Prof. Dr. Georg Maret

2. Referent: Prof. Dr. Paul Leiderer

# CONTENTS

# 1 INTRODUCTION

The use of sound to obtain information about the internal processes of living organisms dates back to Robert Hooke (1635 - 1703), who extensively contributed to the theory of elasticity and envisioned that

> *'It may be possible to discover the motions of the internal parts of bodies, whether animal, vegetable, or mineral, by the sound they make; that one may discover the works performed in the several offices and shops of a man's body, and therby [sic] discover what instrument or engine is out of order, what works are going on at several times, and lie still at others, and the like.'* [1]

Many animals, such as bats and dolphins, use reflections of emitted sound to locate objects, which is the key principle for any ultrasound imaging method. However, a technical implementation of ultrasound was long in coming and first emerged at the end of World War I with C. Chilowsky and P. Langevin, who realized echo ranging in water with piezoelectric materials for transducers[1].

The early stages of medical echo sonography evolved in 1942, when neurologist K. Dussik first attempted to obtain information about the human skull with ultrasound[2]. Later, in the early 1950's, the research of medical ultrasound applications gained popularity with detection of soft tissue layers, tumors and heart structures[3–5]. The first system to study blood flow was suggested in 1957, where it was proposed to use the Doppler shift in frequency of a continuous ultrasound wave transmission to discriminate static from dynamic scatterers[6]. To obtain information about the depth of the vessels, the continuous wave approach was redeemed in 1970's by pulsed wave systems[7,8] evaluating the inter-pulse dynamics of the scatterers. This principle of pulsed waves is still the basis for most current imaging modalities in Doppler ultrasound.

In the following years the ultrasound research was focused on improving the image quality and processing speed, to facilitate diagnostic ultrasound imaging at a large scale (see Fig. 1). A substantial step was achieved about a decade ago by moving the image reconstruction processing step from the hardware to the software[9]. This enabled computing the delay times of plane wave ultrasound echoes on one or more graphics processing units (GPU), facilitating high frame rate imaging[10].

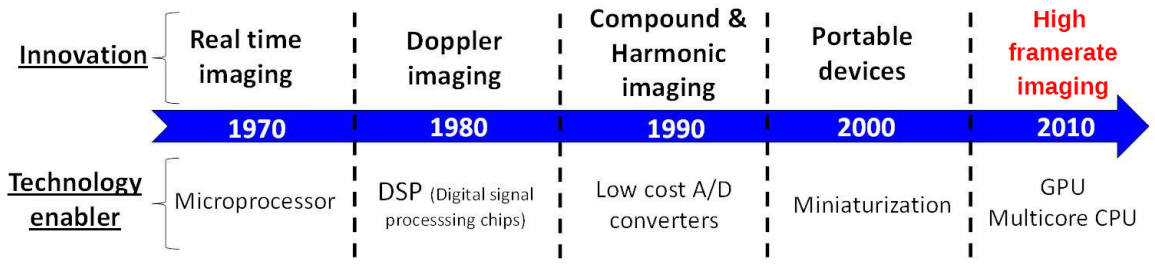


***Figure 1 | Timeline of Ultrasound Imaging***

*The simplified timeline for ultrasound imaging in the past 50 years indicating the technology that enabled novel innovations. A substantial step was taken around 2010 when ultrasound imaging was pushed to high frame rates. Image adapted from [9].*

In the context of Doppler ultrasound, high frame rate imaging allows to resolve the microvasculature inside the brain of small animals[11] and it was first shown in 2011 that the high spatiotemporal resolution of this novel imaging method enables monitoring of the local blood volume changes due to neural activation inside specific brain areas of rodents[12]. This method has been named functional ultrasound (fUS).

Compared to the gold standard of functional neuroimaging, functional magnetic resonance imaging (fMRI), fUS offers an enhanced spatiotemporal resolution of $(100\mu m)^2$ approximately every second. In fMRI, the resolution values depend on a range of intrinsically connected parameters, such that a similar spatial resolution to fUS can only be achieved with a compensation of impaired temporal resolution or field of view[13,14]. Typical numbers in fMRI are voxel sizes of $mm^3$ every few seconds[15]. In addition, fMRI exhibits a comparably low signal-to-noise ratio (SNR), such that averaging over several stimulations becomes necessary and recording of transient events challenging[16].

Thus, fUS imaging offers enormous potential in the field of neuroimaging and, since it was first proposed in 2011, has led to several interesting studies, investigating the somatosensory[12,17–21], visual[22] and olfactory[23,24] system of rats/mice along with discussions on functional connectivity[17,19], epilepsy[12,25] and awake measurements[19,21,25]. Very recently, the method's potential was furthermore demonstrated on humans, revealing different sleep states in neonates[26].

In the context of stimulus related studies, all these notable achievements of fUS have, however, so far solely concentrated on the cerebral dynamics of rodents, even though birds are classical and favorite animal models in a number of neurobiological disciplines. For instance, songbirds are unique subjects because of their similarity to humans in vocal learning[27–29]. Furthermore is the avian visual processing the most popular system for studies on brain asymmetry, due to the bird's unilateral hemispheric dominance, which has a relevance for human developmental disorders[30,31]. Other birds, such as migrating or homing birds, seem to be capable of sensing and processing the earth's magnetic field, which they use for their intriguing peerless navigational skills[32–34]. Yet, it remains unresolved how the bird brain processes this type of information.

In this thesis, it is the objective to discuss the development of an fUS system that is capable of imaging functional responses in the avian brain. To fulfill the necessary requirements for fUS on birds, the acquisition scheme was advanced, leading to a novel implementation of the method, which was termed high definition fUS (HDfUS), pushing the current technology to continuous recording at high frame rates. The discussion in this thesis will concentrate on the technical implementation of HDfUS as well as the capabilities of the method in the context of avian neurobiology. The results presented include studies of the pigeon brain with responses evoked by visual and auditory stimulation as well as of the zebra finch brain solely auditory stimulated. Furthermore, a discussion towards detecting a neural response correlated to the magnetoreception of pigeons is presented.

The thesis is structured to first explain the theoretical background of neural processing in the avian brain as well as of relevant aspects in ultrasound imaging. This is followed by a chapter discussing the experimental setup with a focus on the implementation of HDfUS as well as a detailed evaluation about the influences of different HDfUS settings. In the subsequent results chapter, the HDfUS experiments performed throughout this project are analyzed with respect to the capabilities of HDfUS as a novel neuroimaging method. The implications on future studies of the avian neurobiology are discussed in the respective sections. At the end the results are summarized.

# 2 THEORY

This chapter aims to briefly review the established knowledge of the neural processing in the avian brain and to discuss the theoretical background and current knowledge with respect to fUS imaging. Furthermore, recently proposed findings in high frame rate ultrasound, which enhance the fUS measurements, are outlined.

The chapter is divided into two main parts, t he first discussing the relevant aspects of avian neurobiology and the second of ultrasound imaging.

## 2.1 NEURAL PROCESSING IN THE AVIAN BRAIN

The research field of the avian neural processing is vast and studied by numerous groups. This section only concentrates on aspects of neural processing relevant for this project, more precisely, on the neural characteristics that influence the fUS signal, such as neurovascular coupling, and the important neural pathways.

### 2.1.1 Neurovascular Coupling

Brain activity can be measured in several different ways. With electrophysiological recordings, the variation of the electrical field caused by the ion flow in nerve cells is directly measured. Other methods, such as fMRI or fUS, measure the brain activity indirectly by recording changes in the cerebral hemodynamics, which makes use of the fact that a coupling exists between the neural activity, metabolism and hemodynamics (blood flow, volume and oxygenation)[35]. This interaction is generally termed neurovascular coupling and is split into a parametric and physiological perspective, which are schematically depicted in Fig. 2.

The parametric neurovascular coupling (grey boxes and arrows in Fig. 2) defines the link between neuronal activity and neuroimaging signals,

> *'including characterization of the mathematical relationships between signals, estimation of the hemodynamic impulse response function [...] and the development of comprehensive biophysical models of neurovascular coupling.' [35]*

The physiological neurovascular coupling in turn investigates the involvement and underlying network of the different molecules and cell types (see blue boxes and arrows in Fig. 2).

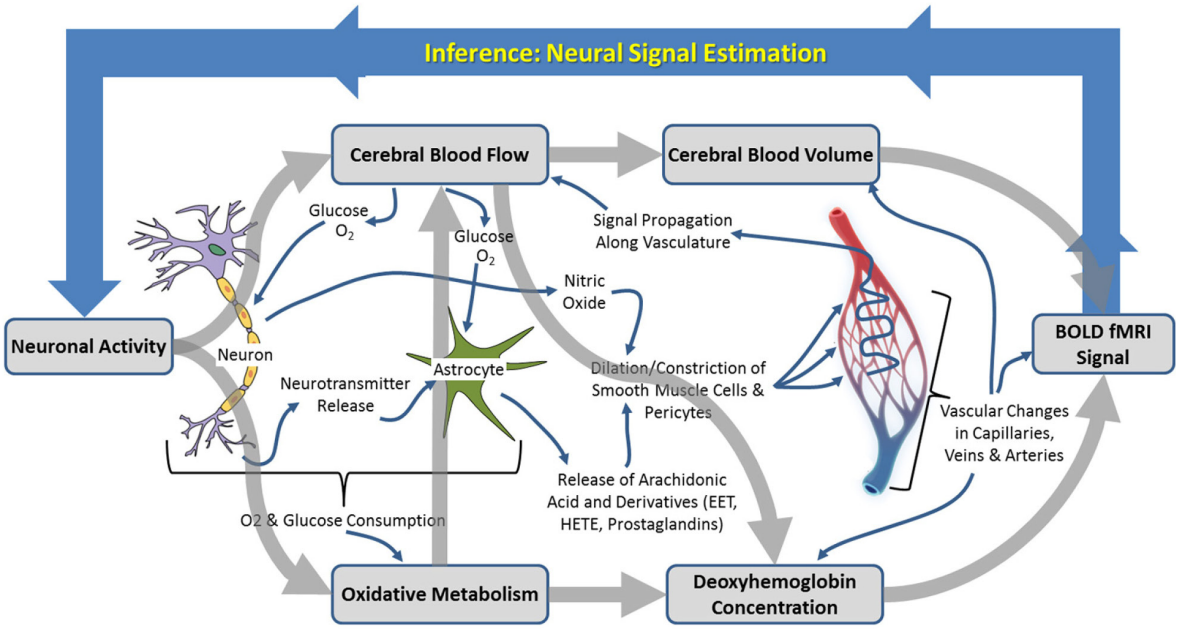


***Figure 2 | Schematic Illustration of the Neurophysiological Processes***

*The boxed processes linked by thick grey arrows represent components of interest to those focusing on 'parametric neurovascular coupling', whereas the more detailed processes illustrated in the center (small blue arrows) represent important concepts for investigation of 'physiological neurovascular coupling'. The relationships between the illustrated biophysical or physiological components, as well as the baseline conditions upon which changes are superimposed, may be mediated by many different factors. Image copied and text modified from [35].*

As can be seen from Fig. 2, the measured neuroimaging signal, here the blood oxygenation level dependent (BOLD) fMRI signal, is influenced by a number of physiological parameters and thus is highly variant[35,36]. Especially anesthetics, which are often used in functional studies, can strongly affect the hemodynamics and lead to deviating responses[37]. Thus, with any neuroimaging method relying on the neurovascular coupling to measure brain activity, it has to be kept in mind that artefactual hemodynamic fluctuation can occur and the experiment has to be designed in a way to take account of it. This is also true for fUS, which measures the cerebral blood volume (CBV) as an indication of neural activity.

### 2.1.2 Neural Pathways

A neural pathway describes the series of connected nerves, which allow to send a signal from one brain region to another. The pathway can consist of white matter, where the connection of neurons is locally distant, or grey matter, which describes a bundle of neurons in a vicinity[38]. Thus, the neural processing of a certain stimulus can be spread over locally separated areas in the brain. In this section, the neural pathways in avian species for visual and auditory input is outlined.

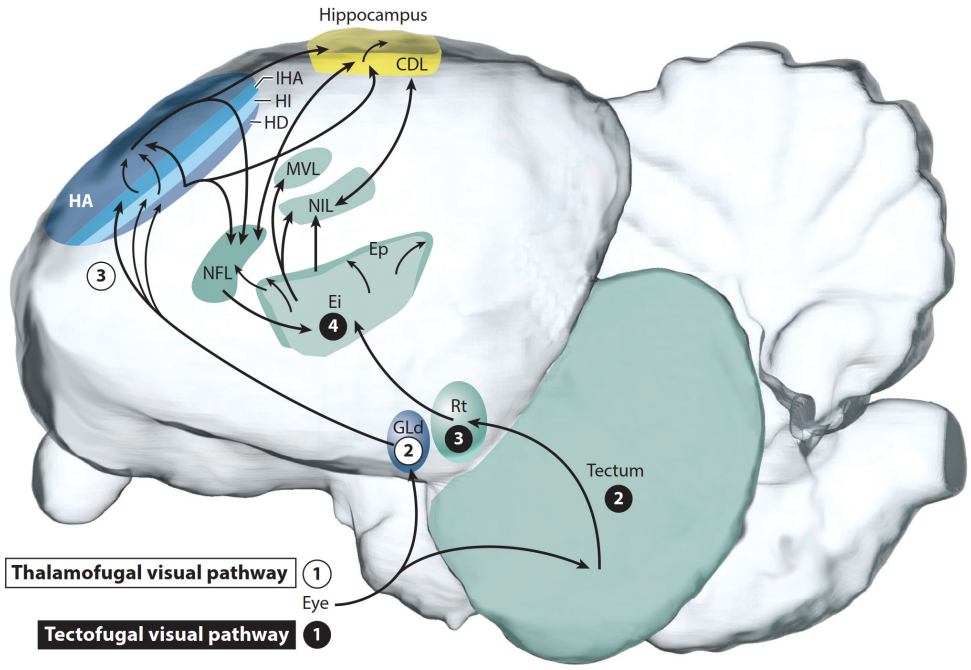


***Figure 3 | Visual Pathways in the Avian Brain***

*The spatial integration of the tectofugal (eye → tectum (TO) → nucleus rotundus (Rt) → entopallium (E)) and thalamofugal pathway (eye →* geniculatus lateralis pars dorsalis *(GLd) → hyperpallium apicale (HA, part of the visual wulst)) in the pigeon brain. Image copied from* [34].

### 2.1.2.1 *Visual Pathways in the Avian Brain*

In birds, vision is a predominant sense. This is reflected by the relatively large size of the eyes compared to the body[39]. In pigeons, the remarkable visual abilities are a 'good detection of static and dynamic stimuli in noise[40], detection of biological motion[41] and other complex motion[42,43], color and UV vision[44–46], and stereopsis[47]'.[48]

The two main pathways in the bird brain that process a visual sensory input are the *tectofucal* and the *thalamofugal* pathway[34]. To comprehend the spatial integration of the areas in the bird brain, see Fig. 3 and Fig. 4.

- The tectofugal pathway is the predominant visual system in the brain and projects the sensory input first to the contralateral optical tectum (TO), passes it along bilaterally to the nucleus rotundus (Rt) and from there to the ipsilateral entopallium (E). The projection to the different areas is asymmetric. This is also termed lateralization and is reflected by an increased number of fibers from the right TO to the left Rt compared to the inverted case[49], as can be seen by the arrow size in Fig. 4. The benefit of concentrating the processing into one hemisphere is believed to result in an enhanced performance in experience based visual tasks, such as object recognition[31].
- The thalamofugal pathway includes the retinal projection to the contralateral nucleus geniculatus lateralis pars dorsalis (GLd) and from there bilaterally to the visual wulsts, which are segmented into four layers from dorsal to ventral[50]. The activation in the

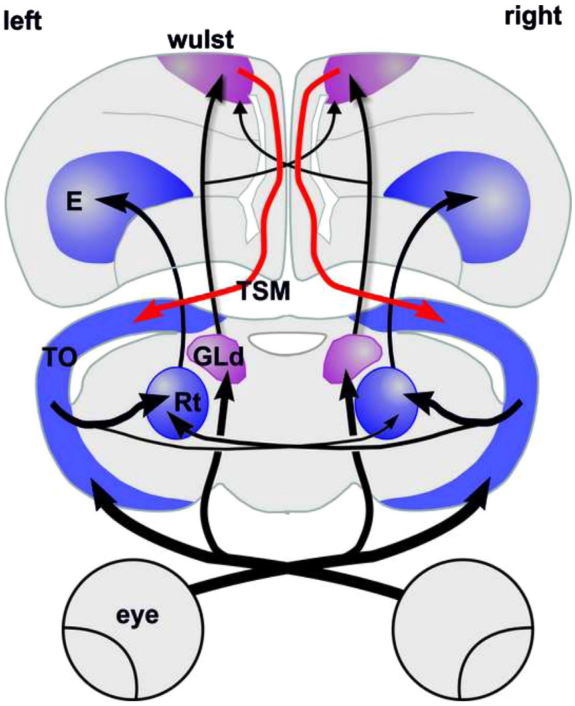


***Figure 4 | Asymmetry in the Visual Pathways in the Avian Brain***
*The spatial integration from the rear view of the tectofugal (eye → TO → Rt → E) and thalamofugal pathway (eye → GLd → wulst) in the pigeon brain. Image copied from [54].*

visual wulst corresponds to a restricted receptive field, laterally centered at about 60° from the beak at rest[51]. This and the vertical organization of the wulst are believed to result in a higher sensitivity to vertical cues[52] compared to the redundant horizontal visual stimulation due to flying and head movement. In the thalamofugal pathway, there is no indication of lateralization[53].

### 2.1.2.2 *Auditory Pathways in the Avian Brain*

The neural processing of an auditory input is – along with vision – another extensive field of research in avian neurobiology. Especially in songbirds, an auditory stimulation is followed by a cascade of activated neural nuclei, which is dramatically different from non-songbirds, such as pigeons (see Fig. 5). The extensive network of interconnected brain nuclei in songbirds is also referred to as song system and involves perception, learning and production of a song[55]. Within songbird species, there are sometimes even seasonal fluctuations of the nuclei sizes or sexual differences, which are ascribed to the fact that male songbirds adapt their song over the course of their lives, whereas females do not[55].

The common forebrain nucleus in all avian brains is the field L, the primary auditory projection region, which is believed to be the equivalent to the auditory cortex in mammals[56]. In songbirds, the principle nuclei responsive to song are the lateral magnocellular nucleus (lMAN), Area X, HVC (letter based name, formerly known as High Vocal Centre) and the robust nucleus of the arcopallium (RA). A detailed review on the neural mechanisms of birdsongs can be found in [55].

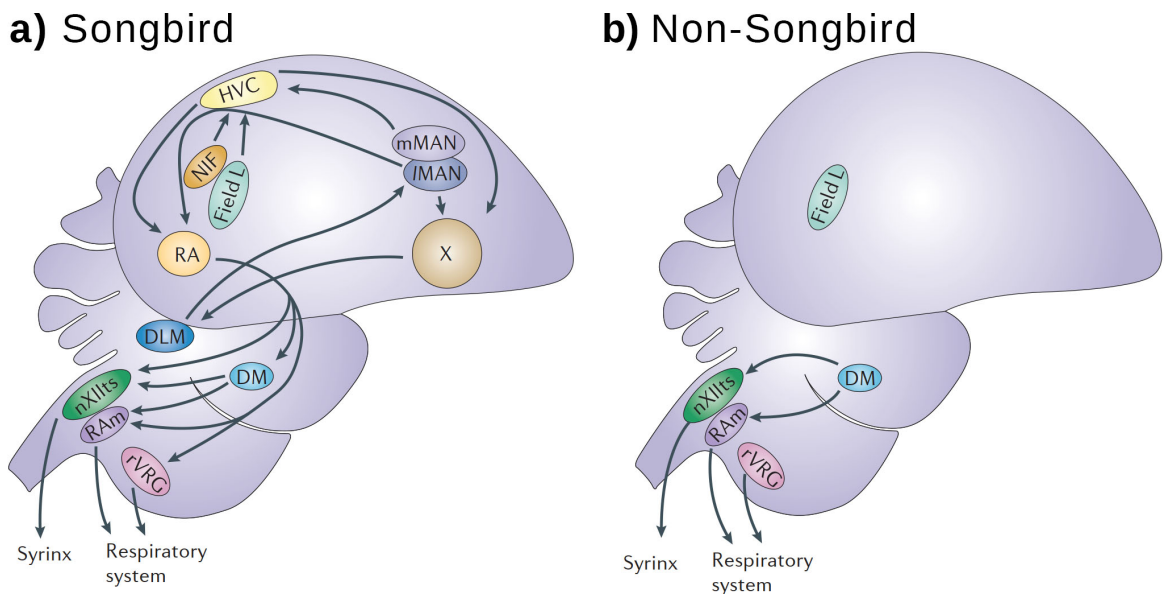


***Figure 5 | Auditory Pathways in a Songbird and a Non-Songbird***

*These schematic diagrams of parasagittal views of the brains of a songbird (**a**) and a non-songbird (**b**). Songbirds have an elaborate network of interconnected forebrain nuclei that form an interface between auditory input (which converges on field L, the primary auditory projection region in the avian forebrain) and vocal output, which is produced in the syrinx, the avian vocal organ. Non-songbirds also have field L, and they can produce vocalizations in the syrinx, but they do not have the network of forebrain nuclei that songbirds have. DLM, nucleus dorsolateralis anterior, pars medialis; DM, dorsomedial nucleus of the midbrain nucleus intercollicularis; HVC, a letter based name; lMAN, lateral magnocellular nucleus of the anterior nidopallium; mMAN, medial magnocellular nucleus of the anterior nidopallium; NIF, nucleus interface of the nidopallium; nXIIts, tracheosyringeal portion of the nucleus hypoglossus; RA, robust nucleus of the arcopallium; RAm, nucleus retroambigualis; rVRG, rostro–ventral respiratory group; X, Area X. Image copied and text modified from [55].*

### 2.1.3 **Magnetoreception**

Many bird species exhibit intriguing navigational abilities, which is believed to be connected to their capability to sense the earth's magnetic field[34]. This so-called magnetoreception is a controversial field of research and it is not yet understood what physical mechanism is the substrate for this sense. Prominent models for magnetoreception of pigeons are magnetic particles in the beak[57] or the inner ear[58], but also a mechanism based on the formation of a radical pair at the retina was proposed[32]. Finding direct cues for the magnetic particles or molecules responsible for the radical pair formation has proven to be difficult[59], such that other strategies can be more promising.

One approach to determine characteristics of magnetoreception could be to detect the associated brain areas. The idea would be to first localize a response in the brain and draw a conclusion on the whereabouts of the magnetoreceptive sensory organ by determining in which brain area the activation is located. Additionally, deviations in the stimulation pattern or setup could lead to more insightful conclusions. For instance, the radical pair mechanism relies

on the animal to be exposed to a certain light spectrum, which can be controlled in an experiment.

However, finding the associated brain areas is challenging, because the response is expected to be comparably small, due to the fact that magnetoreception is believed to be one of the inferior sensory information the pigeon uses[60]. Furthermore, a good stimulation pattern with a large response has not yet been proposed, such that the optimal parameters still have to be found. Thus, for functional methods with a small field of view, such as electrophysiology, it is cumbersome to detect an activation. fMRI cannot be used either, because it relies on strong magnetic fields itself and no defined magnetic field stimulus can be set.

Functional ultrasound could prove to be a very promising method in detecting the magnetoreception associated brain areas, as it offers functional recordings of a large field of view with excellent spatiotemporal resolution (see section 2.2). A detailed discussion on brain areas and neural pathways possibly associated with magnetoreception can be found in [34] and serve as a starting point to look for functional responses.

A profound discussion about magnetoreception and possible imaging techniques can be found in [59] and [60].

## 2.2 Ultrasound Plane Wave Imaging

Recently, it has been shown that images of the microvasculature inside the brain can be obtained through high frame rate Doppler ultrasound imaging for small mammals such as rats[11,61,62]. The revolutionizing aspect about these findings lays within the utilization of plane wave insonifications as an acquisition protocol. Where conventional ultrasound imaging needs numerous acquisitions to reconstruct the whole imaging field of view, the new plane wave method only needs a few recordings. In this section, the principal theory and the resulting imaging possibilities of this new method are discussed.

### 2.2.1 Ultrasound Background

Ultrasound is defined as sound with frequencies above the audible spectrum for humans, which lies approximately at a frequency $f$ = 20kHz. The frequency describes the rate at which a volume within a medium oscillates in its compression and decompression in time. The characteristics of the medium play a crucial role in the propagation characteristics of the longitudinal wave. For gases and fluids the main parameter is the bulk modulus, which defines the magnitude of volume change of a material under pressure.

A scattering event of an ultrasound wave propagating through a medium occurs at material interfaces that have a mismatch of the respective acoustic impedances $Z_i$. The reflection coefficient at an interface is described by

| Material | Speed of sound [m/s] | Acoustic impedance [$10^6$ kg/($m^2$s)] |
|---|---|---|
| Air (0°C) | 330 | 0.0004 |
| Water (25°C) | 1550 | 1.48 |
| Bone | 2700-4100 | 3.75-7.4 |
| Fat | 1440 | 1.37 |
| Blood | 1570 | 1.61 |
| Neurons | 1540 | 1.59 |

***Table 1 | Speed of Sound and Acoustic Impedance for Different Materials***

*The table displays the speed of sound and acoustic impedance values for different materials. For biological matter, the values are only vaguely precise, since it varies with the individual, temperature and location/organ of the body[63,64].*

$$R = \frac{I_R}{I_I} = \frac{Z_1 - Z_2}{Z_1 + Z_2} \tag{1}$$

with the reflected intensity $I_R$ of an emitted ultrasound beam $I_I$. The acoustic impedance is obtained by the product $Z_i = \rho_i c_i$ of the density $\rho_i$ and the speed of sound $c_i$. In Table 1, the speed of sound and acoustic impedance values are listed for relevant media, which reveals two practical challenges for soft tissue imaging: First, imaging objects beneath a bone layer and second, air bubble inclusions within the imaging plane. The large discrepancy in acoustic impedance between soft tissue and air or bone results in strong backscattering amplitudes, such that imaging beneath and around is impaired due to low transmission and/or high reverberations.

A second key point to consider in ultrasound imaging is the relation between spatial resolution and attenuation. High frequencies result in small wavelengths, i.e. enhanced spatial resolution, but reduce the penetration depth due to attenuation. The attenuation transfer function $H(f, z)$ is described by[5]

$$|H(f,z)| = \exp\big(-(\alpha z + \beta f z)\big) \tag{2}$$

where the sound intensity at depth $z$ is exponentially attenuated with the frequency dependent term $\beta$ and independent term $\alpha$.

Along with a better spatial resolution, an increased center frequency of ultrasound has another advantage in blood flow imaging. Due to the small size of the erythrocytes (~5µm) compared to the ultrasound wavelength (λ > 80µm), the scattering is in the Rayleigh regime, where the scattering cross section increases with the fourth power of the frequency[5].

To conclude, selecting the optimal frequency strongly depends on the imaged object. The approach is usually to increase the frequency as much as possible while maintaining the necessary penetration depth for the relevant field of view. For pigeon or rat brain imaging, a center frequency of around 15MHz has proven to be successful[11], which results in a spatial resolution of around 100µm.

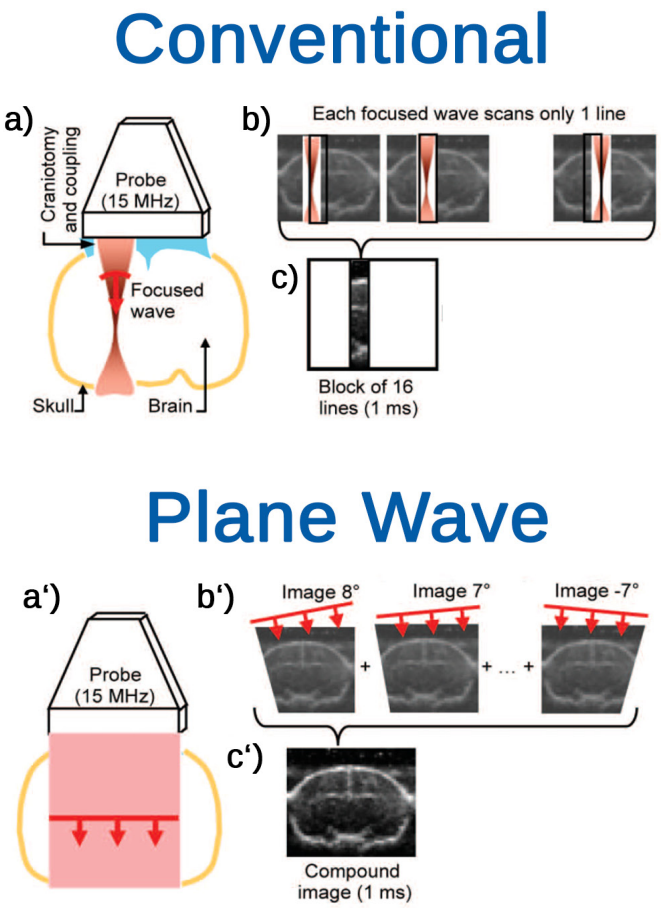


***Figure 6 | Conventional vs. Plane Wave Imaging Schematic***
***a/a')*** *Schematic of the linear array architecture of the ultrasound probe (transducer) with a focused/plane wave transmission into the brain tissue.* ***b/b')*** *The acquisition of several lines/angled plane waves.* ***c)*** *High resolution subimage from 16 focused lines vs.* ***c‘)*** *high resolution full image from coherent compounding of angled plane waves. Both high resolution images are acquired in 1ms. Image copied from* [11].

### 2.2.2 Plane Wave Imaging Basics and Beamforming

As stated at the beginning of this section, plane wave imaging lay the foundation for successful fUS measurements. Typically, ultrasound imaging is performed with a linear array of piezo elements (usually 64-256 channels), that serve in transmit and receive mode (see Fig. 6a/a').

In conventional (non-plane wave) ultrasound imaging, a subset of the elements is used to transmit a pulsed beam with a defined focal depth. Another or the same subset of elements is used to receive the backscattered echo of the pulse (see Fig. 6a-c). With the knowledge of the ultrasound travel time within the medium, the center line insonified by the pulse can be reconstructed. A two dimensional image is then retrieved by scanning through the full field of view line by line.

The approach in plane wave imaging is to insonify the full field of view with all elements simultaneously and reconstruct the image with the knowledge of the travel times (Fig. 6a'-c'). The high resolution is achieved by transmitting and coherent averaging of several angled plane waves to a single image (compounded frame). The intensity map of such a compounded frame is termed B-Mode (brightness mode) image, which directly represents the intensity of the backscattered echoes and allows to detect interfaces in the insonified medium, such as a fetus in the womb.

The image reconstruction of a single plane wave transmission, also called beamforming, is a vivid field of research within the ultrasound community itself. The objective for advanced image reconstruction algorithms is usually an enhancement in image quality and/or computational speed. Depending on the imaged object and setting, both objectives aim to boost SNR, contrast-to-noise ratio (CNR) and/or efficient suppression of artefactual signals, such as reverberations, clutter, etc. In fUS, an elaborate image reconstruction algorithm is of special significance, because a gain in computational performance can drastically increase the imaging quality of the microvasculature as well as fUS sensitivity (see section 2.2.3 and 4.1).

In the following, two image reconstruction algorithms shall be outlined: The classical beamforming approach using delay-and-sum calculations in the time-domain and a faster method acting in the frequency-domain[65] of the echo signals.

#### 2.2.2.1 *Time-Domain Image Reconstruction (Delay-and-Sum)*

The first image reconstruction algorithm of plane waves with a thorough analysis of the image quality enhancement in terms of SNR and CNR compared to conventional methods was published in 2009 for B-Mode imaging[10] and later in 2011 also for Doppler Imaging[61]. The reconstruction is based on a straight forward delay-and-sum calculation of the travel times from the plane wave transmit event via the scattering object to the receive event at a specific channel (see Fig. 7).

To reconstruct the ultrasound echo amplitude of a plane wave with 0° tilt at a given pixel $(z, x)$, the corresponding travel time $\tau$ to the receive channel $x_i$ is calculated

$$\tau(z, x, x_i) = \frac{z + \sqrt{z^2 + (x - x_i)^2}}{c} \tag{3}$$

where $c$ represents the speed of sound in the ultrasonic medium. To make use of the echo signals $RF(x_i, t)$ from all the surrounding receive channels, the travel time, i.e. delay, is calculated for each channel. The ultrasound amplitude signal $s(z, x)$ is then a coherent summation of all the delayed echo signals, such that

$$s(z, x) = \int_{x-a}^{x+a} RF\big(x_1, \tau(z, x, x_1)\big) dx_1 \tag{4}$$

where the aperture $2a$ takes into account only contributing elements. By evaluating $s(z, x)$ for every pixel $(z, x)$ of the plane wave echoes, the image is reconstructed. To improve the resolution, SNR and CNR even further, an image is composed of several angled plane wave transmissions (see Fig. 7c). This results in an image quality similar to the case of scanning though the imaging plane with focused beam lines at the focal spot. Compared to this conventional line scan, the frame rate is enhanced by orders of magnitudes, which is discussed in detail in [10].

The delay-and-sum algorithm is a robust and straightforward solution to reconstruct the image from plane waves, but it is computationally involved, because every image pixel is based on a

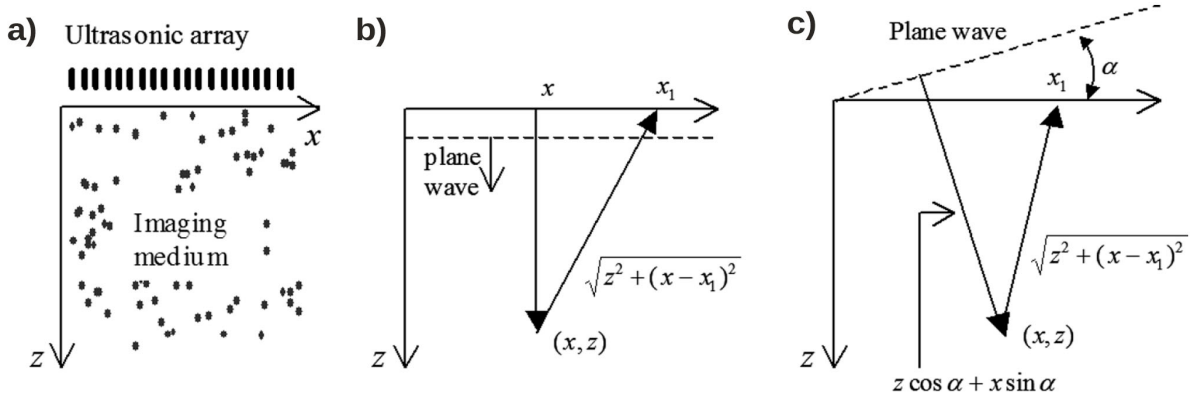


***Figure 7 | Time-Domain Image Reconstruction***

*Schematic representation of the axis convention (**a**) and time delays of plane wave insonifications under no angle (**b**) and angled at α (**c**). Image adapted from[10].*

set of channel data from the echo signals. A computationally faster image reconstruction can be achieved within the frequency-domain of the echo signal[65].

#### 2.2.2.2 *Frequency-Domain Image Reconstruction*

The frequency-domain image reconstruction was first proposed by Lu and coworkers[65,66] and refined by Kruizinga et al.[67]. The idea is to perform a

- 2D fast Fourier transform (FFT) along the temporal dimension (wavenumber $k = 2\pi f/c$, temporal frequency $f$) and lateral component ($k_x = 2\pi/(d_{element})$, distance between elements $d_{element}$)
- Interpolation to an acoustic dispersion grid $k_z = \sqrt{k^2 - k_x^2}$
- 2D inverse FFT

which is depicted schematically in Fig. 8a. The received spectrum $R(k_{tz,rz}, k_{tx,rx})$ consists of the transmitted wave vector $k_T = (k_{tz}, k_{tx})$ and the received wave vector $k_R = (k_{rz}, k_{rx})$ with the dependencies shown in Fig. 8b. To reconstruct the image of the object, the received spectrum $R(k_{tz,rz}, k_{tx,rx})$ is remapped to the frequency grid of the object $O(k_z, k_x)$[67]. For a thorough analysis on the formalism, the reader is referred to the work of Cheng and Lu[66].

Compared to the delay-and-sum algorithm, the frequency-domain image reconstruction is advantageous due to the full axial resolution retention[67] as well as the frame rate gain, because of the computational efficiency of (inverse) FFTs. Furthermore it was shown, that the image reconstruction becomes especially beneficial when the computations are performed on a GPU as pointed out in [67], where a frame rate gain of two orders of magnitudes is achieved compared to the processing on the central processing unit (CPU).

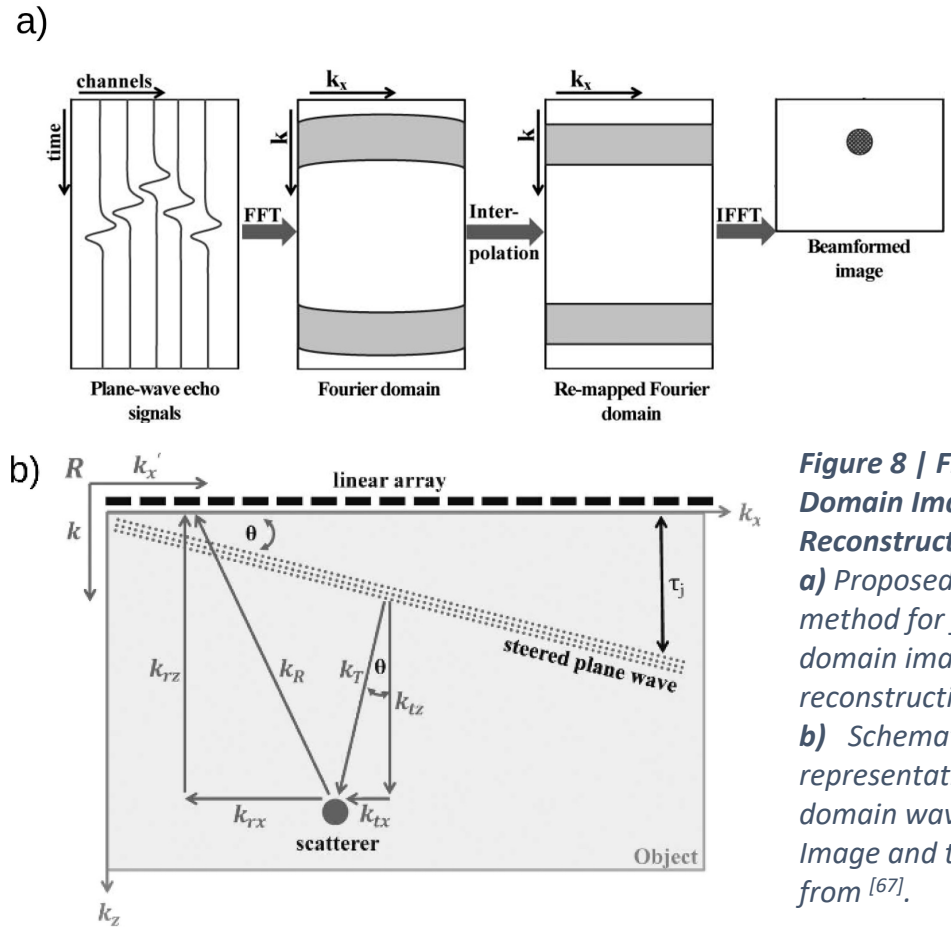


***Figure 8 | Frequency-Domain Image Reconstruction***
***a)*** *Proposed remapping method for frequency-domain image reconstruction[66].*
***b)*** *Schematic representation of the k-domain wave vectors. Image and text modified from [67].*

## 2.2.3 Doppler Imaging: Acquisition

The introduction of plane wave transmissions had a high significance for the Doppler imaging modality in ultrasound. It gave rise to the possibility of resolving microvasculature at a large field of view and extraordinary temporal resolution[11]. To understand why the implications are of such magnitude, it is important to discuss the underlying theory of Doppler imaging. The following derivation is based on [68] and the book chapters 4 and 6 of [5].

The concept of Doppler imaging is based on pulsed wave ultrasound to derive the displacement of a scatterer at a defined depth. The emitted pulsed wave, consisting of $M$ sinusoidal oscillations, is given by

$$e(t) = g(t)\sin(2\pi f_0 t) \qquad (5)$$

$$g(t) = \begin{cases} 1, & 0 < t < M/f_0 \\ 0, & else \end{cases}$$

where $f_0$ denotes the center frequency of the ultrasound. When the emitted pulse is scattered by an object and travels back to the transmit/receive channel in time $\Delta t$, the first receive signal is derived to be

$$r_1(t) = a \cdot e\big(\beta \cdot (t - \Delta t)\big) \qquad (6)$$
$$\beta = \left(1 - \frac{2\mathrm{v_z}}{\mathrm{c}}\right).$$

The attenuation of the emitted pulse amplitude is represented by $a$. The time compression $\beta$ is due to scatterer movement with respect to the propagation direction ($z$) of the pulse. The magnitude of the time compression is only dependent on the axial velocity of the scatterer $v_z = |\vec{v}| \cos\theta$, where $\theta$ denotes the angle between the scatterer movement and propagation direction of the pulse.

The received signal from a consequent second pulse after the time $T_{PRF}$, where PRF stands for pulse repetition frequency, is then

$$\begin{aligned} r_2(t) &= a \cdot e(\beta \cdot (t - \Delta t) - T_{PRF}) \\ &= a \cdot e\left(\beta \cdot \left(t - \Delta t - \frac{T_{PRF}}{\beta}\right)\right) \\ &= r_1\left(t - \frac{T_{PRF}}{\beta}\right) \end{aligned} \qquad (7)$$

which resembles the received signal from the first pulse with a time subtrahend of $T_{PRF}/\beta$. This is further simplified by

$$\begin{aligned} \frac{T_{PRF}}{\beta} &= T_{PRF} \frac{1}{1 - \frac{2v_z}{c}} \\ &\approx T_{PRF}\left(1 + \frac{2v_z}{c}\right) \\ &= T_{PRF} + \tau \\ \tau &= T_{PRF} \frac{2v_z}{c} \end{aligned} \qquad (8)$$

such that (7) becomes

$$r_2(t) = r_1(t - T_{PRF} - \tau). \qquad (9)$$

Designating a relative time scale $t'$, which represents the time between the received signal and the corresponding prior emitted pulse, equation (9) changes to

$$r_2(t') = r_1(t' - \tau). \qquad (10)$$

The only difference in the received signal between consecutive pulses is given through $\tau$. Together with equation (5) and the generalization to any pulse $m$, the received signal can be separated into a constant phase component $\phi_c$ and a variant phase component, which depends on the scatterer dynamics

$$r_m(t') = a \cdot \sin\big(2\pi f_0 (t' - m\tau)\big) = -a \cdot \sin\left(2\pi f_0 \frac{2v_z}{c} T_{PRF} m - \phi_c\right). \quad (11)$$

Thus the received and sampled signal of many consequent pulses oscillates with the frequency

$$f_p = -\frac{2v_z}{c} f_0 = -\frac{2|\vec{v}|\cos\theta}{c} f_0 \quad (12)$$

which resembles the Doppler frequency, but is derived by the inter-pulse dynamics of the scatterers. The use of this phase shift information over a set of samples, which is referred to as the ensemble length $N_e$, is called Doppler imaging and mainly denotes two modes: *Color Doppler* and *Power Doppler (PD)* imaging. In *Color Doppler*, the magnitude of the frequency shift is evaluated, which allows to analyze the direction (i.e. towards or away from the transducer) and velocity of scatterer dynamics. *PD,* in contrast, integrates over the Doppler spectrum, which makes a prediction of flow direction impossible, but maintains the information about the number of scatterers moving within the imaged voxel. Comparing both methods, *PD* is more robust and less prone to signal fluctuations, which makes it more feasible for fUS.

### 2.2.4 Doppler Imaging: Filtering

The challenge in Doppler imaging lies in an effective suppression of the clutter signal. Typically, clutter signal describes the direct echoes and reverberations from objects that have a high scattering amplitude, which is roughly 30dB larger than the blood signal, depending on the ultrasound frequency[69]. The contribution is generally static or has comparably slow dynamics due to a relative movement of the transducer to the object. In fUS, the slow dynamics are caused by breathing and/or movement of the animal. To filter out the clutter signal, a linear high pass filter, such as a Butterworth[12], can be applied with a frequency threshold of around 70Hz, which corresponds to movements of a few mm/s, depending on the angle and center frequency (cf. equation (12)).

The issue with a high pass filter is that it also filters out contributions from very small vessels (i.e. capillaries), where the blood motion is within the same vicinity of dynamics as the animals global motion. Those capillaries, however, are also regulated by the neurovascular coupling and thus contribute to the functional response[70], which fUS aims to measure.

A more sophisticated clutter suppression for Doppler imaging are the eigen-based filters, such as singular value decomposition (SVD). In the context of plane wave imaging, this approach was proposed by Demené et al. in 2015[69] and is outlined in the following. The principle idea of this filter is to differentiate between a signal which is covariant in time over the whole imaging field, i.e. movement of the whole imaged object, and a signal that is solely locally variant, i.e. blood vessels. Thus, the signal $s$ of a pixel $(z, x)$ at time $t$ can be described to be composed of a clutter ($s_c$), a blood ($s_b$) and an electronical/thermal noise ($\eta$) component

$$s(z, x, t) = s_c(z, x, t) + s_b(z, x, t) + \eta(z, x, t) \quad (13)$$

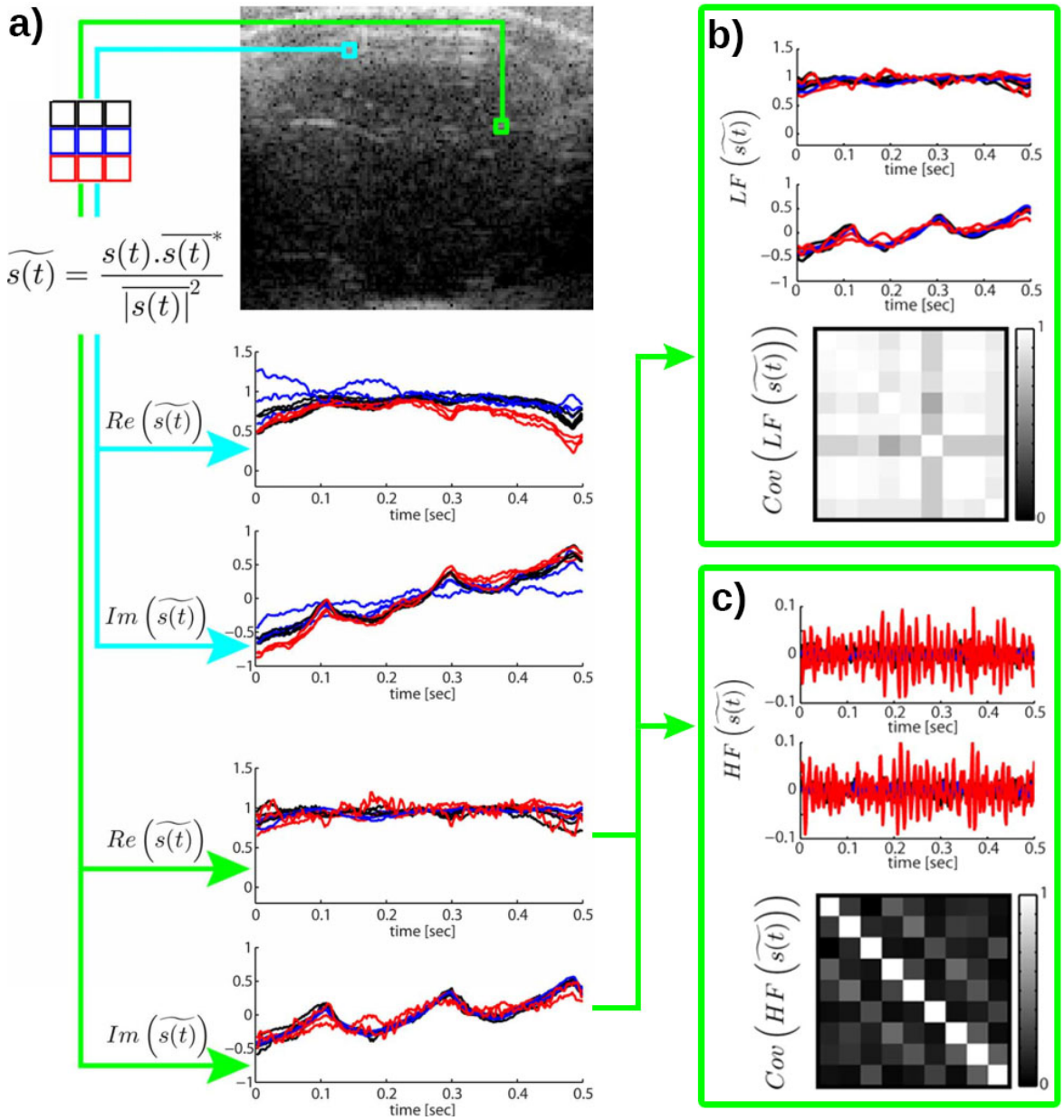


***Figure 9 | Spatiotemporal Filtering for PD Imaging***

***a)*** *A typical plane wave acquisition with a Doppler PRF of 500Hz of a rat brain with thinned skull. The bottom figures give insight on the signal variations in time of two subsets of nine pixels (turquoise and green). The temporal signal variation of the green subset* ***b)*** *low pass filtered (LF) and* ***c)*** *high pass (HF) filtered with a 50Hz Butterworth filter of 4$^{th}$ order. The 9 x 9 covariance matrix (magnitude) of the normalized zero-mean complex signals in* ***b/c*** *show that the LF signal exhibit high covariance, whereas the HF signal is very decorrelated. Image adapted from [69].*

To better compare spatially close temporal signals, a simplified signal is introduced $\tilde{s}(z,x,t) = s(z,x,t).\overline{s(z,x,t)}^* / \left|\overline{s(z,x,t)}\right|^2$, where $\bar{s}$ denotes the time average and $^*$ the complex conjugate. Fig. 9a shows exemplary signal fluctuations of $\tilde{s}(z,x,t)$ in two subsets of 3 by 3 pixels, where a high similarity within each subset is observed. The signal courses and covariance matrices in Fig. 9b/c demonstrate that this similarity is only attributable to the low frequencies

of the signal (i.e. clutter signal $s_c(z,x,t)$) and is not a characteristic of the blood flow contribution $s_b(z,x,t)$. Thus, by discriminating the signal based on the covariance with the other pixels in the imaged field, the blood flow can be retrieved.

To implement the SVD filter for Doppler ultrasound, the signal $s(z,x,t)$ has to be reshaped in a 2D space-time matrix $\mathbf{S}$ of size $(n_x \cdot n_z, n_t)$, where the dimensions describe the spatial number of samples $n_x$ and $n_z$ and the temporal samples $n_t$. The SVD of this so-called Casorati matrix consists of finding the three matrices, such that

$$\boldsymbol{S} = \boldsymbol{U}\boldsymbol{\Delta}\boldsymbol{V}^* \tag{14}$$

where the orthonormal matrices $\boldsymbol{U}$ and $\boldsymbol{V}$ correspond to the spatial and temporal eigenvectors of the respective covariance matrices $\boldsymbol{S}\boldsymbol{S}^*$ and $\boldsymbol{S}^*\boldsymbol{S}$ (* being the complex conjugate).

An SVD of a matrix $\boldsymbol{S}$ can be seen as a decomposition into a weighted, ordered sum of separable matrices[69], such that the diagonal matrix $\boldsymbol{\Delta}$ contains the ordered eigenvalues $\lambda_i$ (singular values) of the outer product $U_i \otimes V_i$

$$\boldsymbol{S} = \sum_{\boldsymbol{i=1}}^{\boldsymbol{rank(S)}} \boldsymbol{\lambda_i} U_i \otimes V_i = \boldsymbol{U}\boldsymbol{\Delta}\boldsymbol{V}^*. \tag{15}$$

In terms of Doppler imaging, the SVD can be seen as a decomposition into separable space and time filters, where each $U_i$ is actually a 2D image of size $(n_x, n_z)$. As outlined above, for tissue displacements (i.e. global motion of the animal) numerous pixels have a similar time profile and thus a high spatiotemporal coherence. This means that those contributions will be mainly described by the first singular values and vectors. Blood signal, on the contrary, has a lower spatiotemporal coherence, such that by adjusting the range of the sum in equation (15), the clutter signal can be filtered out.

The substantial advantage of the SVD compared to a high pass filter is the fact that it discriminates blood flow from global motion by taking account of the temporal characteristics of the signal in the whole field of view. This allows to image the vessels with slow blood flow that would usually be filtered out by a high pass. In Fig. 10b a low pass is applied subsequent to the SVD filter (Fig. 10a), such that only blood flow dynamics < 1mm/s contribute. Clearly, the whole brain is diluted by blood signal, that would be filtered out with a standard high pass filter as can be seen in comparison to Fig. 10d.

On the downside, the SVD filter is - compared to a high pass filter - computationally more complex and cannot be sped up much by GPU processing, because the computing operation are difficult to parallelize. Furthermore, setting the threshold for the tissue/blood transition is challenging to automate. A thorough analysis of the SVD filter formalism, implementation and implications on fUS can be found in [69] and [71].

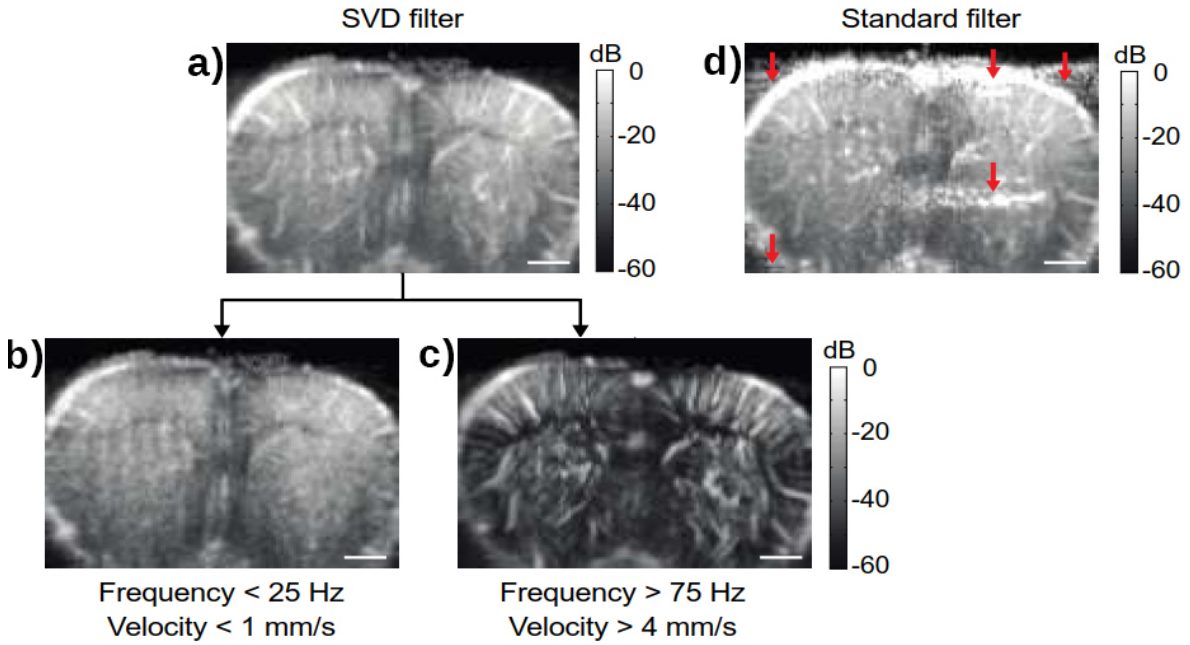


***Figure 10 | High Pass vs. Singular Value Decomposition Filter for Slow Blood Flow***
*The figure shows four images from the same dataset of a rat brain acquired by plane wave imaging. **a)** The Power Doppler image obtained with a SVD filter, which can be divided in a low frequency band (**b**) and a high frequency band (**c**), showing blood in the smaller or larger vessels, respectively. **d)** The Power Doppler image evaluated by a typical 25Hz cut-off high pass filter. The red arrows indicate artefactual clutter signal. The scale bar is 500µm. Image copied from [71].*

### 2.2.5 Plane Wave Imaging: Parameter Settings

In plane wave imaging, a compromise has to be made between frame rate, SNR, spatial resolution and CNR. This section shall serve as an evaluation of the important characteristics and adjustable parameters in plane wave imaging. The discussion is based on two publications, which analyzed plane wave imaging in the scope of B-Mode[10] (Brightness-Mode) and Doppler imaging[61].

In the B-Mode analysis, the lateral resolution, contrast and SNR gain was quantified as indicated in Table 2, where a center frequency of $f_c$ = 4.5MHz was used.

| | Plane wave (1 angle) | Compound (12 angles) | Compound (45 angles) | Compound (71 angles) |
|---|---|---|---|---|
| Lateral Resolution [mm] | 1.8 | 1.1 | 1.1 | 1.1 |
| Contrast [dB] | 12 | 20 | 30 | 33 |
| SNR Gain [dB] | 0 | 11 | 16 | 18 |
| Frame Rate | 100% | 8.3% | 2.2% | 1.4% |

***Table 2 | Image Quality for Different Plane Wave Settings in B-Mode from [10]***

For the Doppler imaging quantification under different plane wave settings, the blood-to-tissue ratio (BTR) is shown in Table 3, where a center frequency of $f_c$ = 5MHz and an ensemble length of $N_e$ = 9 was used.

| | Plane wave (1 angle) | Compound (9 angles) | Compound (16 angles) |
|---|---|---|---|
| BTR Gain [dB] | 0 | 5.8 | 7.1 |
| Frame Rate | 100% | 11% | 6.2% |

***Table 3 | Image Quality for Different Plane Wave Settings in Doppler Mode from*** [61]

The details of the parameters in the two tables will be individually discussed in the following.

#### 2.2.5.1 *Lateral Resolution*

An ultrasound image is obtained through a PSF, which links the object $o(z_1, x_1)$ to the actual image

$$s(z,x) = \iint psf(z,x,z_1,x_1)\, o(z_1,x_1)\, dz_1\, dx_1. \tag{16}$$

The point spread function $psf(z,x,z_1,x_1)$ can be experimentally evaluated by imaging a point-like object (see Fig. 11), such as the cross section of a needle immersed in water. The lateral resolution is represented by the -10dB width of the PSF.

From Table 2 it can be seen that the lateral resolution is impaired for the single plane wave imaging case, but converges already when 12 angled (or even less) are used.

#### 2.2.5.2 *Contrast*

A contrast evaluation is achieved by defining a signal inclusion of diameter $R$ = 5λ around the point scatterer at $(z_1, x_1)$ and compare the average brightness level within the inclusion and the background signal outside the inclusion (see Fig. 11). This is estimated by setting the energy of a PSF outside the inclusion into relation with the total PSF energy.

$$contrast(z_1,x_1) = 10\log_{10}\frac{\iint_{z,x,\notin R} psf^2(z,x,z_1,x_1)\, dz\, dx}{\iint psf^2(z,x,z_1,x_1)\, dz\, dx} \tag{17}$$

Contrary to the lateral resolution, every angled plane wave transmission leads to enhancements of the contrast level (Table 2). Qualitatively, this can also be seen in Fig. 12, where a phantom with several anechoic inclusions is imaged with different numbers of angled plane waves. The reason for the contrast enhancement is the coherent compounding, which smooths out different speckle patterns.

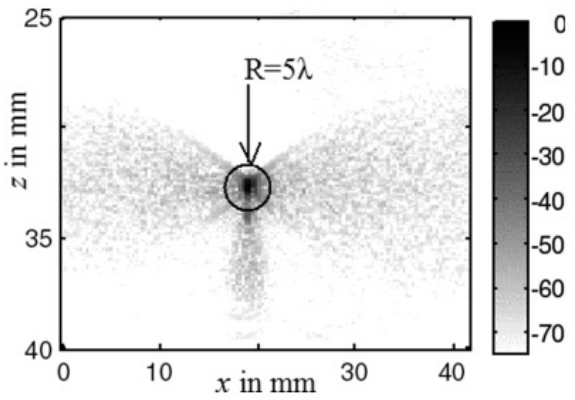


***Figure 11 | Example of an Experimental PSF***
*The color scale in decibels is inversed for the visualization. To measure the lateral resolution the -10dB width is evaluated. For the contrast, the integral of the energy of the lobes outside a circle of 5λ was measured, and divided by the total energy of the PSF. Image copied from [10].*

#### 2.2.5.3 *SNR Gain*

The SNR can be experimentally evaluated by repeatedly measuring a homogenous tissue mimicking object under the same conditions and calculating the ratio of the mean signal $|\bar{s}|$ and its standard deviation $\sigma_s$ at a given pixel $(z_1, x_1)$:

$$SNR(z_1, x_1) = 10 \log_{10} \frac{|\overline{s(z_1, x_1)}|}{\sigma_s(z_1, x_1)}. \qquad (18)$$

In Table 2, the SNR is normalized to the single plane wave transmission case, such that the gain in SNR can be directly evaluated. Similar to the contrast, the SNR gain is increasing when more angled plane waves are transmitted. The reason for the SNR gain is the suppression of electronic noise with every additional plane wave transmission, independent of its angle.

#### 2.2.5.4 *Blood-to-Tissue Ratio Gain*

To estimate the dependency of the PD signal at a given ensemble length on the number of plane wave angles, the blood-to-tissue ratio (BTR) can be calculated from a flow phantom study[61]. In this case the BTR is evaluated as the ratio of PD signal in the center of the flow phantom lumen and the PD signal outside. The gain in BTR is obtained by normalizing the values to the single plane wave case.

From Table 3, it can be seen that a larger number of angles strongly influences the BTR. This is based on the better phase estimation due to the coherent compounding and leads to a better performance of the clutter filter.

#### 2.2.5.5 *Sensitivity with Ensemble Length*

In addition to the above mentioned parameters, the ensemble length is crucial for determination of the right settings. This is especially true in microvasculature imaging, where the PD intensities can be very small due to the slow blood dynamics in the brain of a small animal. To derive the smallest detectable PD intensity $I_{B,min}$, that can be distinguished from the background, a measured signal amplitude of a pixel at $(z, x)$ and time sample $t_i$ after clutter filtering is defined to be

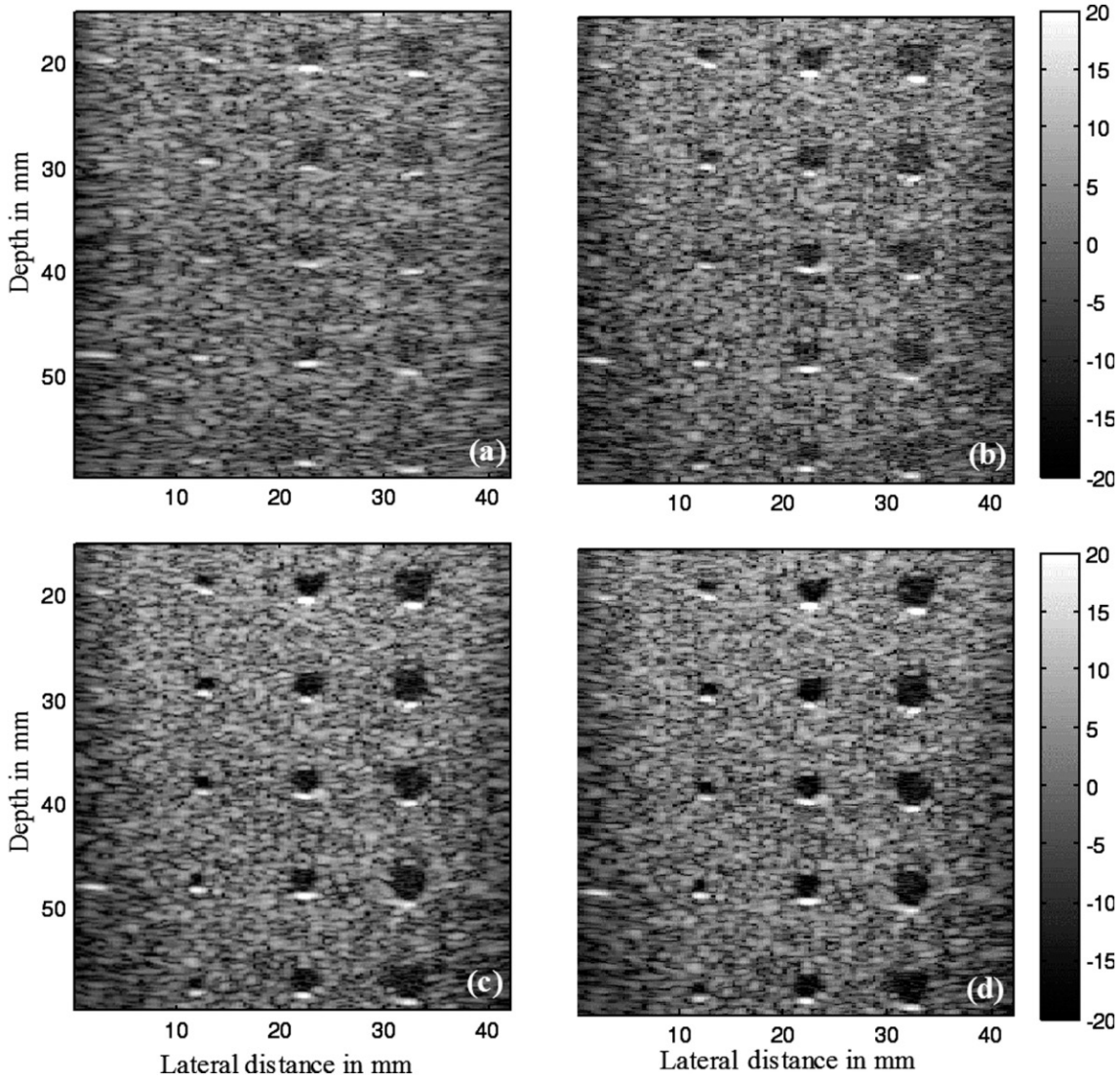


***Figure 12 | Images of Anechoic Objects using Different Numbers of Plane Waves.***
***a)*** *1 plane wave,* ***b)*** *5 plane waves separated by 2° (−4°,−2°,0°,2°,4°),* ***c)*** *21 plane waves separated by 1°, and* ***d)*** *45 plane waves separated by 0.5°. Image copied and text modified from* [10].

$$s(z, x, t_i) = s_B(z, x, t_i) + \eta(z, x, t_i). \tag{19}$$

$s_B(z, x, t_i)$ represents the blood signal and $\eta(z, x, t_i)$ a noise term, which is assumed to be constant over the ensemble length $N_e$. To obtain the PD intensity, the mean signal intensity is computed

$$I(z, x) = \frac{1}{N_e} \sum_{i=1}^{N_e} s^2(z, x, t_i). \tag{20}$$

It can be assumed that $\langle s_B(z,x,t_i)\rangle = 0$ with a variance of $I_B(z,x) = \langle s_B^2(z,x,t_i)\rangle$, such that the measured mean intensity at a pixel is given as

$$\langle I\rangle = I_B + I_\eta. \tag{21}$$

The intensity fluctuates with

$$\sigma_I = \sqrt{\langle (I - I_B - I_\eta)^2\rangle} = (I_B + I_\eta)\sqrt{\frac{2}{N_e}} \tag{22}$$

where $I_\eta$ is the background noise intensity. The lowest detectable blood intensity $I_B$ must be larger than the fluctuations of the measured intensity (i.e. $I_B > \sigma_I$), such that the threshold is given through

$$I_{B,min} = \frac{I_\eta}{\sqrt{N_e/2} - 1}. \tag{23}$$

So, a larger ensemble length $N_e$ enhances the detection capabilities of low blood intensities. Additionally a higher $N_e$ is beneficial for SVD filtering, because it gives more modes to discriminate the blood from the tissue signal (cf. section 2.2.4).

#### 2.2.5.6 *Summary: Plane Wave Imaging Parameter Settings*

In summary of this subsection, finding the right set of parameters in plane wave imaging is rather complex and highly depends on the imaged object. From Table 2 and Table 3 it can be seen that a larger number of angled plane wave images is beneficial in terms of several aspects of image quality. The relative frame rate in the tables, however, shows the drawback. To resolve typical cerebral blood dynamics for small animals (few cm/s), the minimum frame rate is around 1kHz, due to the Nyquist theorem. Taking into account travel times (speed of sound in soft tissue $c$ = 1540m/s) and imaging depths (10 - 20mm in small animal brains), the maximum number of plane wave transmissions for coherent compounding is around 20 – 30. In terms of ensemble lengths typical values range between 100 and 400 to resolve microvasculature.

### 2.2.6 Functional Ultrasound

With plane wave high frame rate imaging, a detection of the microvasculature by PD became feasible and with that, functional imaging. The first functional responses recorded with an ultrasound apparatus were presented by Macé et al.[12] on rats with a whisker stimulation (see Fig. 13a). To localize the activation, the PD signal samples $\mathrm{s(t_i)}$ are typically correlated with the task pattern $\mathrm{A(t_i)}$, by the means of Pearson correlation

$$\mathrm{r} = \frac{\sum_\mathrm{i}\ (\mathrm{s(t_i)} - \bar{\mathrm{s}})(\mathrm{A(t_i)} - \bar{\mathrm{A}})}{\sqrt{\sum_\mathrm{i}\ (\mathrm{s(t_i)} - \bar{\mathrm{s}})^2}\sqrt{\sum_\mathrm{i}\ (\mathrm{A(t_i)} - \bar{\mathrm{A}})^2}} \tag{24}$$

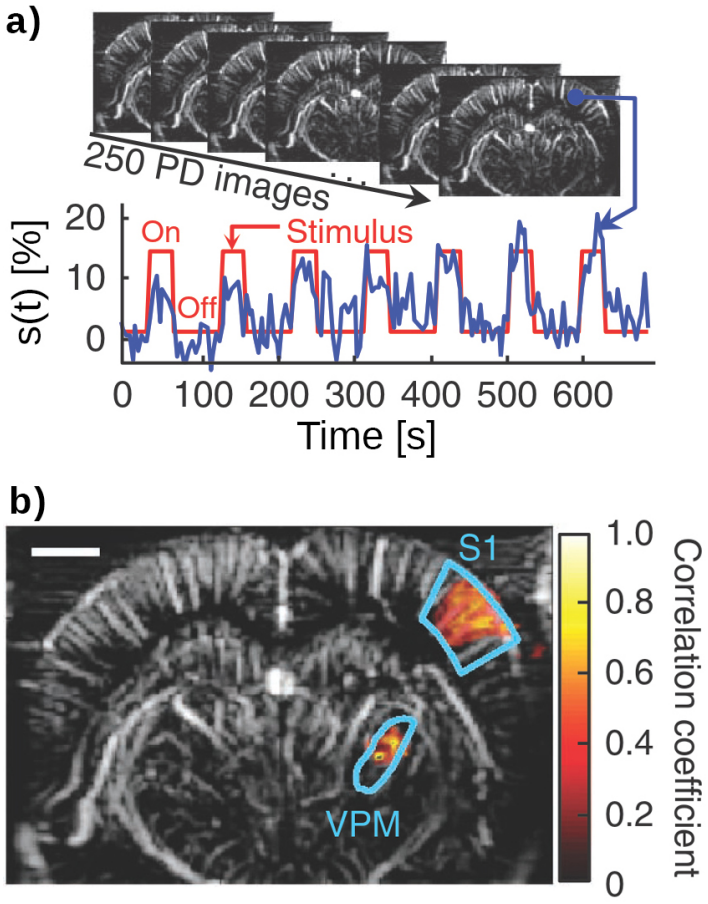


***Figure 13 | Functional Ultrasound Imaging of the Rat Brain***
***a)*** *The series of Power images (grey) acquired every 3s with the relative PD signal shown below (blue) from a region within the barrel cortex. The red line indicates the stimulation/task pattern of whisker stimulation, which correlates with the PD signal changes.* ***b)*** *The PD image (grey) with a colored overlay of the Pearson correlation coefficient map computed over the whole brain slice. The region of activation is indicated by a high correlation coefficient and localized in the barrel cortex (S1) and the ventral posterior medial nucleus (VPM). Image copied from [12].*

where the bar above the coefficients denotes the mean signal. To enhance the SNR of the activity detection, the task pattern $\mathrm{A}(\mathrm{t_i})$ can be matched to the characteristics of the hemodynamic response, which is usually delayed by a few seconds. The threshold value of $r$ that defines an area to be active depends on the general hemodynamic fluctuations and has to be adapted accordingly. Figure 13b shows how the Pearson correlation can be used to localize an activity in defined brain areas.

### 2.2.7 **3D Vascularity**

A detailed 3D image of the microvasculature is of explicit importance for fUS, because it can be used as a neuronavigation. With defined landmarks of major vessels in the small animal brain, an atlas for mapping any 2D fUS dataset could be produced. This would enhance the comparability of the results from different datasets, especially with respect to avian species where the stereotactic coordinates are relatively imprecise[72]. A recent conference proceeding[73] demonstrates how such a neuronavigation with Doppler imaging could be used for rats.

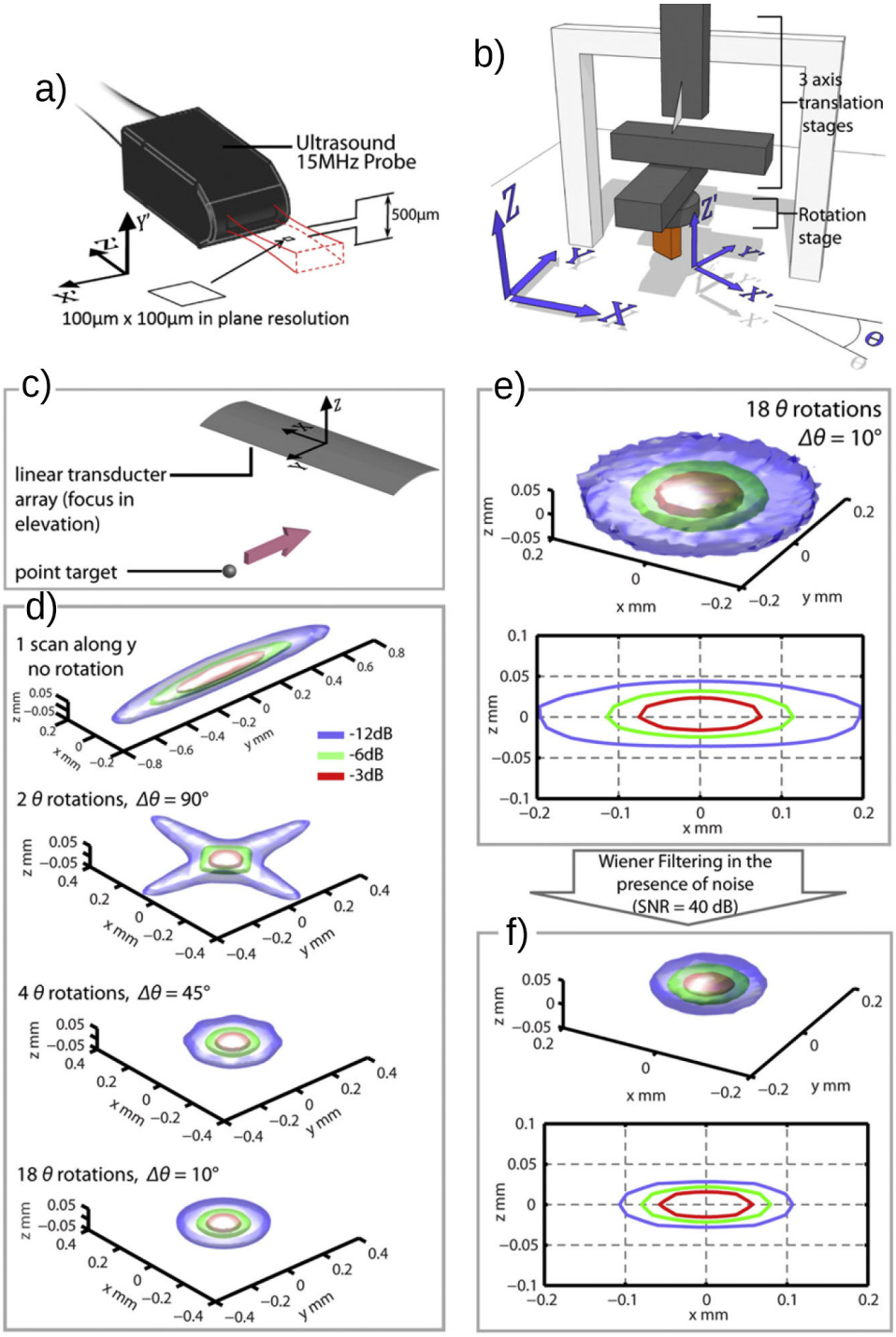


***Figure 14 | 3D Microvasculature Imaging – Setup and Simulation***

***a)*** *1D linear array probe with 15MHz center frequency. The resolution in-plane and out-of-plane are indicated to be 100µm x 100µm and 500µm, which causes the anisotropic point spread function (PSF).* ***b)*** *The ultrafast Doppler tomography setup to produce a 3D volume with an isotropic PSF.* ***c)*** *Simulation model to compute the PSF with a point target moving along the out-of-plane axis.* ***d)*** *Result of the simulation with a rotation of the transducer angle $\theta$. With a larger number of 3D volume recordings, the PSF becomes more isotropic.* ***e)*** *The PSF in all three dimensions for 10 angles acquisitions at $\Delta\theta = 10°$. The -3dB and -6dB width of the PSF in the x-y-plane is 150µm and 230µm respectively.* ***f)*** *Deconvolution with a Wiener filter decreases the -3dB and -6dB PSF widths to 90µm and 135µm, respectively. Image adapted from [74].*

The issue in producing a detailed 3D microvasculature image with a linear array transducer is constituted by the relatively poor elevation (out-of-plane/$y$-) resolution with this architecture (see Fig. 14a). The in-plane ($z, x$) resolution is equal to the wavelength of the transmit beam, which is achieved by angled plane wave insonifications (cf. section 2.2.1). The elevation resolution is however defined by the acoustic lens in front of the piezo elements and typically takes values of a multiple of the wavelength. To eliminate this anisotropy, it was proposed in [74] to mount the transducer to a 4D stage (3 translational, one rotational) and acquire volume datasets under numerous transducer rotations along the z-axis (see Fig. 14b). Thus, the point spread function (PSF) in the $x$-$y$ plane becomes isotropic (Fig. 14c-e) and can be deconvolved to retrieve the wavelength resolution (Fig. 14f). The method was named ultrafast Doppler tomography.

Formally, the problem can be expressed as

$$s(x,y,z) = psf(x,y,z) * e(x,y,z) + \eta(x,y,z) \qquad (25)$$

where $s(x,y,z)$ is the acquired 3D volume and $\eta(x,y,z)$ is a white noise term. The first term on the right side of the equation describes the convolution of the blood scatterer distribution $e(x,y,z)$ and the point spread function $psf(x,y,z)$, which can be evaluated by simulation, if the transducer characteristics are known.

To deconvolve the 3D volume in presence of noise the best approach is the application of a Wiener filter

$$\widehat{W}\left(k_x,k_y,k_z\right) = \frac{1}{PSF\left(k_x,k_y,k_z\right)} \frac{\boldsymbol{S}\left(k_x,k_y,k_z\right) - \sigma^2}{\boldsymbol{S}\left(k_x,k_y,k_z\right)} \qquad (26)$$

where the upper case letters denote the Fourier transform of the variables from equation (25) and the bold characters the energy spectrum. The variance $\sigma^2$ accounts for the noise and is evaluated in an area of the 3D volume without blood.

The retrieved blood scatterer distribution in k-space is then computed by

$$\hat{E}(k_x,k_y,k_z) = \widehat{W}(k_x,k_y,k_z)S(k_x,k_y,k_z) \qquad (27)$$

which can be inversely Fourier transformed into the spatial domain to obtain the blood scatterer distribution $\hat{e}(x,y,z)$ within the 3D volume at isotropic wavelength resolution (see Fig. 15).

A drawback of the ultrafast Doppler tomography approach is that it is comparably time consuming, because a full 3D volume needs to be acquired with several transducer rotations. In [74] the native resolution of (100µm)³ over a volume of 12.8mm x 12.8mm x 20mm for a rat brain was retrieved with 18 rotation and 65 translation steps, i.e. 1170 total transducer positions/images. Depending on the speed of the linear and rotational stages, an ultrafast Doppler tomography takes 20 minutes or more.

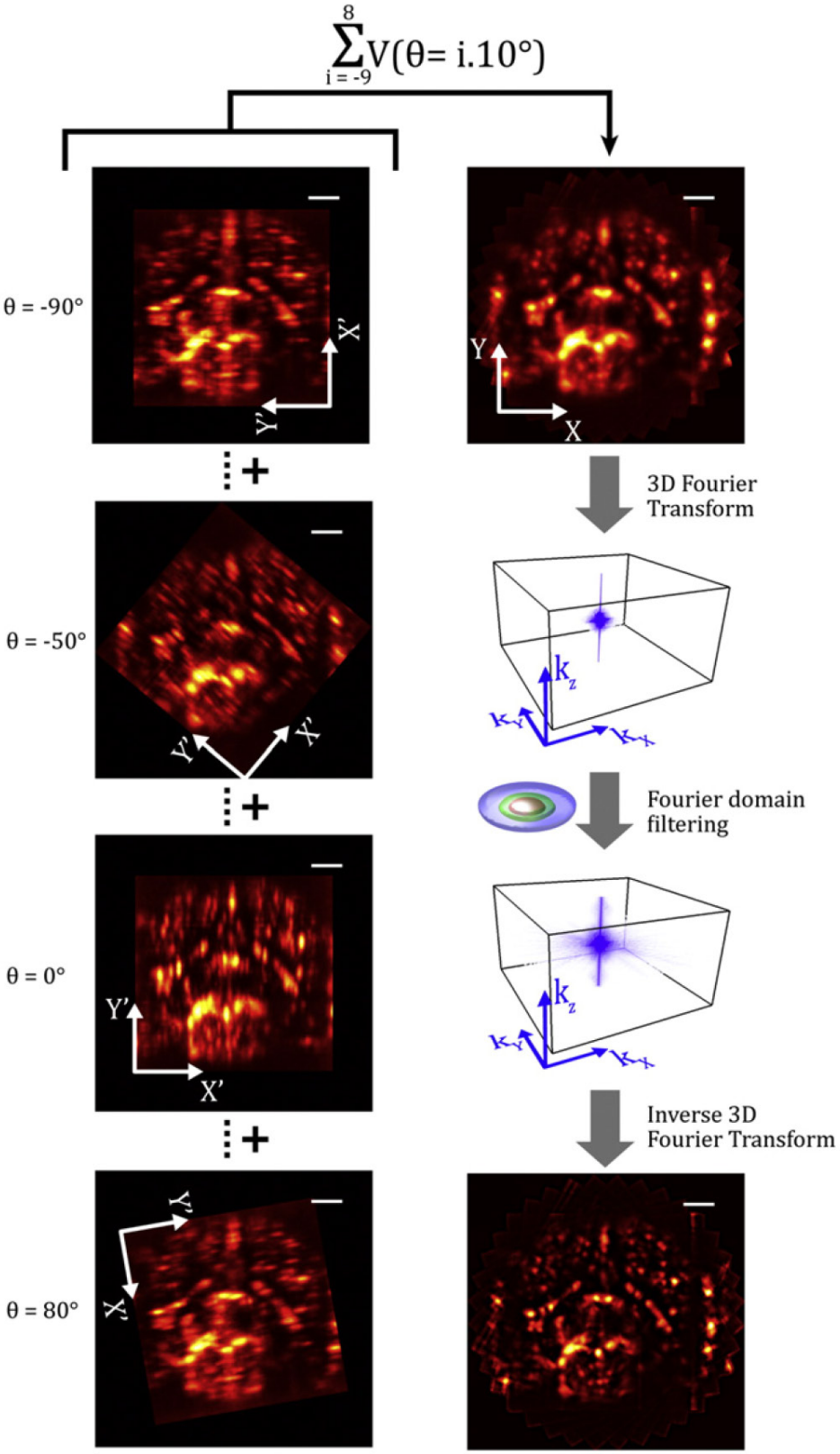


***Figure 15 | 3D Microvasculature Imaging of a Rat Brain***

*The images on the left represent the schematic of a selection of angled 3D volume recordings in an x-y-plane. The top right image is the average of the 18 different angled 3D volume recordings. With the Wiener deconvolution approach, the native in-plane resolution is retrieved, leading to a detailed map of the rat's brain microvasculature. Image copied from [74].*

To produce detailed 3D images faster, the best approach would be to use a 2D array probe. It has to be mentioned that the utilization of those probes is currently a vivid field of research, because with the constant progress in computing performance the processing of a large number of channels becomes feasible. Recent results have shown that 3D Doppler imaging with a 32 by 32 (1024 in total) channel matrix array is possible at a lower center frequency[75]. It is however still very challenging because it requires four costly state-of-the-art ultrasound machines working in parallel. The small dimensions of the piezoelectric elements per channel necessary to produce vascularity images at $(100\mu m)^3$ resolution makes 2D probes not yet feasible. A 2D array containing 1024 channels, for instance, could image a field of about 3mm by 3mm, which is still too small for most brain sizes. With the ongoing progress of computational performance direct 3D brain imaging of small animals will be possible in the near future.

# 3 METHODS

In this chapter, the methods of the experimental setup are described in two parts. First, the experimental preparation together with the stimulation setup are discussed, which lay the basis for the functional ultrasound studies in this project. In the second part, the important aspects about high definition functional ultrasound acquisition (HDfUS) are explained with a focus on software implementation and a detailed discussion about the parameter adjustments.

## 3.1 EXPERIMENT PREPARATION AND SETUP

To perform an fUS study, a few preparations are necessary and an accurately working experimental setup is essential. In this part, all the preparatory operations are explained as well as the stimulation evocation for the animals. The focus is laid on the pigeon (columba livia domestica) setup that was implemented at the University of Konstanz. In each section, the differences to an application of fUS on zebra finches are pointed out.

A general overview of the experimental setup at the University of Konstanz is shown in Fig. 16 with a close up view of a pigeon fUS experiment in Fig. 17. A detailed view on the different components of the setup shown in the two figures will be explained throughout the whole chapter.

In the general overview in Fig. 16, the three Merrit-coil systems (Fig. 16a) represent the frame around the box and facilitate the control of the magnetic field inside the box, where the pigeon is located for fUS studies and. The ultrasound acquisition performed with the Verasonics Vantage ultrasound apparatus (Fig. 16b) and the anesthesia depth is controlled with the isoflurane vaporizer (Fig. 16c). The pulsoxymeter (Fig. 16d) allows to monitor the physiology of the animal and thus the stability of the narcosis. The setup also includes a diffusing wave spectroscopy system[60] shown in the background (Fig. 16e), which measures functional responses based on multiple light scattering in the animal simultaneously to the fUS acquisitions.

The close up view of the experiment in Fig. 17 shows an anesthetized pigeon inside the pigeon box of the three Merrit-coil systems (Fig. 17a) with a fixation of key-and-slot joint holders (Fig. 17b) around a basin that is permanently attached to the pigeon's skull. For fUS measurements, the basin is flooded with ultrasound coupling gel and the tip of the transducer (Fig. 17c) is positioned inside the gel about 10mm above brain surface. The transducer is mounted to a 4D-axis stage for accurate positioning. The LEDs (Fig. 17d) at the side are used for the static lateral

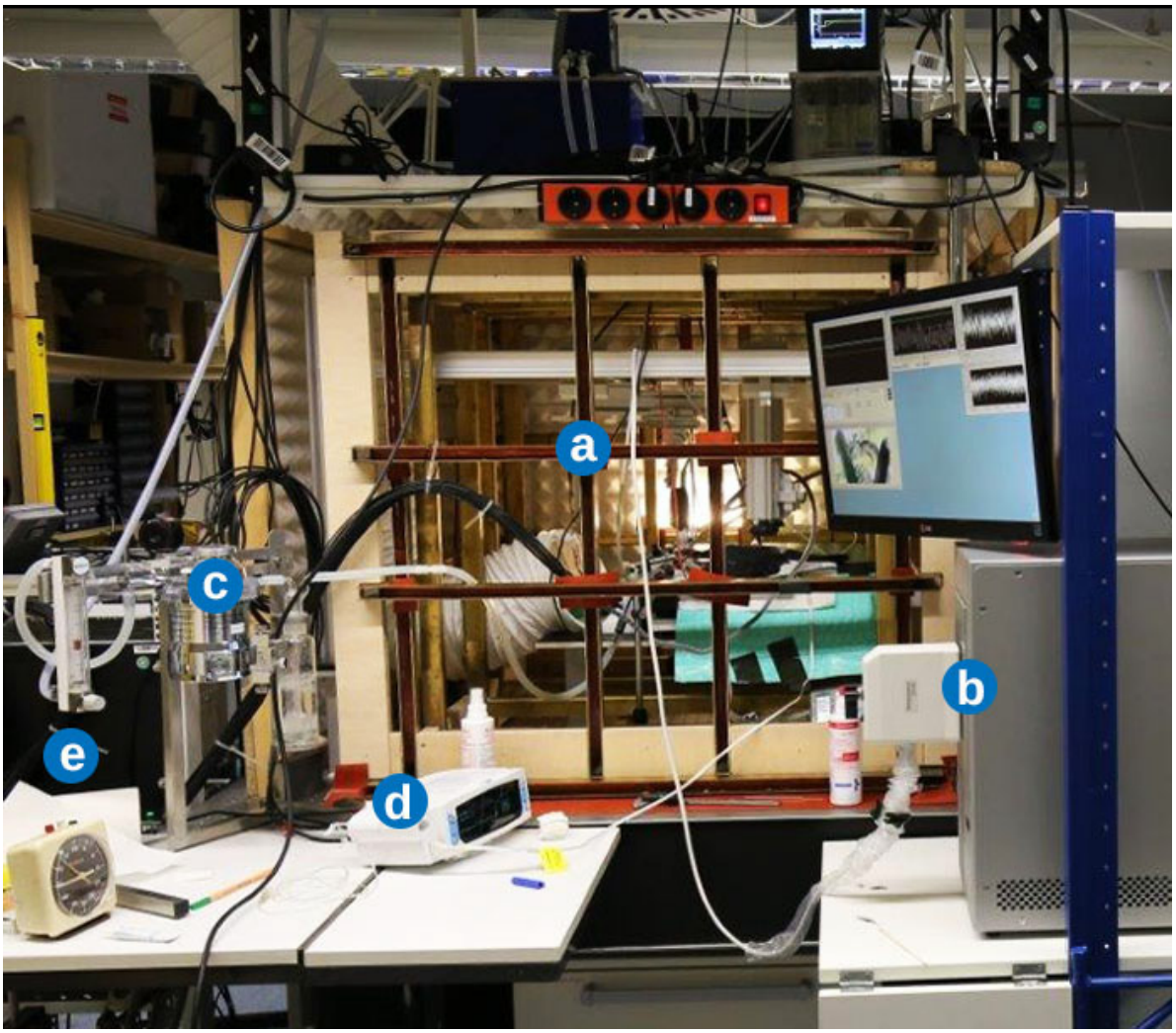


***Figure 16 | Experimental Setup Overview***

*General overview of the setup for the fUS studies.* ***a)*** *Merrit-coil system,* ***b)*** *Verasonics ultrasound apparatus,* ***c)*** *isoflurane vaporizer,* ***d)*** *pulsoxymeter,* ***e)*** *DWS setup. See text for details.*

visual stimulation, the Merrit-coil systems (Fig. 17a) for the magnetic stimulation and two speakers for the auditory stimulation. The anesthesia of the pigeon is administered by an isoflurane flooded half open mask (Fig. 17e) and controlled/monitored with cameras (Fig. 17f), a water perfused heating blanket (Fig. 17g), a thermometer and pulsoxymeter. A microphone is installed at the top of the box to record interfering ambient sound during the measurements.

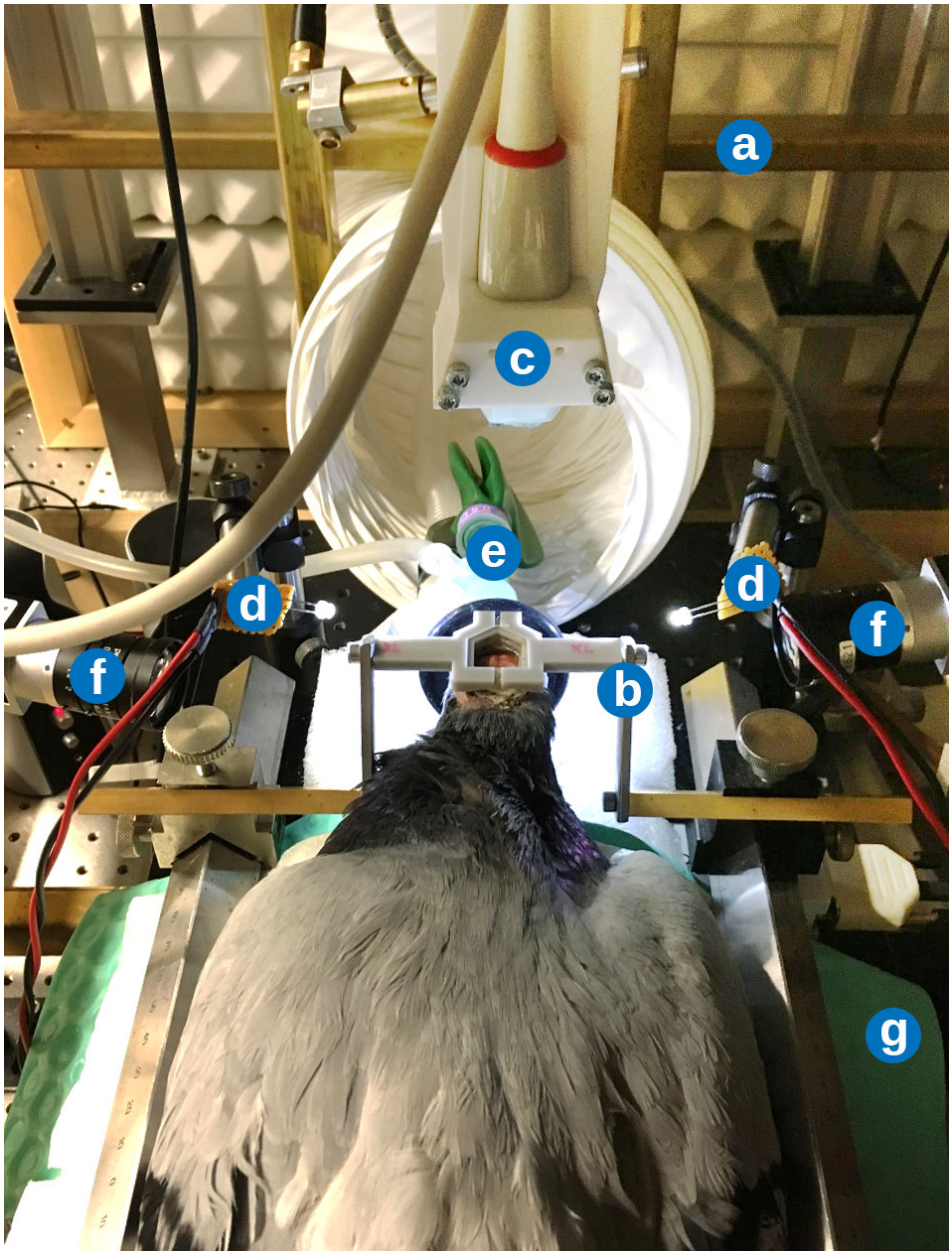


***Figure 17 | Pigeon with Fixation in the fUS Setup***

*A close up view of the setup with an anesthetized pigeon.* ***a)*** *Merrit-coil system,* ***b)*** *key-and-slot joint holders,* ***c)*** *transducer,* ***d)*** *LEDs,* ***e)*** *breathing mask,* ***f)*** *cameras,* ***g)*** *heating pad. See text for details.*

### 3.1.1 **Trepanation**

As discussed in section 2.2.1, the interface between soft tissue and bone or air results in strong backscattering signals of the ultrasound and impairs the detection of the microvasculature beneath. Especially the bird skull anatomy with the sponge-like structure that mainly consists of air cavities (Fig. 18), is not in favor for ultrasound penetration. This results in a number of air/bone interfaces, which exhibit a large acoustic impedance mismatch and thus high

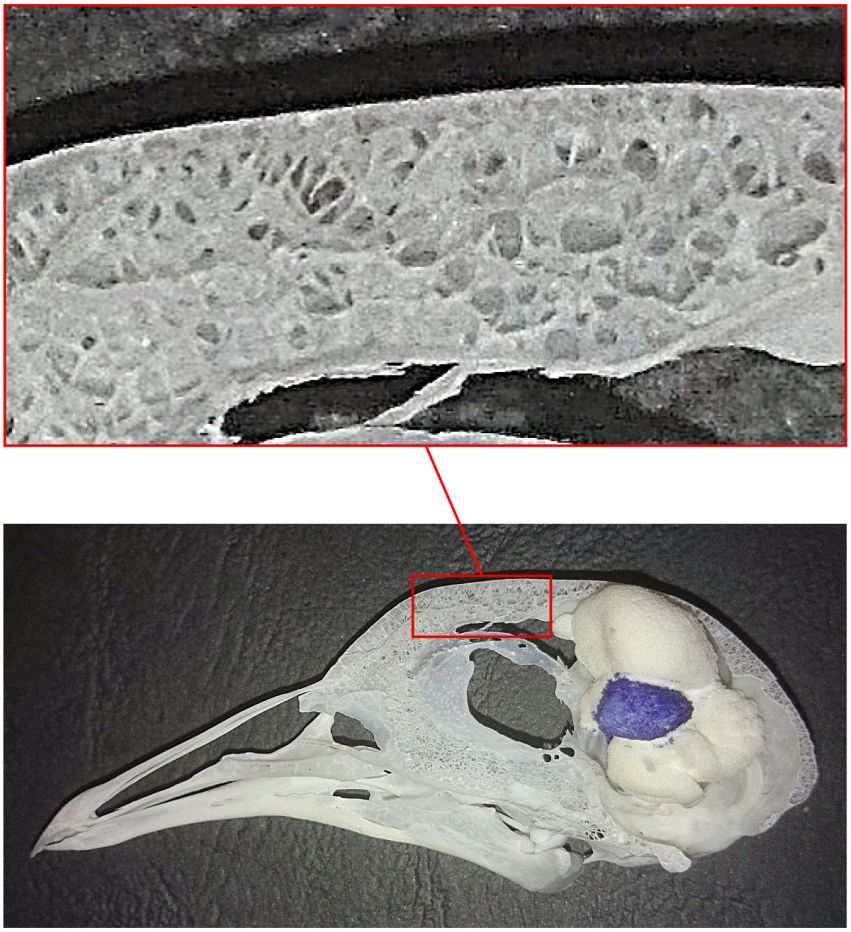

***Figure 18 | Pigeon Skull with a 3D Printed Brain Model***

*Skull of a pigeon (purchased from tierschaedel-online.de) which was cut in half. The upper image shows a zoom into the area marked in red. In the lower image a 3D printed pigeon brain (3D data of pigeon brain atlas from ref. [76]) was inserted into the skull providing better orientation regarding the brain regions. The optical tectum is colored in blue. Image copied from [60].*

reflection coefficients (see equation (1)). The reason for this peculiar anatomy is reduced bodyweight and hence less energy consumption while flying.

Compared to most fUS measurements on rats[12,17,19], a full craniotomy is not necessary for pigeons or zebra finches. The last layer of bone (a few 100µm thick) attached to the dura impairs the ultrasound penetration only partially and a sufficient detection of the microvasculature is given. The advantage of leaving the bone to some extent intact is that several experiments can be carried out over weeks with the same animal. There is also no need for sacrifice, because the skull regrows and the animal can be released after recovery. During the time of healing and skull regrowth it has to be ensured that the animal does not hurt itself at the trepanation area, which can be accomplished by installing a protective custom made basin.

To perform the surgery, a detailed protocol is provided in [60]. In the following, the procedure is summarized with some optimizing modifications about the basin design and trepanation size.

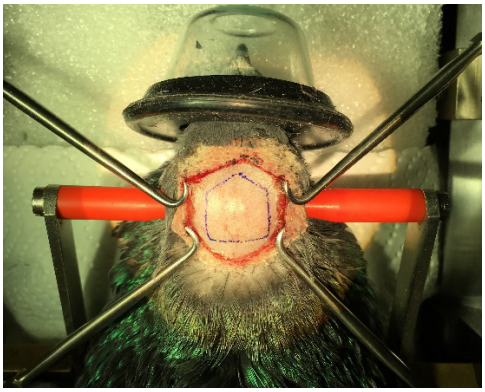

A medial skin incision of about 25mm from rostral to caudal is performed to open the regio frontalis area. To prevent infections, the feathers are removed around the incision. The blue lines mark the size of the basin of around $(14mm)^2$ to be installed on the skull.

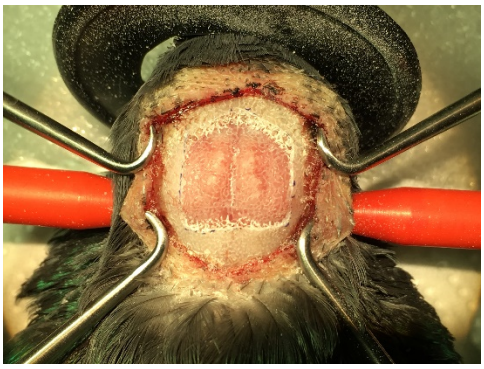

The marked area is thinned with a microdrill (Proxxon 50/E, Föhren, Germany) and the last layer of bone is left intact. The edges reveal the cavities in the bone.

The custom made 3D-printed basin is installed and fixated with dental cement (Harvard Cement normal setting, Harvard Dental International GmbH, Hoppegarten, Germany). The surrounding skin is also embedded in the cement to prevent infections.

A slide-in plate is used to close the trepanation area and to prevent injuries. For fUS measurements the plate is taken out and the basin filled with ultrasound coupling gel. It is important that the plate fits tightly in the slit, such that it cannot fall out with strong head movements or manipulation.

For pigeons, the installed basin was found to stay up to eight weeks without the need for further surgery. After this period, the basin falls off and the skin opening grows together over the course of a few weeks. Once the pigeon is fully recovered, it can be released to the loft. Up until then it is kept isolated in a separate large cage to protect it from potential aggressive behavior of other pigeons. In total, four pigeons were studied with this novel type of installed basin.

For the zebra finch study, the basin was resized to fit the smaller anatomy of the bird. Because those experiments were final, no conclusion can be drawn about the stability or lifetime of basin installation on the head. Only one zebra finch was studied in this project with this type of basin.

### 3.1.2 **Anesthesia**

To prevent unexpected complications in the surgery and fUS measurements, controlling the narcosis depth is crucial. For pigeons, the narcosis depth is strongly correlated to the physiology and thus, constant monitoring and/or control of the animal's temperature, breathing rate, heartrate and movement is essential. To achieve a stable anesthesia, the following equipment was implemented in the setup:

- **To control the isoflurane concentration,** an Eickemeyer Anesthetic Unit Research (Eickemeyer, Tuttlingen, Germany) is used (Fig. 16c). The isoflurane is administered to the animal through a half open mask (Fig. 17e) with a constant pure oxygen flow.
- **To monitor the heartrate and oxygen saturation** at the distal M. gastrocnemius of the animal**,** a SurgiVet V90041 pulsoxymeter (Smiths Medical PM, Inc., MA, USA) is used.
- **To monitor the temperature,** a Voltcraft Multi-Thermometer DT-300 (Conrad Electronic AG, Wollerau, Switzerland) is placed in the rectum of the animal.
- **To control the temperature,** the animal is placed on a Gaymar T-Pump Mul-T-Pad heating pad (Gaymar Industries Inc, NY, USA) connected to a Huber CC-104A thermostat (Peter Huber Kältemaschinenbau AG, Offenburg, Germany). Some animals had a more pronounced temperature drop during anesthesia, such that the surrounding air temperature was additionally increased with a conventional fan heater.

Furthermore, the breathing rate should be observed by the experimenter by looking at the slight movements of the beak and body.

Compared to pigeons, controlling the anesthesia is less involved for the zebra finches. In this case, a stable narcosis was maintained with isoflurane and a heating pad, but a constant monitoring of the parameters was not necessary.

### 3.1.2.1 *Narcosis Protocols*

To perform a stable anesthesia during surgery and measurements, a defined narcosis protocol is needed. For pigeons, the following narcosis protocol has been used for the surgery:

| Time | Event |
|---|---|
| - 12hrs | Pigeon is fasted |
| - 0.5hrs | Buprenorphine (0.5mg/kg of bodyweight) |
| (0 → $T_{narcosis}$) | Narcosis introduction: 5% isoflurane (oxygen flowrate 2l/min)<br>During surgery: 2% isoflurane (oxygen flowrate 0.5l/min)<br>After surgery: 1.5% - 2% isoflurane (oxygen flowrate 0.5l/min) |
| $T_{narcosis}$ | Meloxicam (0.5mg/kg of bodyweight) |
| $T_{narcosis}$ + 4hrs | Meloxicam (0.5mg/kg of bodyweight) |
| $T_{narcosis}$ + 8hrs | Meloxicam (0.5mg/kg of bodyweight) |
| 12hrs | Buprenorphine (0.5mg/kg of bodyweight) |
| 24hrs | Buprenorphine (0.5mg/kg of bodyweight) |
| 36hrs | Buprenorphine (0.5mg/kg of bodyweight) |
| 48hrs | Buprenorphine (0.5mg/kg of bodyweight) |
| 60hrs | Buprenorphine (0.5mg/kg of bodyweight) |
| 72hrs | Buprenorphine (0.5mg/kg of bodyweight) |

Meloxicam and Buprenorphine are used for pre- and postoperative analgesia. The surgery takes about $T_{narcosis} \approx$ 2hrs. The fUS experiments were performed over the course of several weeks after surgery with the same pigeon. For these measurements, a modified narcosis protocol is used with premedication of Midazolam to reduce the stress level through its anxiolytic and sedative effect:

| Time | Event |
|---|---|
| - 12hrs | Pigeon is fasted |
| - 0.5hrs | Midazolam (5mg/kg of bodyweight) |
| (0 → $T_{narcosis}$) | Narcosis introduction: 5% isoflurane (oxygen flowrate 2l/min)<br>fUS measurement: 1.5% - 2% isoflurane (oxygen flowrate 0.5l/min) |

For the zebra finch measurement, the animal was premedicated with Meloxicam (0.01-0.02ml/10g) and the trepanation was performed with a razor blade. The fUS measurements were carried out directly after the surgery and no postoperative treatment was necessary, because the experiments were final.

It was observed and is reported[77,78] that the applied drugs and narcosis regimes can have a dramatic effect on functional studies. A detailed discussion on the effects of various anesthetic/analgesic drugs in combination with functional measurements of pigeons is given in [59] and [60].

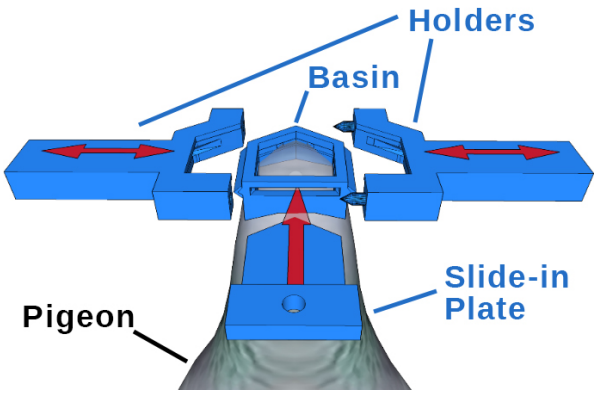


***Figure 19 | Schematic of 3D Printed Basin and Holders***
*The image shows schematically the 3D printed polyamide basin, which is cemented directly on the pigeon skull. The basin can be sealed with the slide-in plate from the back for protection of the trepanation area. For the fUS measurement the slide-in plate is removed and the holders from the left and right are closed around the basin utilizing a key-and-slot joint. The image has been created with SketchUp Make.*

### 3.1.3 Fixation

For the fUS measurements, a robust fixation is essential. Optimizing this was emphasized during this project, which fundamentally contributed to the success of an fUS study. Typically, a non-invasive fixation of avian animals is achieved by stereotactic ear plugs and a bar in the beak, which lead to a reasonable constraint of translational movements. However, one rotational degree of freedom is not accurately restricted and depending on the breathing/movement of the animal, this induces strong clutter signal contributions (see section 2.2.4) and/or causes the imaged brain slice to move out of the fUS imaging plane. A restriction of the rotational motion is difficult because the beak has to remain free to a certain extent, such that the animal's ability to breathe is ensured.

Another approach of fixation is to place a screw in the skull, after flooding it locally with dental cement. However, for fUS studies in small animals this is not feasible, because the screw and its holder are typically largely restricting the imaging area for the ultrasound probe.

Over the course of this project, custom made holders and the basin mentioned in section 3.1.1 were designed to ensure robust fixation at an extensive field of view over the cerebrum. The design utilizes a key-and-slot joint of the basin (see sketch in Fig. 19) and restricts the motion of the animal to 10µm. In Fig. 17b, the installed basin together with the attached holders are shown for an anesthetized pigeon in the fUS setup.

The fundamental advantage of the new design lies in the fact that it allows measurements on awake animals. As discussed in section 2.1.1, this excludes possible strong influences of the anesthesia on the neurovascular coupling, which was observed during this project in pigeons. To perform awake studies with the pigeon, the equipment relevant for anesthesia is removed from the setup. The pigeon is additionally fixated with a wool stocking and tape around the feet to prevent jerky movements that cause decorrelation and impairment of the fUS signals.

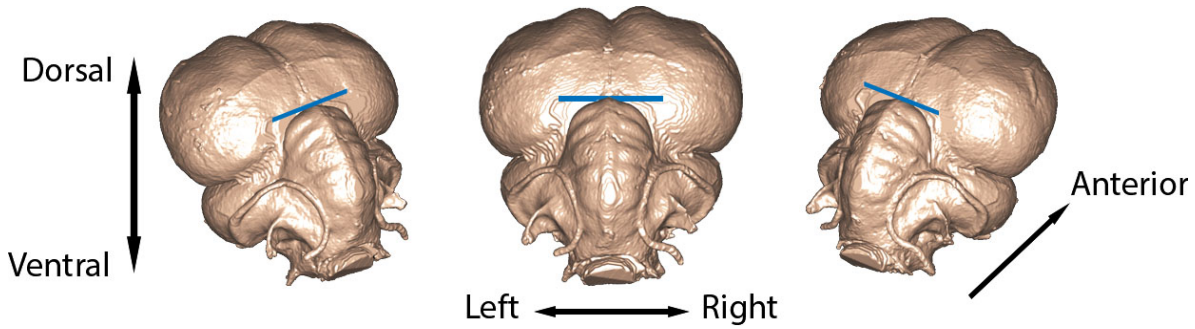


***Figure 20 | MRI Pigeon Brain Surface with Reference Point***

*The figure shows the MRI brain surface of a pigeon from the loft at the University of Konstanz from three different perspectives. The setting of the new reference point at the PG +0mm is marked in blue in the figure.*

### 3.1.4 **Neuronavigation**

To guarantee reproducible measurements over days and in view of comparative pigeon studies, an accurate orientation within the avian brain, i.e. neuronavigation, is important. For the pigeon, the pineal gland in the brain is defined to be the zero location (PG +0mm), which is located exactly between the cerebellum and the cerebrum (see blue bar in Fig. 20). This defines a well recognizable landmark and is less prone to errors than the usually called upon pigeon stereotactic atlas[72]. The transducer angle in the pigeon measurements translates to approximately 65° from the horizontal skull axis in common coordinates.

In order to map a pigeon fUS dataset to the brain architecture, the data is referenced to an MRI brain measurement of another pigeon from the loft at the University of Konstanz (Fig. 20). With the knowledge of the PG +0mm location, an overlay of the datasets is ensured. The location is identified on the day of the surgery and its relative distance to the walls of the installed basin (cf. section 3.1.1) noted. The MR imaging was conducted with a Biospec 94/20 (Bruker BioSpin MRI GmbH, Germany), a 9.4 T small animal MRI system, at the Institute for Clinical Radiology, OCC Münster, Germany.

For the zebra finch fUS study no detailed neuronavigation protocol has been established yet, because the transition from cerebrum to cerebellum is not that easy to identify due to the smaller dimensions of the brain. The vasculature exhibits however a very prominent structure and the main bifurcation was used as the zero location in this project.

The positioning of the transducer is controlled with a 4D stage, composed of one rotation stage (M.060.DG, Physik Instrumente GmbH &Co. KG, Karlsruhe, Germany) connected to a motion controller (Mercury C-863 DC, Physik Instrumente GmbH &Co. KG, Karlsruhe, Germany) and three linear stages (M-UMR8.25, Newport Corporation, CA, USA) of which two (x/y-axis) are connected to another motion controller (MM3000, Newport Corporation, CA, USA). Both controllers are operated with MATLAB and allow accurate positioning at a precision of $< 1°$ and $\sim 10\mu m$, respectively. In order to attach the transducer, a 3D printed socket was designed exactly fitting the ultrasound probe and connected to the rotary stage (Fig. 17c). The assembly

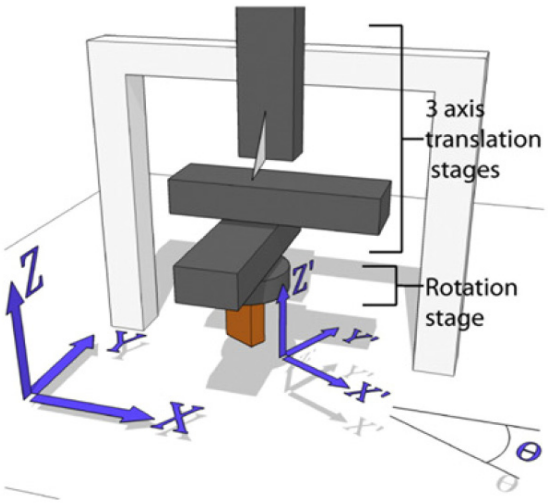


***Figure 21 | 4D Stage Setup***
*The transducer (orange) in the transducer coordinate system ($x$', $y$', $z$') is connected to a rotation stage (round), which is attached to 3 translational stages. The upper stage (translation along the z/z'-axis) is not motorized, because it only has to be set once. The global coordinate system is indicated by ($x, y, z$). Image adapted from [74].*

of the stages is shown in Fig. 21 with the non-motorized translational stage in z-direction at the top. The notation of the figure is maintained through the following.

It is important to note that a precise calibration of the 4D stage is necessary, because typically the center of the rotation axis does not match the center element of the transducer linear array. To accurately calibrate the stage several 3D volumes of two point scatterers (for example tips of vertically oriented needles in water) are acquired under different $\theta$ values. Each 3D volume is acquired by moving the transducer in the azimuthal $y$'-axis with the linear stages. By mapping the 3D volumes to a global coordinate system, the discrepancy between the locations of the point scatterers can be used to introduce a correction term to the displacement of the linear stages. Thus, the new rotation axis becomes equivalent to the center element of the transducer linear array.

In addition to an easier and more accurate adjustment of the transducer positioning, the 4D stage facilitaes the acquisition of a detailed vascularity atlas with the tomography approach as described in section 2.2.7. A full scan with this setup takes about 1 hour at 18 rotational values and 65 slices per 3D volume (see section 2.2.7 for details).

### 3.1.5 Stimulation Setup

Different stimulation patterns were used to analyze functional responses in the brain. For pigeons, the focus has been laid on visual, auditory and magnetic stimulation. For the zebra finch, only auditory stimulation has been applied.

#### 3.1.5.1 *Visual*

Two kinds of visual stimulation setups were used. The first utilizes two white LEDs (LL1502HCWW1-CO1 White LED, 6500K, Ledman, Shenzhen, China) oriented laterally of the pigeon (see Fig. 17d) and was used for the experiments with anesthetized pigeons, because of the high light intensity of the LEDs. This is important because in most cases, the pigeon's eyes were closed under anesthesia, such that a bright light source was in favor.

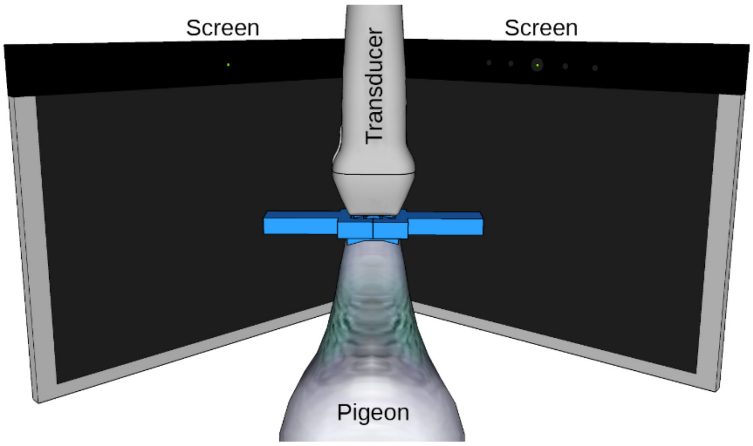


***Figure 22 | Schematic of the Visual Stimulation Setup***

*Schematic figure of a pigeon with the basin on the skull and the fixating holders from the sides (blue, cf. Fig. 19). The transducer is placed above the trepanation area. The visual stimulation is achieved with two screens covering the bird's field of view from lateral left to lateral right. The image has been created with SketchUp Make.*

The second setup consists of two 7'' TFT monitors with a contrast of 500:1 (Kkmoon 7" TFT ColorDisplay LED HD, Shenzhen, China). They are placed in front of the head, one at +45° and one at -45° angle to the pigeon axis, thus covering the pigeon's 90° lateral to 0° frontal field of view (see Fig. 22). Even though the light intensities of the screens are lower, they offer the advantage of possible dynamic stimulation patterns, such as a dot on the screen moving from one rear field to the contralateral rear field of view. This was used in the context of awake measurements of pigeons.

#### 3.1.5.2 *Auditory*

For the auditory stimulation, two loudspeakers (Stereo Speaker E300, Hama, Monheim, Germany) were placed 0.5m frontal of the pigeon head. The zebra finches were stimulated with a single custom made loudspeaker placed roughly at the same distance directly frontal to the bird.

The auditory stimulations consisted of known sound patterns, such as other bird sounds, as well as noise.

#### 3.1.5.3 *Magnetic*

For the magnetic stimulation three Merrit-coil systems were utilized (see Fig. 16a and Fig. 17a). The array was proposed by Merrit et al. [79] and has an enhanced field uniformity at the center compared to a Helmholtz system. It is composed of two inner and two outer coils with a fixed ratio of turn numbers. In this setup, turn numbers of 36 for the inner coils and 85 for the outer coils were used at distances of about $2b \approx 80$cm (the distance between the inner coils $2a$ is roughly a fourth of the distance of the outer coils). The framework, where the coil systems are embedded, is depicted as a schematic with the correct ratios and the axis directions in Fig. 23.

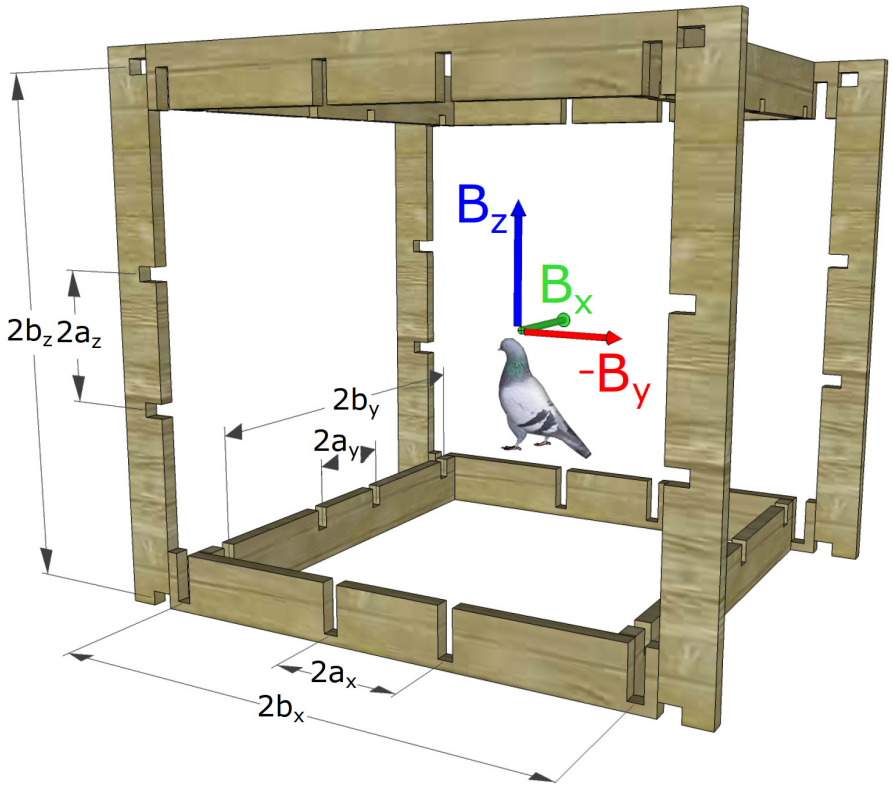


***Figure 23 | Magnetic Stimulation Setup***

*Model of the wooden frame for holding the Merritt coil system. The arrows represent the positive directions of the magnetic field $\vec{B}_{coils}$ of the coils. The pigeon model indicates the relative position of the pigeon's head in the box and to the coordinate system axis (same axis convention as in Fig. 21). Image copied and text modified from [60]*

The positive $y$-direction is defined anterior, $x$ medial and $z$ dorsal with respect to the pigeon location.

A 3-axis flux-gate magnetometer (Bartington Mag-03MS100 with low noise option, Bartington Instruments, Witney, UK) is placed approximately 5cm below the pigeon's head to measure and calibrate the magnetic field vector within the Merrit-coil system. This allows a precise measure of the magnetic field stimulation at the pigeon location. For a detailed information about the magnetic field stimulation setup, the reader is referred to the dissertation of Scheffer [60].

### 3.1.6 Data Recording of the Physiology and Ambient Influences

A dedicated LabView algorithm was implemented to constantly record and save the

- heartrate of the pigeon
- oxygen saturation of the pigeon
- temperature of the pigeon
- head and eye movement of the pigeon
- ambient sound
- magnetic field vector

This data can be used in the postprocessing to evaluate potential artefactual influences in recorded fUS datasets or to analyze the effects of those characteristics on the functional responses. The visual recordings were done with two Basler GigE cameras (Fig. 17f; Basler AG, Ahrensburg, Germany) and the audio recordings with an Avantone CK-1 microphone (Avantone Pro, UT, USA) connected to a Tube MP Studio V3 amplifier (Art Pro Audio, NY, USA). The implementation of the LabView code is explained in detail in [60].

Additionally to the physiology and ambient influence recordings, the LabView algorithm also records the *Diffusing Wave Spectroscopy* (DWS) data (setup shown in Fig. 16e), a method based on multiple light scattering that is capable of detecting neural activity at high sensitivity. The DWS measurements can be performed simultaneously to the fUS experiments and the details of the method with respect to functional recordings on pigeons are discussed in [60] and [59].

For the zebra finch study, no additional data of physiology and ambient influences were acquired.

## 3.2 HIGH DEFINITION FUNCTIONAL ULTRASOUND

Setting up an ultrasound acquisition scheme feasible for functional studies was the main challenge of this project. Even though the first fUS result was published back in 2011[12] and the principles of the method are well discussed, a working fUS implementation is very involved to set up. The main complication is ascribed to the fact that the requirements concerning the ultrasound machine are enormous in terms of data transfer rate and computing performance. To comprehend the magnitude of the demands, a few technicalities of fUS imaging have to be discussed.

fUS is based on plane wave imaging (see section 2.2) with typically $N_c$ = 128 channels of piezo elements that transmit and receive the ultrasound plane wave. In order to resolve the phase information, the received data of each channel is quadrature sampled (sampling frequency $\mathrm{f_s}$ = 62.5Mhz for a transmit insonification of $\mathrm{f}_c$ = 15.6Mhz) and typically consists of $N_s$ = 640 samples to resolve a depth of about $d = (N_s\, c)/f_s \approx$ 16mm, where $c$ = 1540m/s is the speed of sound in soft tissue.

For a single plane wave image, this results in a data size of

$$D_1 = N_c\, N_s \cdot 16bit = 164kB \qquad \textbf{(28)}$$

where $16bit = 2bytes$ is the required data size of the 14-bit A/D-converters per channel. As discussed in section 2.2.2, the SNR and CNR of a single plane wave image is very low and several beamformed angled plane wave insonifications have to be coherently compounded to retrieve a higher image quality. Typically, a coherently compounded plane wave image consists of about $N_a$ = 20 angles, such that the data size for a high quality image is increased to

$$D_{17} = N_a\, N_c\, N_s \cdot 16bit = 3.3MB \qquad \textbf{(29)}$$

which is acquired in 1ms. From this information, the B-mode image is produced.

As discussed in section 2.2.3, the detection of the microvasculature is based on the inter-pulse dynamics of the scatterers. With typical ensemble lengths of $N_e$ = 200 (cf. section 2.2.4), the data traffic for a single PD image to resolve the microvasculature of a brain slice image is

$$D_{PDI} = N_e\, N_a\, N_c\, N_s \cdot 16bit = 655MB \qquad (30)$$

which is acquired in about 200ms. To resolve functional changes in the cerebral blood volume (CBV), the data traffic of $D_{PDI}$ = 655MB needs to be processed at about a Hz frame rate, given the baseline of the PD signal is stable. This demonstrates the huge data traffic, an fUS system needs to cope with.

The first fUS publication[12] by a leading ultrasound research group at the Institut Langevin, ESPCI Paris, France, realized a system, the *Supersonic Imagine Aixplorer,* with a frame rate of 0.33Hz and could image stimulus evoked CBV changes in localized brain areas of rats (cf. section 2.2.6).

To perform fUS at the University of Konstanz, the *Verasonics Vantage 128* ultrasound apparatus (Verasonics, Kirkland, WA, USA), specifically designed for ultrasound research, was delivered to our group in August 2015. However, the system was only equipped with rudimental acquisition schemes, such that it became the main task of this project to implement an fUS algorithm, capable of detecting a localized response in the avian brain evoked by an external stimulation. To perform fUS studies on species such as pigeons, the fUS technology had to be advanced in certain characteristics, because of the unfavorable physiology of pigeons (the details will be discussed in section 4.1). The improved algorithm was termed high definition fUS (HDfUS) and pushes current fUS technology to continuous recording at high frame rates. HDfUS is about a factor of four faster than any other acquisition scheme presented to the community.

### 3.2.1 High Definition Functional Ultrasound: Processing Chain

The three key objectives of HDfUS concerning the optimization of the data handling are:

- **Continuous acquisition:** Acquire continuous datasets such that undesired CVB changes can be filtered and SNR of the functional response is enhanced (see section 4.1).
- **Live processing:** Process and image as much data as possible, such that real time evaluation of the data is facilitated to the best degree.
- **Continuous Saving:** Save the data as raw as possible to enable finding the best set of parameters in signal and image processing in the post-acquisition analysis.

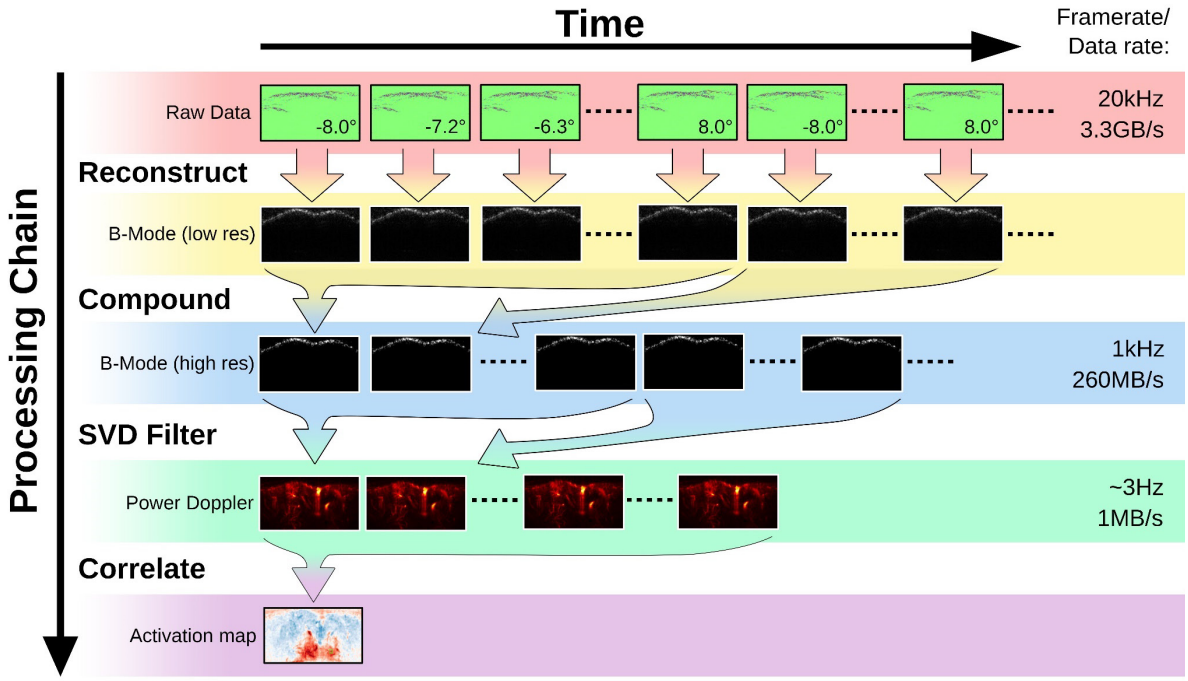


***Figure 24 | The Processing Chain of the Datastream***

*The processing chain from the raw data to the PD images and the activation map. The raw data (red background) of angled plane waves is reconstructed (yellow background) and coherently compounded (blue background). Subsets of the compounded frames are used for the PD images (green background), which allow to retrieve the localized activation in the brain slice (purple background) with an imposed hemodynamic response to the stimulus pattern.*

The general processing chain of HDfUS to satisfy all three criteria is shown in an overview in Fig. 24. The values and parameters shown in the figure correspond to the latest (and fastest) version of HDfUS and shall serve exemplarily to discuss the principle of the processing.

The raw data recording consists of continuous transmission of plane waves at 20kHz under 20 different angles, ranging from -8° to +8°. In order to retrieve the phase of the 15.6MHz ultrasound pulse, the echoes are quadrature sampled at 62.5MHz with 128 A/D converters. The resulting data stream for imaging a depth range of 12mm sums up to 3.3GB/s. The images are reconstructed in the frequency domain (see section 2.2.2.2) and compounded in real time on state-of-the-art GPUs. This results in 260MB/s data (blue background in Fig. 24), which can be written to a Solid State Drive (SSD) via a Serial ATA computer bus interface (version 2 or higher). The SVD computation of a subset of the compounded frames (typically $N_e$ = 300 frames) for the PD imaging can be executed in parallel (green background in Fig. 24). The brain activation map (purple background in Fig. 24) is computed on the basis of all PD images within one HDfUS acquisition by calculating the Pearson correlation (see section 2.2.6).

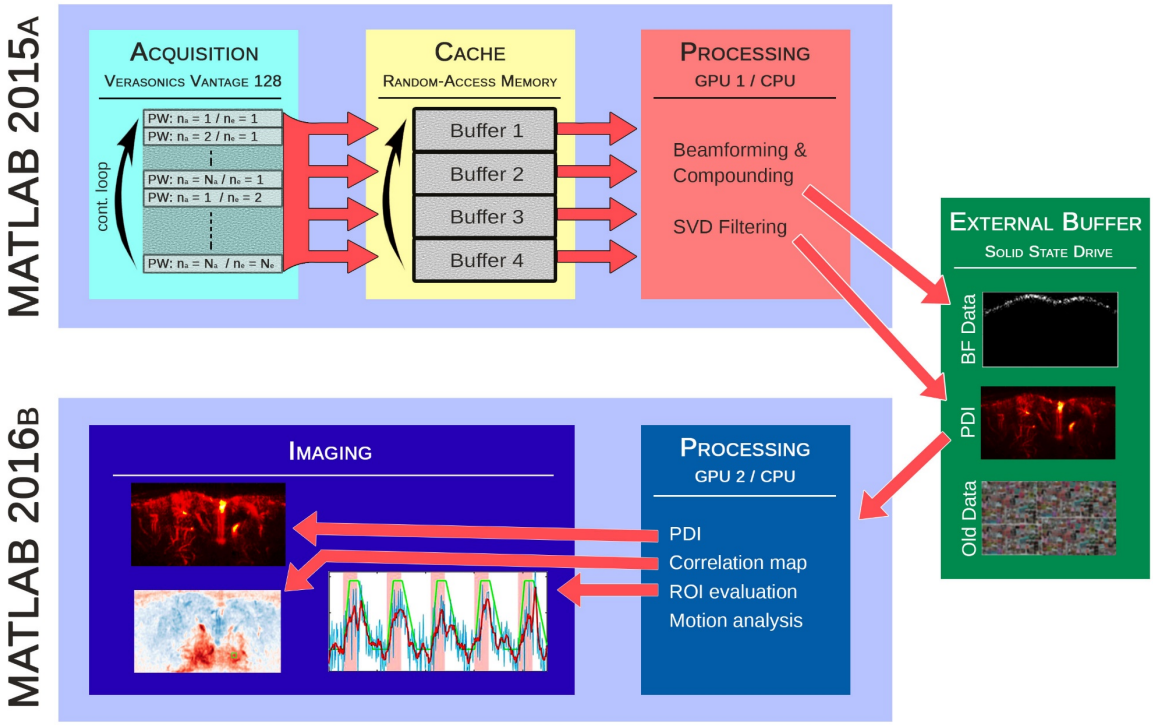


***Figure 25 | Workflow Chart of HDfUS***

*For the HDfUS acquisition, two MATLAB instances are executed to parallelize the processing via an external buffer. See text for details.*

### 3.2.2 High Definition Functional Ultrasound: Implementation

For a successful software implementation of a processing algorithm depicted in Fig. 24, a set of two MATLAB instance working in parallel was chosen to facilitate the utilization of two GPUs and to boost the frame rate. In Fig. 25, the software implementation is schematically shown with the two MATLAB instances that are communicating unidirectional via an SSD as an external buffer.

The first MATLAB instance is working in version 2015a, because the communication of the Verasonics Vantage (v. 3.0.8) is optimized for this (turquoise in Fig. 25). It executes a program to acquire data of $N_a \cdot N_e$ plane wave (PW) transmissions in a continuous loop for the time of one HDfUS measurement (typically 20s to 500s). The data is sent to one of four buffers in the RAM (yellow in Fig. 25) with a chunk size that contains frames to produce one PD image. The four buffers are chosen to prevent interference between existing and new incoming data while processing.

The data from the buffer is then prepared on the CPU and transferred to the first GPU for image reconstruction and SVD filtering (red in Fig. 25). This can be achieved by using MATLAB's own built-in GPU functions, which are however a factor of two slower than C++/CUDA implementations (the parallel computing platform created by the GPU designer Nvidia). Additionally, MATLAB is currently not capable of parallel processing at a reasonable temporal resolution with respect to HDfUS acquisition, which prevents saving the beamformed frames

(BF data) for data evaluation in a post-acquisition analysis. A C++/CUDA algorithm can bypass these issues with MATLAB and was developed in collaboration with the Thorax Center (Erasmus MC, Rotterdam, Netherlands). It is programmed such that the large BF chunk datastream (260MB/s) is written into a preallocated dataset on the Solid State Drive (SSD) external buffer (green in Fig. 25).

The SVD filtered data that produces the PD image is also written to the external buffer and is read out in parallel with the other MATLAB instance (2016b). In that instance, all the PD images are further processed live on the second GPU to prevent an influence on the primary processing unit with the first GPU (blue in Fig. 25). The data is processed to image a live view of the vascularity from the PD images, a correlation map with a response pattern that can be adapted during the measurement and an evaluation of the PD signal over time in an adaptable region of interest (purple in Fig. 25). Additionally, the motion of the animal can be analyzed by running an image registration algorithm over the PD images.

The second MATLAB instance also allows to access the old HDfUS datasets on the SSD from previous measurements to directly compare the vasculature and responses from different animals or acquisitions.

### 3.2.3 High Definition Functional Ultrasound: Relevant Parameters

In HDfUS, a whole set of parameters can be adjusted to optimize the image quality. In this section the individual parameters and their effects with respect to the HDfUS acquisition and software implementation are discussed.

#### 3.2.3.1 *Parameters per Plane Wave Frame*

- **The transmit frequency** was discussed in section 2.2.1 in detail. Higher frequencies result in a better spatial resolution and enhanced blood scattering, but also reduce the field of view due to attenuation. In addition to that, a technical limitation is given through the frequency of the A/D-converters, which is 62.5MHz for the used Verasonics Vantage apparatus. If quadrature sampling of the echoes is implemented, the transmit frequency is limited to a maximum of 15.6MHz, which was used for all HDfUS experiments throughout this project. Additionally, it has to be kept in mind that the transmit frequency has to match the frequency bandwidth of the transducer, which is defined by the characteristics of the built-in piezo elements.

- **The pulse length** of the transmitted ultrasound plane wave is usually set somewhere between one half and a few full cycles, Gaussian modulated. Short pulse lengths results in better spatial resolution and less energy absorption, i.e. heating, of the tissue. Longer pulse lengths bear the advantage of enhanced ultrasonic scattering of blood[5]. The best PD image quality was determined to be around 2.5 cycles for the studies in this project.

- **The transmit voltage** of the channels defines the amplitude of the ultrasonic pulse. For high frame rate ultrasound, higher voltage values (> 15V) can cause tissue heating and

damage to the ultrasound transducer, depending also on the pulse length of the transmit beam.

- **The aperture apodization** defines how many channels are used for transmit and receive. If the ultrasound probe has a field of view larger than the object to be imaged, it makes sense to narrow the area of insonification to suppress reverberations from edge structures, such as skull, skin, hair, feather or air. Especially for very small animals with brain sizes of a few $cm^3$, i.e. zebra finches or mice, an apodization is advised if the aperture of the transducer exceeds the brain size. In this project, the Verasonics L22-14v transducer was used, which has an aperture of 12.8mm, and an apodization was applied for the zebra finch study, but not for the pigeons.

- **The range of samples in depth** defines the imaging depth and should be adapted to just include all important features of the object. This is because the number of acquired samples is inversely proportional to the temporal resolution, due to the limited processing capabilities. Thus, the required imaging depth range should be evaluated in the live view mode before acquiring an HDfUS dataset.

#### 3.2.3.2 *Parameters per Compounded Frame*

- **The number of angled beams $N_a$** defines the amount of plane wave averaging (i.e. coherent compounding) and was already discussed in section 2.2.5.6 to be best set to about 20 in order to take into account the Nyquist limit. A higher value can be set to get a better estimation of the phase of the pixels, but exceeding the Nyquist limit impairs the detection of the larger vessels, which exhibit fast dynamics. In this project, angle numbers between 20 and 36 were used.

- **The angle opening** describes the angle between the maximal and minimal angled transmission. Larger angle openings lead to better detection of laterally organized vessels, because at a larger angle the frequency shift increases (see equation (12)). Vessels that are oriented 90° to a plane wave do not exhibit any Doppler shift in frequency. Larger angle openings, however, also reduce the field of view due to the smaller overlap region in compounding. An angle opening of 16° was found to be a good compromise. It has to be noted that a plane wave transmission of 0° is not advised for the Verasonics Vantage 128 in combination with the Verasonics L22-14v probe, because it delivers artefactual echoes, probably due to crosstalk of simultaneous transmission of all channels.

#### 3.2.3.3 *Parameters per PD Image*

- **The Doppler Pulse Repetition Frequency $f_{PRF}$** is the frame rate of the compounded frames to resolve the inter pulse dynamics (cf. section 2.2.3) of the scatterers. Typically $f_{PRF}$ should be set such that the Nyquist limit is accounted for. For velocity detection of a few cm/s, this represents approximately 1kHz. As the larger vessels with faster dynamics are usually less important in the case of fUS, $f_{PRF}$ may be decreased, enabling

a better phase detection due to more compounding frames. For the fUS measurements in this project, the $f_{PRF}$ was set between 300Hz and 1kHz.

- **The Acquisition Time per PD Image** is defined by the ensemble length and the Doppler PRF $f_{PRF}$. Depending on the fUS algorithm, the acquisition time per PD image can have a strong influence on the sensitivity, which will be evaluated in section 4.1.

- **The ensemble length** $N_e$ defines the sensitivity of blood flow detection and was discussed in detail in section 2.2.5.6. The results discussed in this thesis use ensemble lengths between 140 and 300 for HDfUS acquisitions.

- **The SVD parameters** define the range of modes that suppress the clutter signal (cf. equation (15)). The number of all SVD modes in an PD image is equal to the ensemble length. It was found that the last SVD modes mostly correspond to noise and can also be filtered out. The components relevant for the blood flow were in this project visually categorized to be between 40% and 82% of all SVD modes in the PD image. This, for instance, converts to contributing SVD modes between 120 and 246 for an ensemble length of 300.

#### 3.2.3.4 *Algorithm Performance vs. Acquisition Parameters*

With respect to an optimal performance of the HDfUS algorithm, the crucial parameters are the number of angles $N_a$ and the ensemble length $N_e$. All other parameters either have no influence on the achievable frame rate, are fixed by other boundary conditions or are directly determined by the performance of the algorithm.

In Fig. 26, the maximum possible frame rates of the C++/CUDA algorithm are shown for $N_a$ between 8 and 36 and for $N_e$ between 40 and 320. High values of $N_a$ and $N_e$ result in a better detection of the microvasculature, because of an enhanced SNR and filtering. The two boundaries in Fig. 26 result from the Nyquist theorem for large vessel detection at 1kHz with the corresponding Doppler PRF $f_{PRF} = f_{max}/N_a$ (blue boundary) and the writing limitation of the SSD (red boundary). The arrows in Fig. 26 define the parameter range where the acquisition is within the boundaries. The writing speed of the SSD was evaluated within MATLAB 2015a to ~480MB/s for typical data chunks of 80MB. An actual limitation of 320MB/s is set because the SSD is accessed for live imaging simultaneously in the second MATLAB instance, requiring some bandwidth capacity.

The best set of parameters for live imaging was found to be $N_a$ = 20 (number of angles) and $N_e$ = 300 (ensemble length), where a defined detection of the microvasculature is given as well as an accurate detection of the large vessels within the Nyquist limit (see black cross in Fig. 26). This represents a maximum possible frame rate of $f_{max} \approx$ 20kHz. With this frame rate, the Doppler PRF is $f_{PRF}$ = 1kHz and the resulting writing speed on the SSD is 262MB/s.

If the accuracy of the large vessel detection is of lesser importance, the number of angles $N_a$ can be increased, leading to frame rates of up to 26kHz (see values around $N_e \approx$ 160 in Fig. 26). The enhanced frame rates here are mainly attributed to the fact that the transfer from the GPU to CPU requires less time because the amount of data is reduced by compounding the angles.

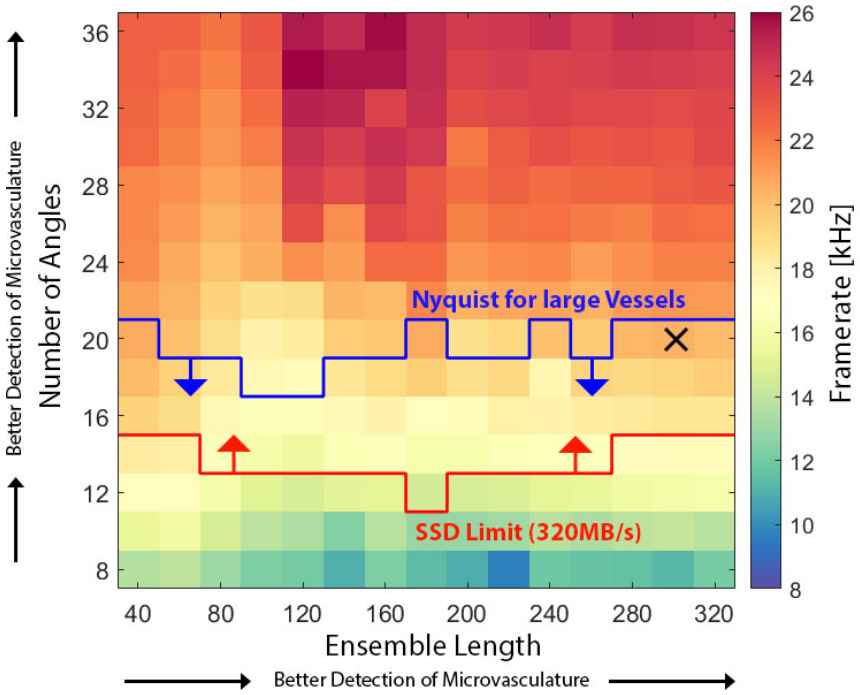


***Figure 26 | Possible Frame Rates with the C++/CUDA Algorithm***

*The maximum achievable frame rates $f_{max}$ of the transmissions with the C++/CUDA algorithm for different number of angles $N_a$ and ensemble lengths $N_e$. The values for the frame rates $f_{max}$ have been decreased by 20% to leave some headroom. The blue and red line indicate the boundaries set by the Nyquist limit and SSD writing speed. See text for details.*

To better understand the influence of the parameter settings on the framerate, the single processing steps need to be looked at. In the workflow chart in Fig. 25, the processing part in the MATLAB 2015a instance was grouped into beamforming with compounding and SVD filtering. The required processing times for each group are shown in Fig. 27 (in the figure the beamforming includes the compounding). For the beamforming step, the processing times depend on the number of angles $N_a$. Two cases are shown representatively: $N_a$ = 10 and $N_a$ = 20. The SVD filtering takes place after the compounding and is thus independent of $N_a$. Figure 27 shows that the overall processing time is dominated by the beamforming step, especially when more angled frames ($N_a$) need to be processed. The time needed for beamforming at a given ensemble length is linearly proportional to the number of angles. The SVD filter timings are linearly proportional to this range of ensemble lengths and take up to 20% of the processing time with $N_a$ = 20.

For some early datasets that will be discussed in the results of this thesis, the fast C++/CUDA was not yet developed. Instead, a preliminary acquisition algorithm using the MATLAB built-in GPU functions was used (a list of the individual datasets and corresponding version is given in appendix 8.5). The possible frame rates with this MATLAB-GPU algorithm are shown in Fig. 28 and are about a factor of two decreased compared to the C++/CUDA version. In consequence, the Nyquist limit to accurately detect large vessels is violated. This can be compensated with

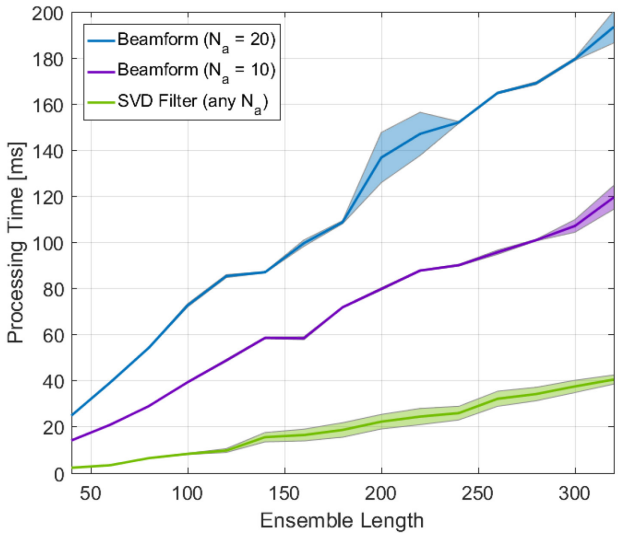


***Figure 27 | Processing Times vs. Ensemble Length***
*The processing time needed for SVD filtering in comparison with the beamforming (with compounding) step for $N_a$ = 10 and 20. The error bar is evaluated by the standard deviation from 10 computational iterations per data point.*

an abandonment of the continuous acquisition, i.e. introducing dead times between the PD image sequence. However, this causes other problems, which will be discussed in section 4.1. The other alternative is to put up with the fact that the detection of the larger vessels is impaired. The consequences of this still have to be thoroughly evaluated, but results discussed in ref. [71] indicate that the majority of a functional ultrasound signal originates from the cerebral capillaries with slow blood flow dynamics.

In Fig. 28, there is also no boundary shown for the SSD writing speed limitation, because the compounded frames cannot be saved permanently with this algorithm. The reason is that MATLAB does not allow parallelization in a convenient way within the same instance. Thus, with this algorithm, only the PD images are produced and saved, which prohibit an adaptation of the ensemble length and/or the SVD parameters in the postprocessing.

The best set of parameters with the MATLAB-GPU algorithm was determined to be $\mathrm{N_a} = 36$ (number of angles) and $\mathrm{N_e} = 140$ and 160 (ensemble length), respectively (see black crosses in Fig. 28). This represents maximum possible frame rates of $f_{max}$ ≈ (10-12)kHz. With this frame rate, the Doppler PRF is $f_{PRF}$ = (300-350)Hz.

In conclusion of the relevant parameters with respect to the technical implementation, the new C++/CUDA algorithm allows a much broader analysis of the data, especially in the postprocessing, because the compounded frames were saved in parallel. With the frame rates achieved by this algorithm, the physical limitation of the ultrasound transmission travel times in the brain can be reached. Furthermore, heating of the probe and/or tissue become a boundary condition, such that it has to be compromised between the transmitted pulse energy and frame rate.

It has to be mentioned that the quantification of the algorithm performance was deliberately focused on the frame rates and not on the image quality in terms of CNR, SNR or fUS sensitivity. These characteristics are more difficult to evaluate, because the analysis would have to be based on a whole range of HDfUS measurements. This requires in depth statistical evaluation

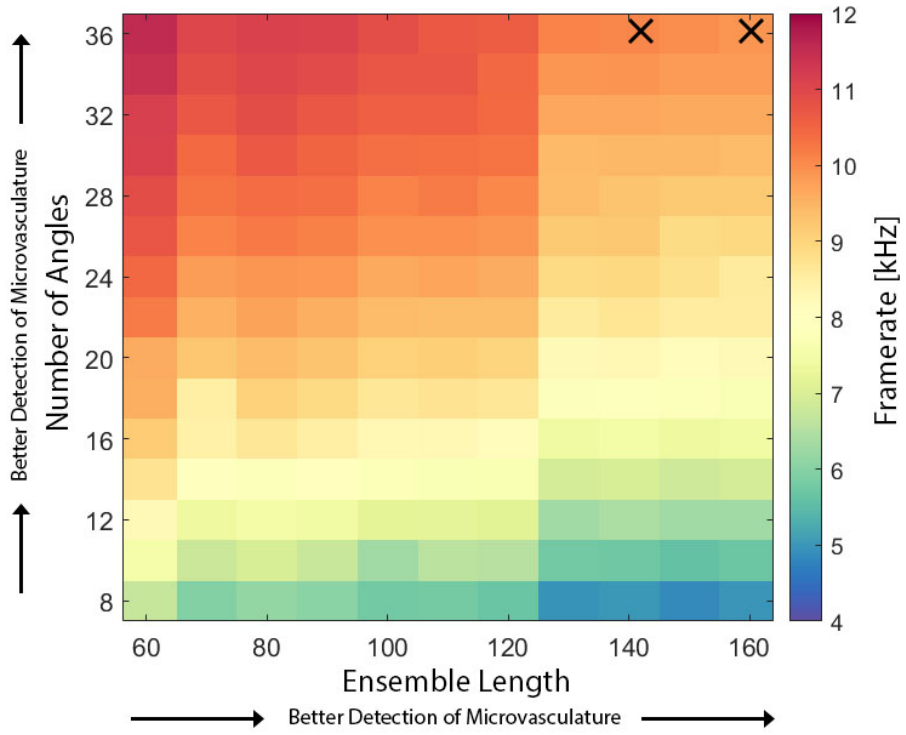


***Figure 28 | Possible Frame Rates with the MATLAB-GPU Algorithm***

*The maximum achievable frame rates $f_{max}$ of the transmissions with the MATLAB-GPU algorithm for different number of angles $N_a$ and ensemble lengths $N_e$. The values for the frame rates $f_{max}$ have been decreased by 20% to leave some headroom. See text for details.*

of several acquisitions and animals, which is very cumbersome and out of the scope of this project.

### 3.2.4 High Definition Functional Ultrasound: Hardware Specifications

The HDfUS acquisition in this project was performed with the following hardware components:

- Transducer: Verasonics L22-14v
  - Center frequency: 18.5MHz
  - Elements: 128
  - Pitch (center-to-center distance between elements): 0.1mm
  - Elevation focus: 6mm
  - Bandwidth/center frequency: 67% (average)

- Ultrasound apparatus: Verasonics Vantage 128 High Frequency Configuration
  - Open software-based research platform, controlled with MATLAB
  - PCI express interface with maximum transfer rates about 6GB/s
  - A/D-converters: 14bit at 62.5MHz
  - 128 channels with 64MB buffer per channel
  - Trigger In and Out option

- **Host controller: DELL Precision Workstation T7910**
  - RAM: 128GB
  - Octa Core CPU: Intel Xeon E5-2680 v3
  - Graphics Cards:
    - Processing: NVIDIA Tesla K80 with two GPUs (12GB RAM each)
    - Video output: NVIDIA Quadro K620
  - HDfUS SSD: Samsung Evo 850 PRO, 2TB (via Serial ATA)

# 4 RESULTS

In this chapter, the results of the project are presented. It starts with a discussion of a simple theoretical model that points out the necessity for HDfUS in the context of pigeon (columba livia domestica) studies. The model's findings are validated with proof of principle experiments on pigeons and rats (wistar). This is followed by HDfUS results of pigeons (visually and auditorily stimulated) and zebra finches (auditorily stimulated) with a focus on the enhancements in spatiotemporal resolution of the method. Subsequently, HDfUS in the context of magnetic field stimulations is debated and some associated artefactual influences are analyzed. The chapter is closed with concluding remarks and a discussion about potential future studies with HDfUS generally.

The acquisition and processing parameters for all the following HDfUS studies in this chapter were adapted to the circumstances (i.e. species, narcosis, etc.). A listed overview for the used parameters for each study is given in the appendix 8.5 to facilitate reproducibility of the results.

## 4.1 PHYSIOLOGY INFLUENCE ON FUNCTIONAL ULTRASOUND

Compared to rats or mice, the physiological characteristics of certain species, such as pigeons, can be unfavorable for conventional fUS imaging. The need of HDfUS in pigeons is pointed out below, based on simulated data and in vivo measurements.

### 4.1.1 Modelling fUS: Rats vs. Pigeons

In order to estimate the influence of the physiology in a functional measurement, a simplified response of the cerebral hemodynamic changes in a vessel (denoted by $\Delta\mathrm{CBV}(\mathrm{t})$) for different cardiac cycle periods is modelled. The cerebral hemodynamics are composed of three factors: Heartbeat-related changes, true hemodynamic response and noise. The heartbeat-related changes $\Delta\mathrm{CBV}_{\mathrm{HB}}(\mathrm{t})$ are visible in the fast time range (> 1Hz; see Fig. 29a and inset in Fig. 30a/b), the hemodynamic response changes $\Delta\mathrm{CBV}_{\mathrm{f}}(\mathrm{t})$ show up in the slow range (< 1Hz; see Fig. 29b) and the noise term $\eta(\mathrm{t})$ has a broadband response (see Fig. 29c). Note that motions due to breathing turned out to have negligible contributions when the head was fixated (cf. section 3.1.3). Thus, it can be assumed

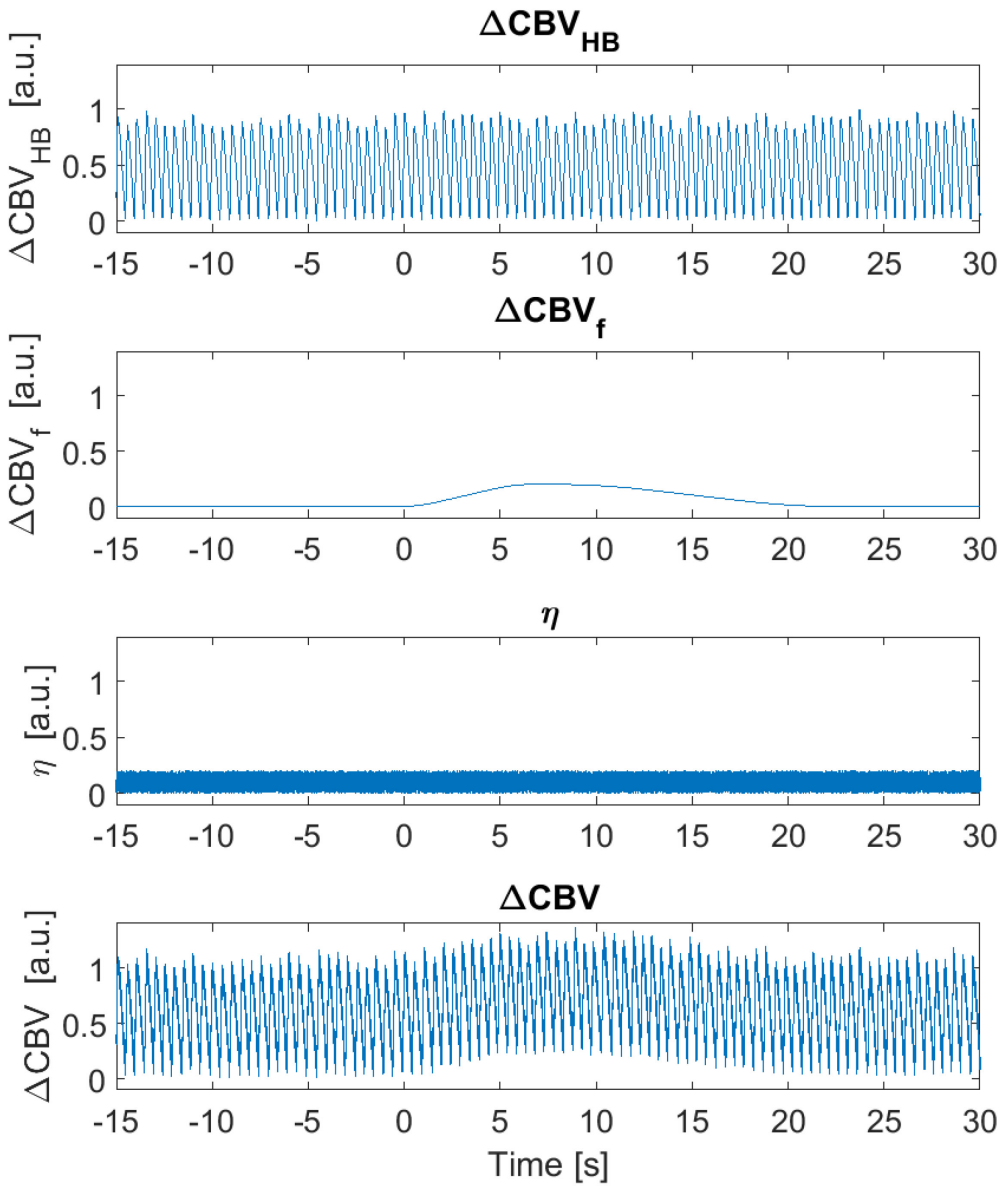


***Figure 29 | Design of $\Delta CBV(t)$***

*Heartbeat changes $\Delta CBV_{HB}(t)$ and hemodynamic response changes $\Delta CBV_f(t)$ show up in the fast (here: 2Hz) and in the slow (< 1Hz) range, respectively. The maximum amplitude of $\Delta CBV_f(t)$ is designed to be 20% of $max(\Delta CBV_{HB}(t))$. The noise $\eta(t)$ is also 20% of $max(\Delta CBV_{HB}(t))$.*

$$\Delta\mathrm{CBV}(\mathrm{t}) = \Delta\mathrm{CBV}_{\mathrm{HB}}(\mathrm{t}) + \Delta\mathrm{CBV}_{\mathrm{f}}(\mathrm{t}) + \eta(\mathrm{t}). \qquad \textit{(31)}$$

In PD imaging, the time required to measure the blood volume should not be much shorter than the hemodynamic time scales. Typical acquisition times for small animals are in the range of $\mathrm{t_{acq}} =$ 200ms to 400ms, over which the $\Delta\mathrm{CBV}(\mathrm{t})$ is averaged[62], such that the PD signal becomes

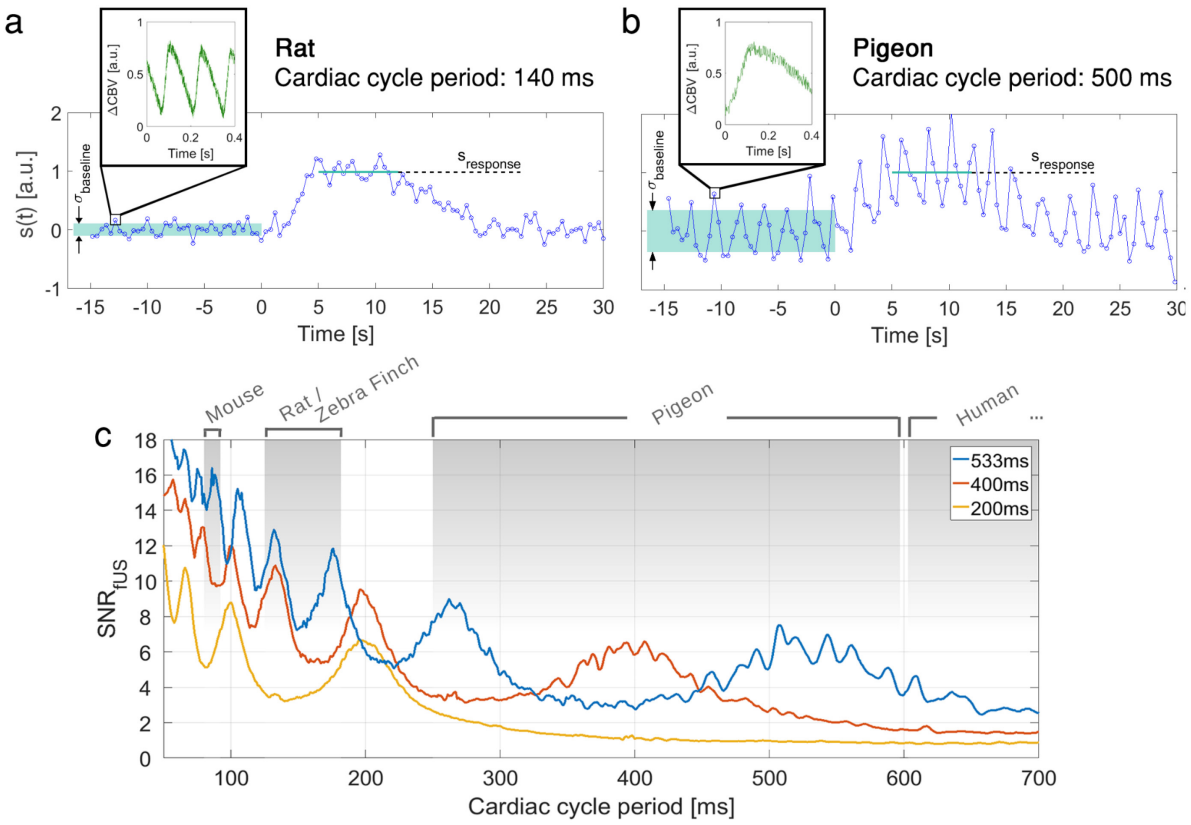


***Figure 30 | Influence of the Cardiac Cycle Length***

*The temporal course of the PD signal $s(t)$ modelled for a rat (**a**) and a pigeon (**b**) with their characteristic cardiac cycle periods. Each data point in $s(t)$ consists of an average of the underlying $\Delta CBV$ signal over the acquisition time of 400ms (shown in green in the insets). The fUS sensitivity is evaluated by $SNR_{fUS} = s_{response}/\sigma_{baseline}$ to be 9.4 for the rat and 2.8 for the pigeon. **c)** The $SNR_{fUS}$ over the whole range of cardiac cycle periods from mice to humans at different acquisition times (200, 400 and 533ms). The resonances occur when an integer of cardiac cycles fits with the acquisition time.*

$$s(t) = \int_{t}^{t+t_{acq}} \Delta CBV(t')dt'. \qquad (32)$$

In Fig. 30a/b, the PD signal $s(t)$ is shown for an acquisition time of 400ms and cardiac cycle periods of 140ms and 500ms, which are typical values for rats and pigeons, respectively. To get an estimate on how the heartbeat frequency affects the sensitivity of a functional measurement, an fUS signal-to-noise ratio $SNR_{fUS} = s_{response}/\sigma_{baseline}$ is defined to be the mean amplitude $s_{response}$ in the time interval of maximum response divided by the standard deviation $\sigma_{baseline}$ of $s(t)$ before the response (see green indicators in Fig. 30a/b). For these different cardiac cycle periods, this simplified model predicts an impairment in the $SNR_{fUS}$ by a factor of 3+ for the pigeon. The lower $SNR_{fUS}$ has to do with the fact that the PD averaging time is too short to include one full heartbeat.

To get a more general understanding on how the heartbeat affects the sensitivity of fUS, the $SNR_{fUS}$ is evaluated for any cardiac cycle period ranging from 50ms (1200bpm) to 700ms

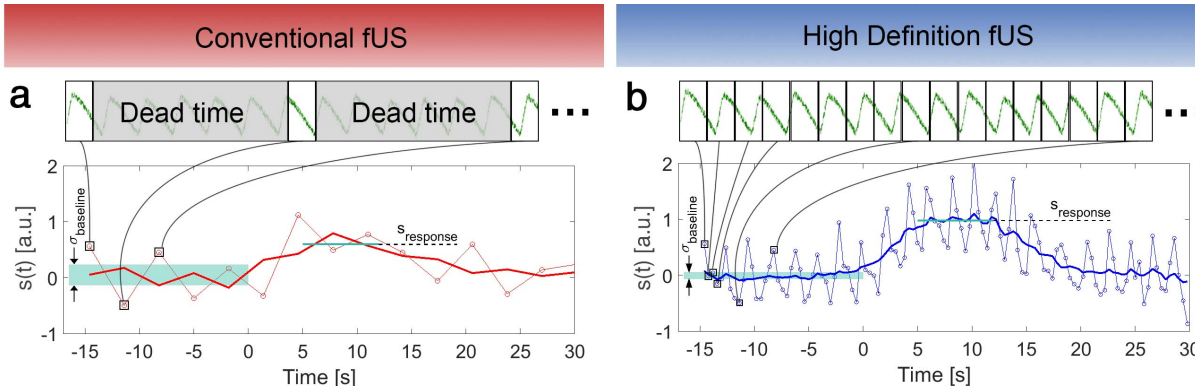


***Figure 31 | Conventional vs. HDfUS***

*A sketch of the data acquisition in conventional fUS with dead times (**a**) and High Definition fUS (**b**). Every data point $s(t)$ is based on the average signal of $\Delta CBV$ (plotted in green on top) over the acquisition time of 400ms. The higher frame rate of HDfUS allows enhanced low pass filtering (0.25Hz) of the data (thick lines in the figure), such that the $SNR_{fUS} = s_{response}/\sigma_{baseline}$ compares with 16.3 for HDfUS to 3.1 for the conventional fUS.*

(85bpm), which covers the physiology from mice to humans[80,81] (see Fig. 30c). Maximum resonances occur when the acquisition time of a PD Image is a multiple of a full cardiac cycle period. A second observation is that there is a general increase in SNR when more cardiac cycles are included, which is due to an implemented frequency fluctuation of 5% in $\Delta\mathrm{CBV_{HB}(t)}$ (see Fig. 29).

A possible solution to obtain high $\mathrm{SNR_{fUS}}$ measurements is to adjust the PD acquisition time to include at least a few full heartbeats. This seems a valid approach for rats, but for pigeons, with their slow heartrates, this means losing the key advantage of high temporal resolution as compared to other slower functional neuroimaging methods like fMRI.

An alternative approach consists of low pass filtering the signal $\mathrm{s(t)}$ such that the beat frequency resulting from the interaction between averaging period and heartbeat period is suppressed. This is however not an easy task because of the vast amount of data produced in microvasculature PD imaging (~3GB/s). The reason for these high transfer rates is that a single low noise PD image consists of $\mathrm{N_F} = N_e N_a$ observations of every pixel, which is necessary to retrieve the blood signal in backscattered ultrasound (see section 3.2). Due to the fact that echoes from tissue are orders of magnitudes higher compared to blood[5], $\mathrm{N_F}$ typically has to include several thousand samples. The processing capabilities, including beamforming and filtering, of current fUS systems is in the order of 2-5kHz[12,22], whereas best results in terms of signal and contrast to noise ratio for PD images occur when the actual sampling is done at >10kHz[11,61]. Thus, typical fUS measurements with high quality PD images require dead times for processing between the frame acquisitions[12,25].

Figure 31a shows the implications on the $\mathrm{SNR_{fUS}}$ of these dead times in the PD signal $\mathrm{s(t)}$ in pigeons as demonstrated with the model from Fig. 30. Here it is assumed that only every eighth frame can be processed due to the limited processing capabilities of current systems. A low pass filter of 0.25Hz (thick red line) slightly enhances the $\mathrm{SNR_{fUS}}$ from 1.7 to 3.2. The effect is

relatively small due to the few data points available. In Fig. 31b the filter is applied to a dataset of continuous PD acquisition, which enhances the capabilities of the filter drastically and increases the $\mathrm{SNR_{fUS}}$ by a factor of about 6 from 2.8 to 16.3. Such continuous PD acquisition are offered by HDfUS.

### 4.1.2 fUS Experiments: Rats vs. Pigeons

To validate the assumption obtained from the model, fUS experiments were performed on a rat and a pigeon as a proof of principle. For best comparison, stimulations known for strong functional responses for either animal were used. For the rat, an activation was evoked in the barrel cortex by electrically stimulating the left forelimb (with two conductive cannulas as needle electrodes at 10Hz repetition frequency, 18V and 200µs pulse width). This was shown recently[18] to result in high responses and could be reproduced in this study (see appendix 8.1 for details). For the pigeon, a response was induced in the visual wulst by unilaterally stimulating the rear field of the left eye with a static white light LED flashing at 5Hz (see section 3.1.5.1). Vision is thought to be the predominant sensory system in most birds and widely studied in pigeons[49,52,82,83]. In addition, the timing for the single PD images is increased from 400ms to 533ms in the pigeon case, to include at least one full cardiac cycle.

In the comparison study, the transducer was oriented above the barrel cortex for the rat and above the visual wulst for the pigeon (Fig. 32a-b/a'-b'). For a first estimate of the fUS sensitivity, the Pearson correlation maps of the individual hemodynamic response of the animal are evaluated in Fig. 32c/c' (the red and blue boxes demonstrate the different results of conventional fUS and HDfUS). The activated region can be visualized in the rat using conventional fUS and HDfUS with $\mathrm{r}$-values in the signal region of interest (purple ROI) of $3.5\sigma$ and $7.6\sigma$, respectively. Here, $\sigma$ represents the spatial standard deviation in the noise region (see black box in Fig. 32c/c'). For the pigeon, the $\mathrm{r}$-values in the signal region decrease to $1.2\sigma$ (conventional fUS) and $5.1\sigma$ (HDfUS), which indicates the necessity for higher frame rates in this species.

To further analyze the stimulus evoked response, the PD signals $\mathrm{s(t)}$ of the purple ROI in the activated area are shown in Fig. 32d/d', with the average response $\bar{\mathrm{s}}(\mathrm{t}) \pm \sigma_{\mathrm{s}}$ over the first eight stimulations in Fig. 32e/e'. Whereas HDfUS provides only a slight improvement for the rat, it appears crucial for pigeons. To get a quantitative estimate of the improvement due to HDfUS, a signal-to-noise $\mathrm{SNR_{fUS}} = \bar{\mathrm{s}}_{\mathrm{max}}/\sigma_{\mathrm{s}}$ is defined to be the ratio between the maximum in the average response $\bar{\mathrm{s}}_{\mathrm{max}}$ and the mean value of the standard deviation $\sigma_{\mathrm{s}}$ over the eight stimulations. For the rat, the $\mathrm{SNR_{fUS}}$ improves only from 8.9 to 9.3 with the HDfUS scheme. For the pigeon, however, the enhancement from 1.6 to 6.0 due to HDfUS makes all the difference between success and failure.

In the previous section 4.1.1, it was hypothesized that the impaired $\mathrm{SNR_{fUS}}$ in pigeons originates from the augmented baseline fluctuations and slower heartrate. This argument is supported with the raw non-lowpass filtered HDfUS signals in Fig. 32d/d', where a higher variance of the signal can be observed. To evaluate this in more detail, the signal fluctuations in the whole vascular system over time can be calculated with the low frequency components

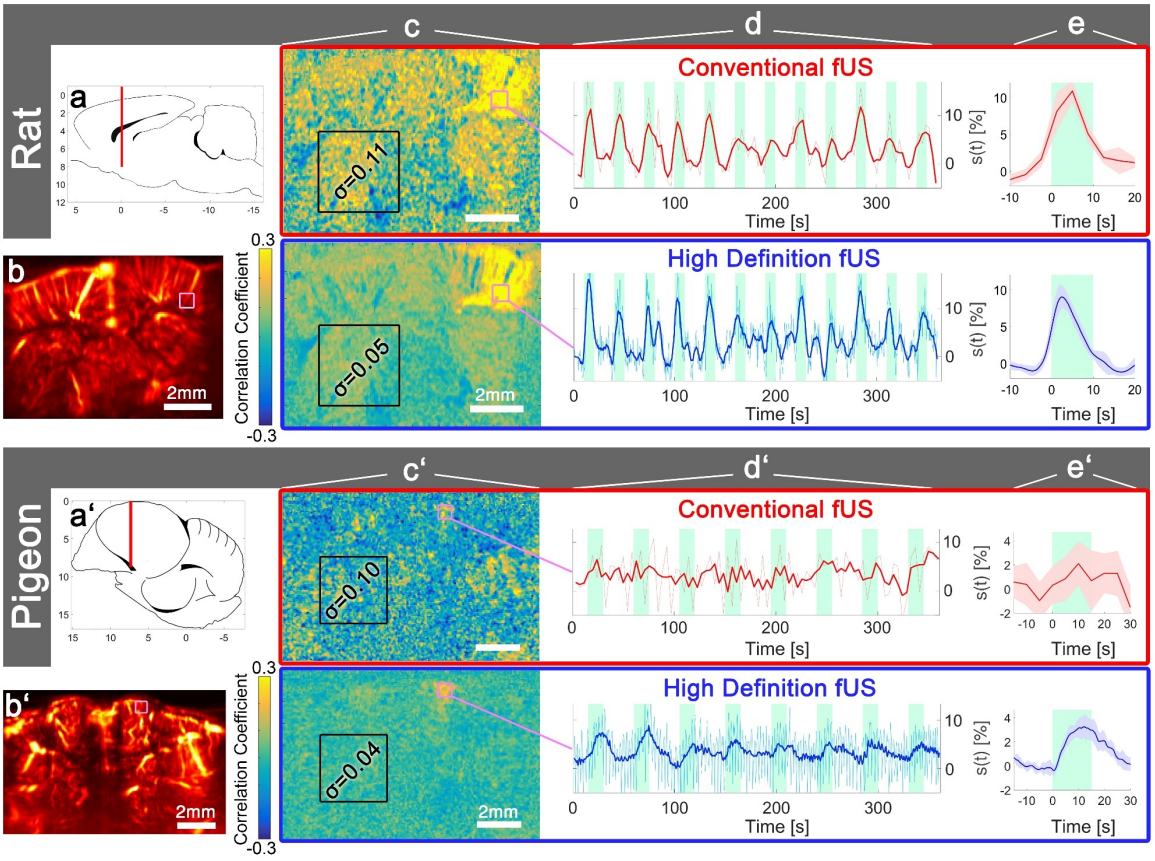


***Figure 32 | Conventional vs. HDfUS for a Rat and a Pigeon***

***a/a')*** *shows the orientation of the transducer with the corresponding PD image in* ***b)*** *for the rat at bregma +0mm and* ***b')*** *for the pigeon at PG +8mm.* ***c/c')*** *Pearson correlation maps for the conventional fUS and HDfUS mode. The color scaling ranges between ±0.3. The standard deviation of the $r$-value in the noise region of interest (black ROI with (3mm)²) is shown within the maps. The size of the purple ROI in the signal region is (0.6mm)² with its mean signal plotted in* ***d/d'****. It shows the raw and low pass filtered data for both modes.* ***e/e')*** *The average over eight low pass filtered responses. The underlying data is the same for the conventional and HDfUS, but the conventional fUS data only includes every eighth PD image. The cardiac cycle was measured with a pulsoxymeter to be (152.9±2.6)ms for the rat and (463±15)ms for the pigeon during this acquisition.*

filtered out (see Fig. 33). The fluctuations are 2.6 times higher for the pigeon case, such that a filter suppressing the cardiac dynamics is more crucial in this species.

In addition to the higher fluctuations, the amplitude of the response is a factor of three smaller in the pigeon (3.1 ± 0.5%) compared to the rat (9.0 ± 1.0%), further impairing the $\mathrm{SNR}_{\mathrm{fUS}}$. A discrimination of such small signals from the noise level makes an efficient suppression of the baseline fluctuations even more essential.

Considering these observations, it can be postulated that successful fUS in pigeons requires continuous PD acquisition with several $\mathrm{s}(\mathrm{t})$ observation images per second, meaning HDfUS as it was introduced in section 3.2.

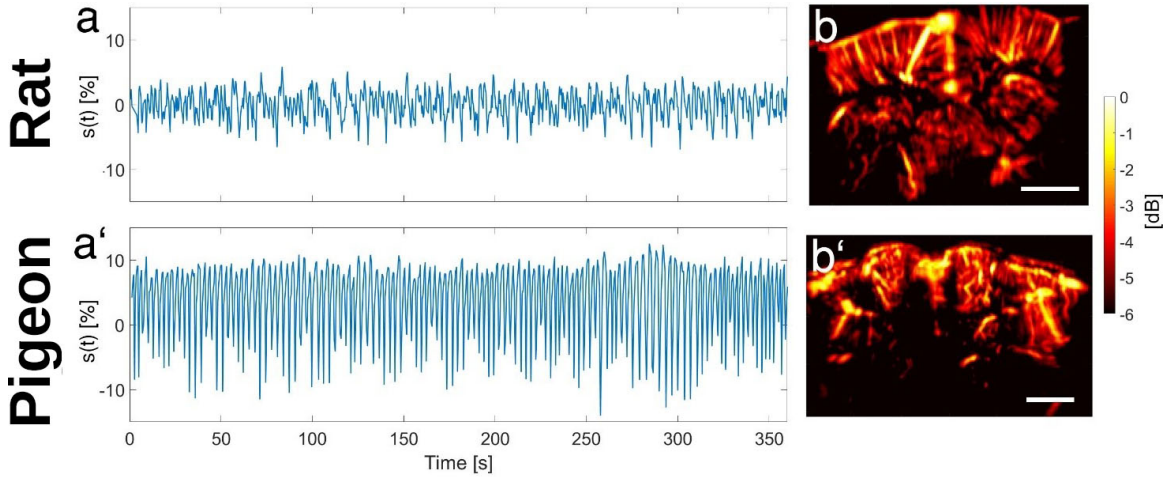


***Figure 33 | Baseline Variations in the PD Signal for a Rat and a Pigeon***
*High pass filtered (0.2Hz) average signal variations over the whole PD image (-6dB masked) for the rat (**a**) and pigeon (**a'**). PD images in **b** and **b'**. The temporal standard deviation is 2.2% in the rat and 5.6% in the pigeon. The scalebar is 2mm in both images.*

## 4.2 Functional Ultrasound - Visual Stimulation

The neural activity of pigeons evoked by a visual stimulation is a large research field in the neuroimaging community. One of many reasons is the asymmetric pathway architecture in the pigeon brain[49]. To demonstrate the capabilities of HDfUS in the context of the avian visual system, data was acquired with one anesthetized and two awake pigeons under different stimulation patterns (cf. section 3.1.5.1).

### 4.2.1 Static Light Source

First, the case of an anesthetized male pigeon is studied with a stimulation of a non-moving unilaterally flashing (5Hz) light source located in the rear field of view. On the front page of this manuscript, a coronal plane for left eye stimulation is shown with the vascularity in red and the measured activation of the visual wulst in blue. This image was rendered on the basis of HDfUS acquisition at 21 different brain slices and five stimulations per slice. A selection of the different slices are shown in Fig. 34a, which were acquired consecutively by mechanically moving the transducer to the positions according to Fig. 34d. The response has an average signal increase of up to 1.4% (Fig. 34b) and is mainly concentrated in the contralateral visual wulst (Fig. 34e), when the pigeon is stimulated at the left eye (Fig. 34c). The inverted case of right eye stimulation results in a likewise inverted response, but with a slightly higher amplitude of 1.8% (see Fig. 35).

As can be seen from Fig. 34b/e and Fig. 35b/e, there is no activity observed in the entopallia of this pigeon. The reason for this is that the light source was located in the very rear field of view and such a stimulation mainly projects to the visual wulst.

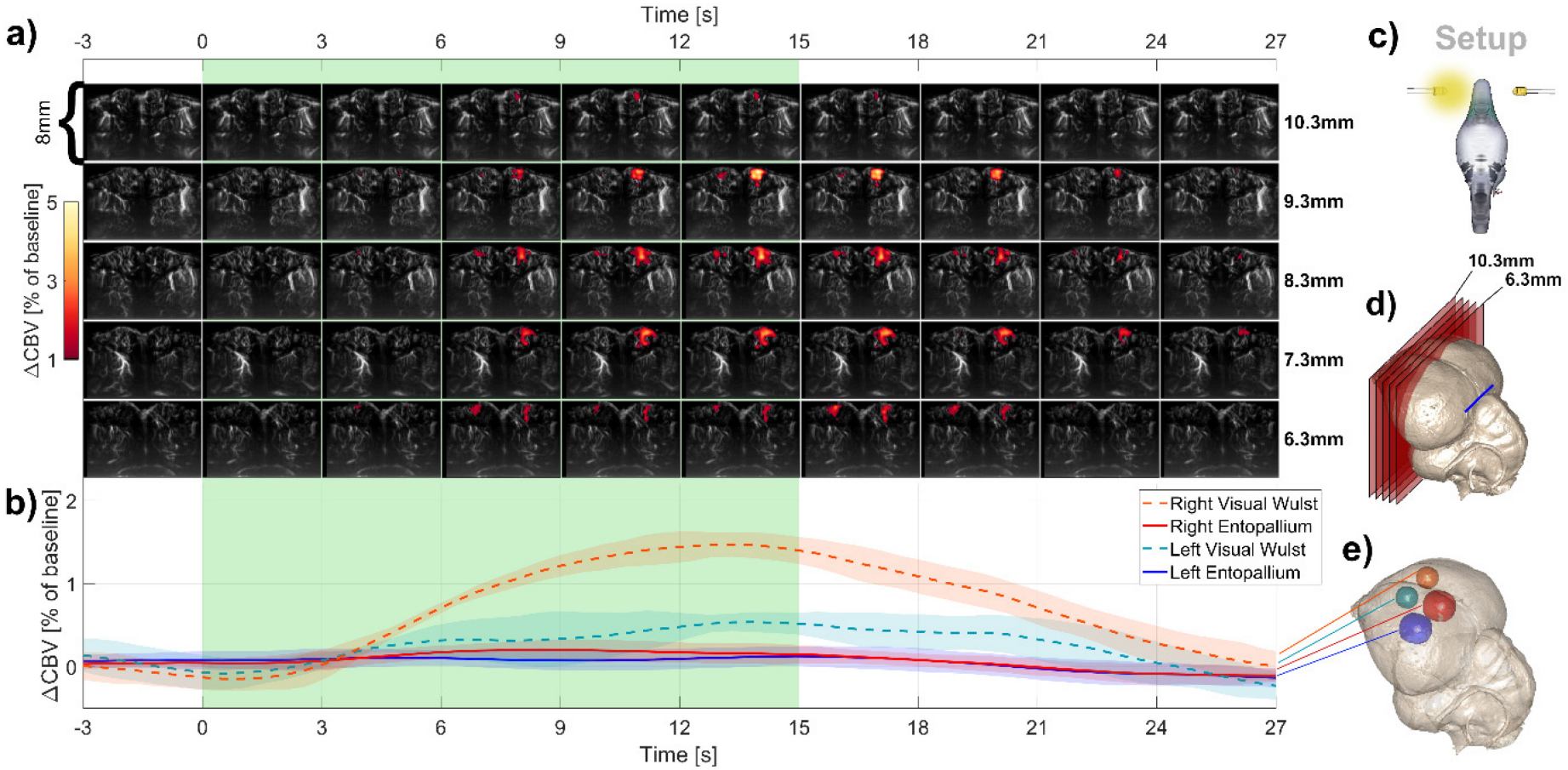


***Figure 34 | Unilateral Left Eye Visual Stimulation of an Anesthetized Pigeon***

***a)*** *The temporal course of ΔCBV by PD imaging (previously denoted as $s(t)$) within the visual wulst in five brain slices. Each image shows the vasculature as a greyscale map derived from the PD image and the ΔCBV between 1% and 5% as a colored overlay. The positions of the slices within the brain are shown to the right of the images and in* ***d*** *with respect to the PG location (blue bar).* ***b)*** *The average signal (error band one standard deviation) within four different regions of interest relevant for the visual system, whose positions are indicated in* ***e*** *with the corresponding colors. The green bar specifies the timespan of stimulation.* ***c)*** *A schematic of the setup.*

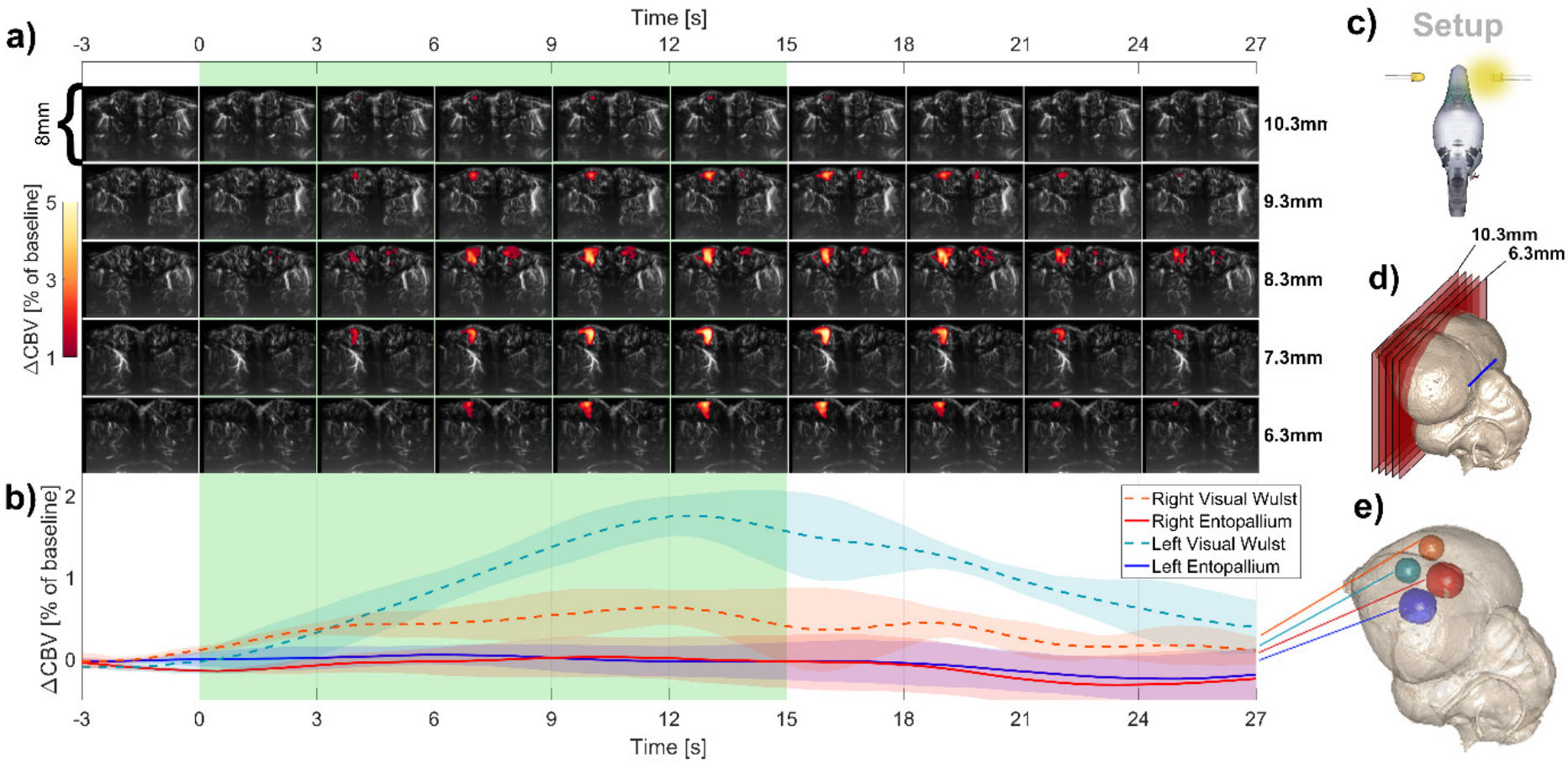


***Figure 35 | Unilateral Right Eye Visual Stimulation of an Anesthetized Pigeon***

*The figure has the same structure and layout as in Fig. 34, but with contralateral stimulation. See text for details.*

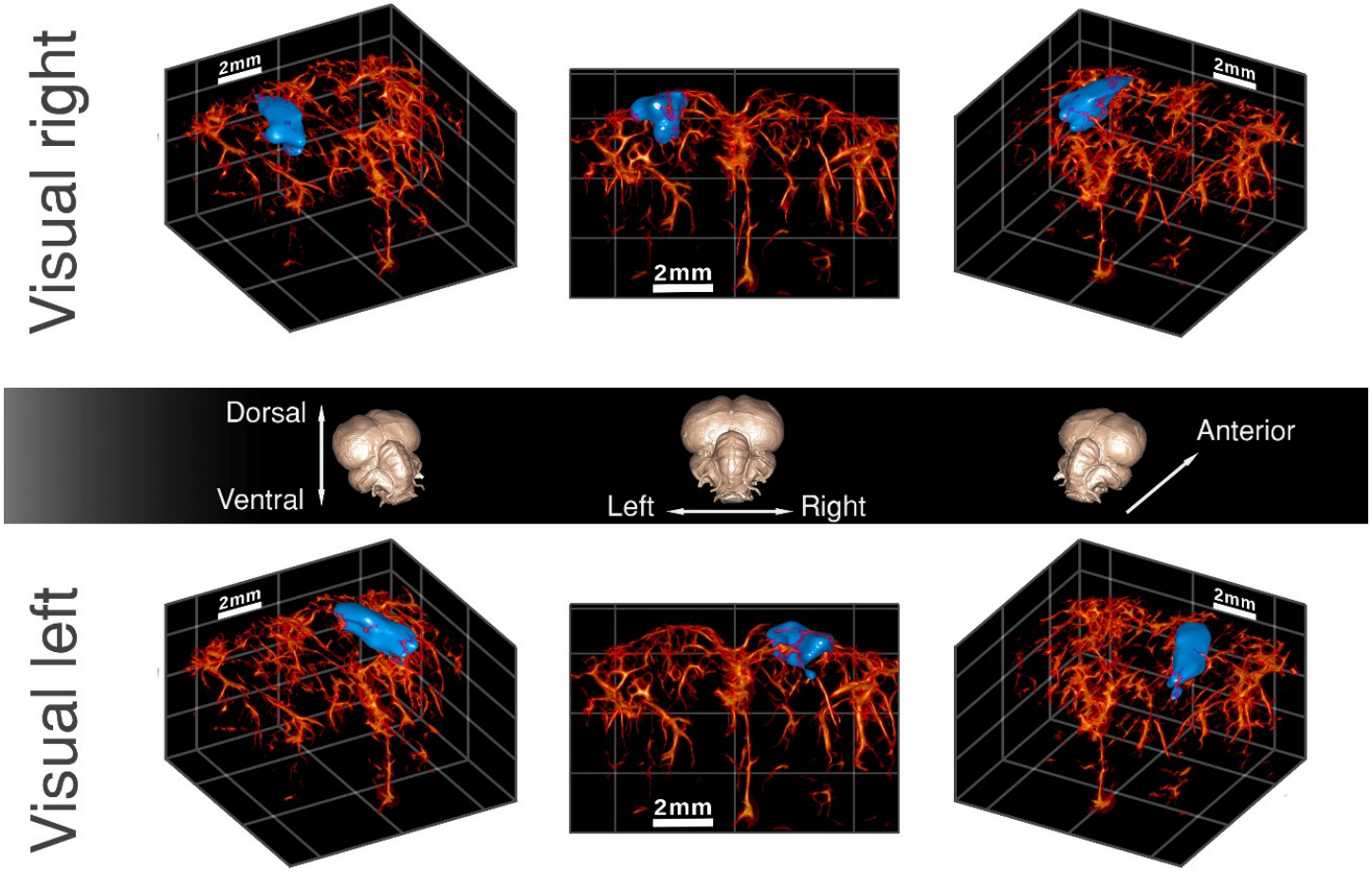


***Figure 36 | 3D Representation of the Unilateral Visual Stimulation of Pigeons***

*The activation in blue and the vascularity in red for left and right visual stimulation and from three different viewpoints. The brain surfaces in the middle show the angle of view (cf. section 3.1.4). The middle bottom figure shows the same response as on the front page.*

To comprehend the full integration of activation in the pigeon brain, a 3D reconstruction of the response in the 21 slices was evaluated. Figure 36 shows the activation (blue) as an overlay on the vasculature (red) derived from PD imaging for both stimulation patterns. An area is defined as active when the correlation coefficient of ΔCBV is $r > 0.2$ (cf. section 2.2.6). The three different perspectives are shown to comprehend the spatial integration of activation in the visual wulst from PG +3.5mm to +13.5mm. The 3D vascularity was extracted by 3D skeletonizing the stack of PD images and not with the tomography approach from section 2.2.7.

With the enhanced temporal resolution offered by HDfUS, the complex dynamics within the activated region can be studied in detail. Figure 37 shows that the area of the highest response is shifted to the posterior of the contralateral visual wulst under right eye stimulation and to the anterior under the left eye stimulation. The time required to reach the signal peak $\Delta CBV_{max}$ shows that low peak amplitudes (blue in Fig. 37a/a') tend to correspond to late responses (purple in Fig. 37b/b'), whereas high $\Delta CBV_{max}$ are mainly found around 14s. This is verified with Fig. 38, where the delay times of reaching $\Delta CBV_{max}$ after stimulation are shown in a histogram. Exploiting the high spatiotemporal resolution offered by HDfUS, it is possible to resolve in detail the temporal spreading of the complex hemodynamics within the activated visual wulst. To the best of my knowledge, this was not revealed previously by any other method at this level of detail and field of view.

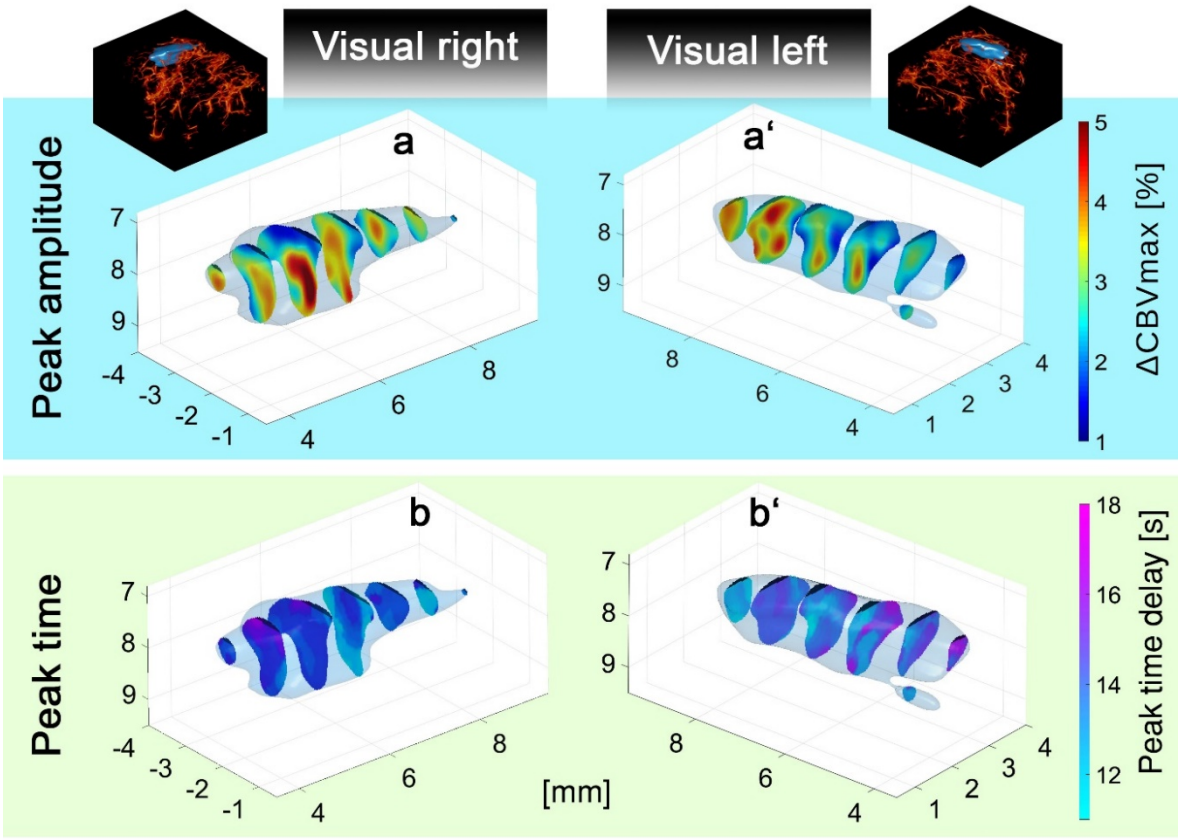


***Figure 37 | Complex Dynamics in the Activated Visual Wulst***

*The figure shows the spreading of the CBV response in the activated region with the peak amplitude values $\Delta CBV_{max}$ in **a/a'** and the delay times when the peak amplitude $\Delta CBV_{max}$ is reached in **b/b'**. The activity maps are depicted at the top of the figure for orientation and are the same as in Fig. 36.*

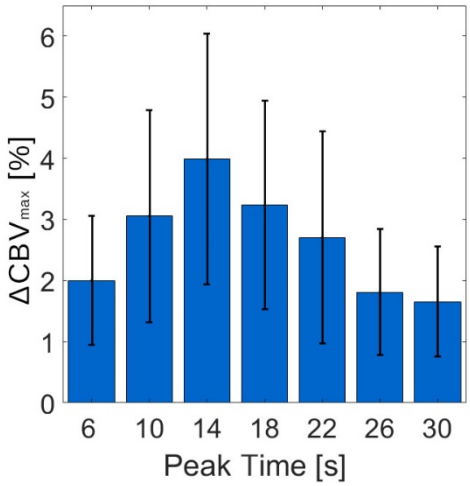


***Figure 38 | Average Maximum Signal Amplitude vs. Peak Times***

*Average maximum signal amplitude $\Delta CBV_{max}$ for voxels at the corresponding peak time. For voxels that peak at ~14s, the corresponding average $\Delta CBV_{max}$ is largest. For responses that peak later, the matching peak amplitude values are lower. The high standard deviation is due to the variance in the relative response strength.*

### 4.2.2 Moving Light Source

In order to investigate the visual system of pigeons in more detail and demonstrate the full potential of the HDfUS method, measurements on two awake pigeons (one male, one female), stimulated with a moving and constantly illuminating light source, were performed. It was observed that the pigeons were in most cases focusing on the moving light source during stimulation and the temporal spreading of the activation exhibit very similar characteristics for both animals, such that only the male pigeon will be discussed in this section.

In Fig. 39a-e, the neurovascular response within the visual system is shown for a 5mm x 5mm white square horizontally moving from the right to the left in 15s on a black background (Fig. 39c). Figure 39 has almost the same layout as Fig. 34 and the temporal course of ΔCBV is shown within the visual wulsts and entopallia (average over two stimulations) in seven brain slices (Fig. 39a). An extra subfigure at the bottom (Fig. 39f) depicts the temporal course of the response for the inverted stimulation case (square on screen moving from left to right) with the same parameters otherwise.

In Fig. 39 it is shown, that the resulting response of the pigeons have a strong dominance of the left entopallium, which processes the information input from both eyes. The right hemisphere is almost solely responding to the contralateral stimulation, which happens at about 7.5s when the dot on the screen starts to appear in the left eye's field of view. The left hemispheric dominance is also observed with the inverted stimulus pattern, as shown in Fig. 39f. This asymmetry of the pigeon's visual system has been described before[31,49] and is also referred to as lateralization (cf. section 2.1.2.1).

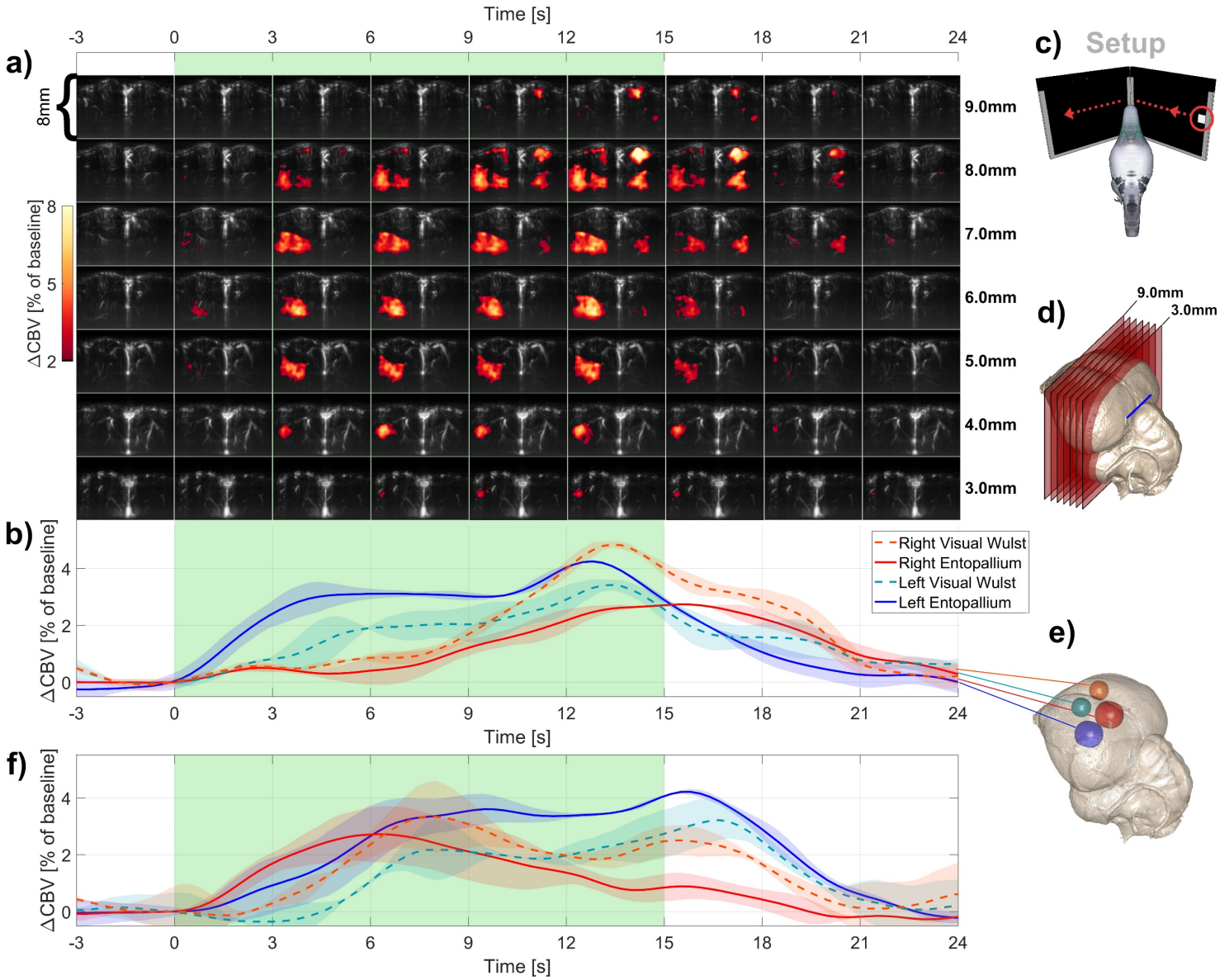


***Figure 39 | Dynamic Stimulation of the Visual System of an Awake Pigeon***

*The figure has the same structure and layout as in Fig. 34, but with an additional subfigure **f** showing the inverted response with the dot moving from left to right.*

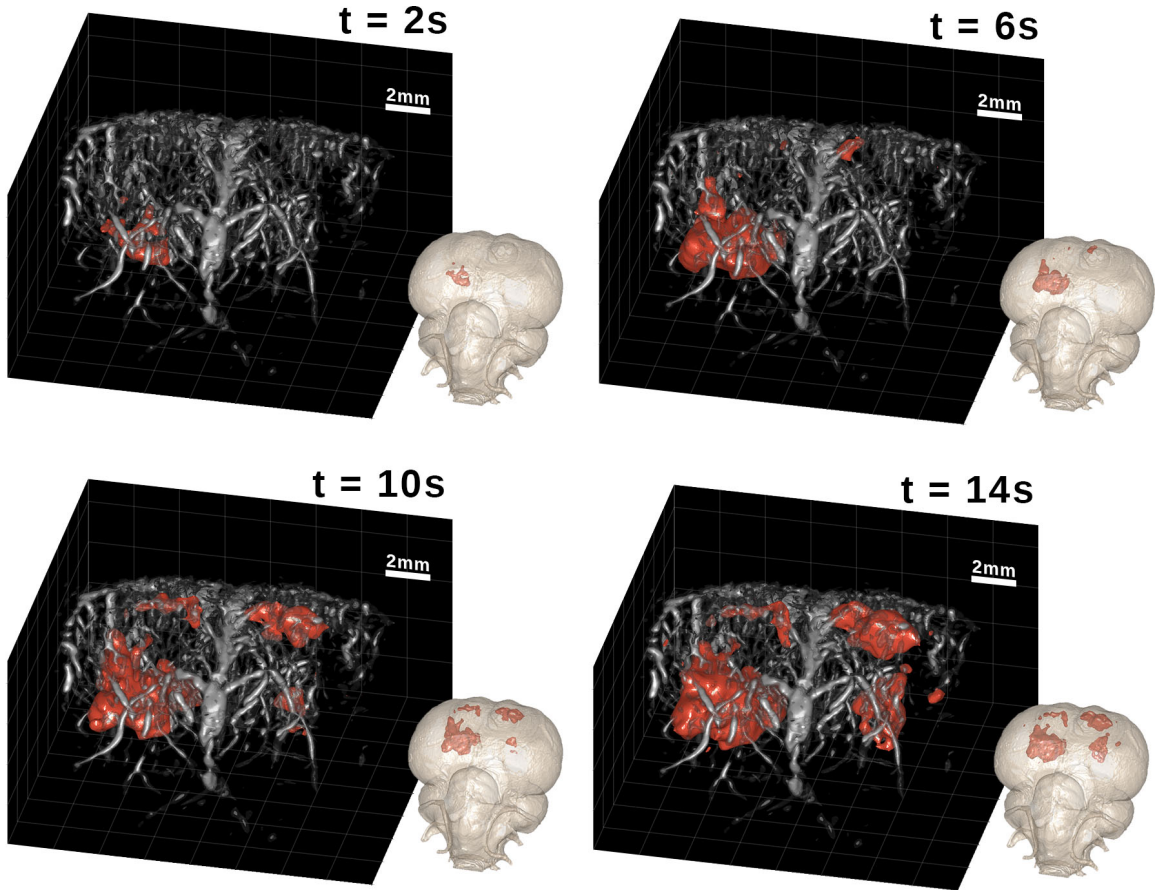


***Figure 40 | 3D Representation of the Response to the Moving Light Source***
*3D reconstructions of 21 scanned slices at different times within the stimulation timespan from the same data as shown in Fig. 39. See text for details.*

To better understand the course of the 3D neural activity, Fig. 40 shows a 3D integration of the response from Fig. 39a-e at four different times from 2s to 14s after stimulation start. The vasculature (grey in Fig. 40) was rendered from PD imaging with the tomography approach (cf. section 2.2.7) and the response (red) shows ΔCBV values above 3% as a colored overlay. Next to the vasculature maps in Fig. 40, the same ΔCBV overlay is mapped to an MRI dataset of a pigeon brain for enhanced comprehension of the neural activity location. The response clearly shows a spreading from the left entopallium, starting at t = 2s, which is contralateral to the stimulation of the square position on the screens. At t = 6s, both visual wulsts show some response, which is followed by an activity in the right entopallium. At t = 14s all main areas of visual system reveal a large volume of increased cerebral blood dynamics with a clear dominance of the left entopallium due to the lateralization.

### 4.2.3 Visual Stimulation - Discussion and Outlook

With the HDfUS study of the avian visual system, the temporal spreading of the neurovascular response within a single brain region of individual animals can be evaluated at excellent detail. This was shown in the visual wulst of an anesthetized pigeon, demonstrating the outstanding definition of the HDfUS acquisition scheme.

To determine how HDfUS can be utilized in the context of the ongoing neurobiology research issue concerning the brain asymmetry, the study of two awake pigeons, stimulated by a dynamic light source was designed. In this case, the resolution offered by HDfUS allowed to investigate the activation in two major neural substrates of the avian visual system, the entopallium and the visual wulst. In both pigeons it was found that the left entopallium is dominant to the right entopallium, as it has been described in the literature (cf. section 2.1.2.1). It is believed that the sensory input from both eyes is integrated in the visual system of the left hemisphere to enhance the performance in tasks where the binocular information is beneficial[31]. The introduction of HDfUS to this research field of brain lateralization allows investigations at a more profound level. With the setup established at the University of Konstanz, the response in pigeons can be studied over weeks with the same animal and with any type of picture or movie stimulation. This is facilitated by the two screens installed around the pigeon head to cover the majority of the animal's field of view (cf. section 3.1.5.1). An interesting future experiment in this context would be to study the response in the brain to a visual looming stimulation (i.e. objects growing in size to provoke a perception of collision) under monocular and binocular conditions. In addition to the brain asymmetry, a looming effect is also interesting in terms of time perception, because it imposes a time-to-collision sensation for the animal.

## 4.3 Functional Ultrasound - Auditory Stimulation

The study of speech acquisition in human infants has strong parallels to the learning process of the song characteristics in some birds[55,84]. In consequence, the neural substrates responsible for birdsong development are a prominent model system to examine learning and memory[85] and a sensitive and fast neuroimaging of the bird's auditory system is of distinct importance. In typical in vivo studies, the auditory system of the bird is studied by electrophysiological recordings[86] or fMRI[28], which offer very limited field of view and/or spatiotemporal resolution. In this section, the neural activity evoked by auditory stimulation is analyzed with HDfUS. The results of one out of three pigeons (male) are discussed and subsequently of one female zebra finch, which – as a songbird – has a more involved auditory pathway structure (cf. section 2.1.2.2).

### 4.3.1 Pigeon

In Fig. 41a, an HDfUS acquisition of an awake pigeon, stimulated for 15s with the sound of an adult hawk scream is shown. The PD image (grey) shows the vascularity of a slice through the pigeon brain. The colored overlay in the image represents the activated regions in the brain

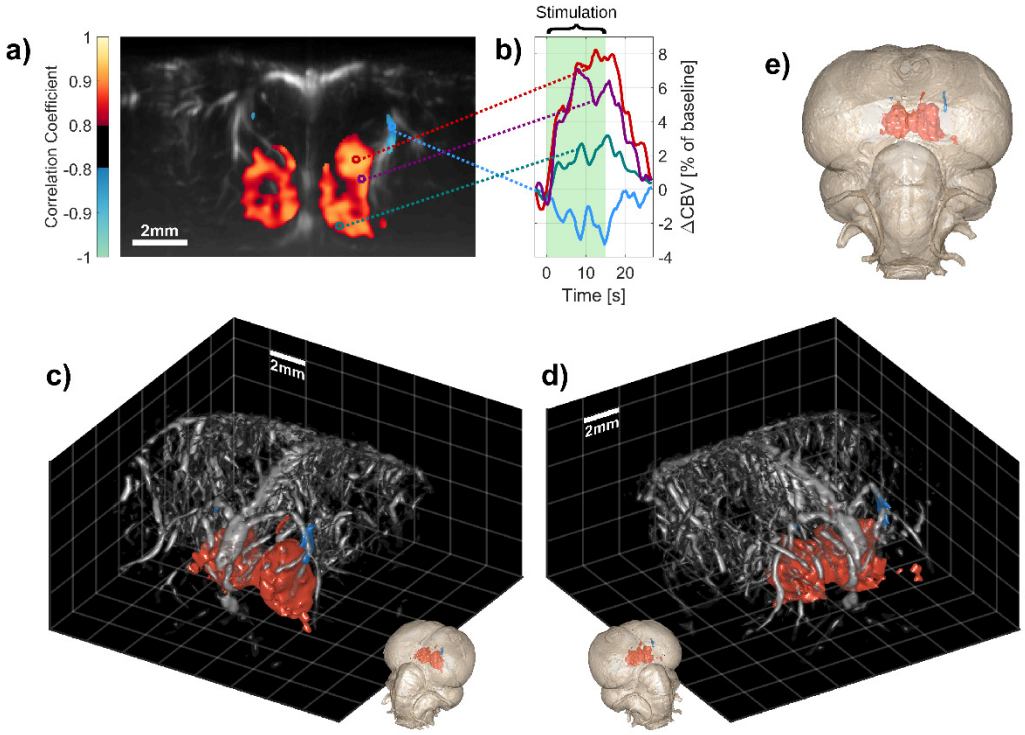


***Figure 41 | 2D and 3D HDfUS Responses in the Auditory System***

***a)*** *PD image (grey) and activity overlay.* ***b)*** *Temporal course of response in different ROIs.* ***c/d)*** *3D reconstruction of the response from 18 slices mapped to an MRI brain surface (**e**). See text for details.*

evaluated by the Pearson correlation coefficient (cf. section 2.2.6) over a single stimulus (threshold at $|r| > 0.75$, red/yellow and blue/green correspond to positive and negative correlation, i.e. CBV increase/decrease). The CBV change in Fig. 41b reveals the shape of the hemodynamic responses within four ROIs and the green bar indicates the time of auditory stimulation. Scanning through the brain in steps of 500µm with 18 HDfUS acquisitions images the whole three dimensional response at great detail (Fig. 41c and d). The mapping of the HDfUS datasets to an MRI pigeon brain (Fig. 41e, cf. section 3.1.4) shows the location of the activated areas within and around the field L[76], in accordance to the established associative processing of these sound patterns. The different ROIs in Fig. 41a/b furthermore show a non-uniform hemodynamic response within the activated area, with signal peaks at different times during the stimulation sequence. To the best of my knowledge, this study also shows for the first time a drainage of the CBV within a supplying larger artery/arteriole during activation (see blue negative values in Fig. 41), demonstrating the importance of a high spatial resolution in functional neuroimaging. For methods such as fMRI that sample a larger voxel size, this drainage effect could potentially lead to a decreased functional signal as the negative and positive change would partly cancel out. Thus, activated brain regions with an associated nearby decrease in CBV are more difficult to investigate or even identify.

In order to evaluate the difference in neural activation between an unknown sound stimulus (noise) and a known sound (hawk), the awake pigeon is exposed to a noise sound of the same frequency spectrum and amplitude as the hawk sound (Fig. 42). For both cases the response

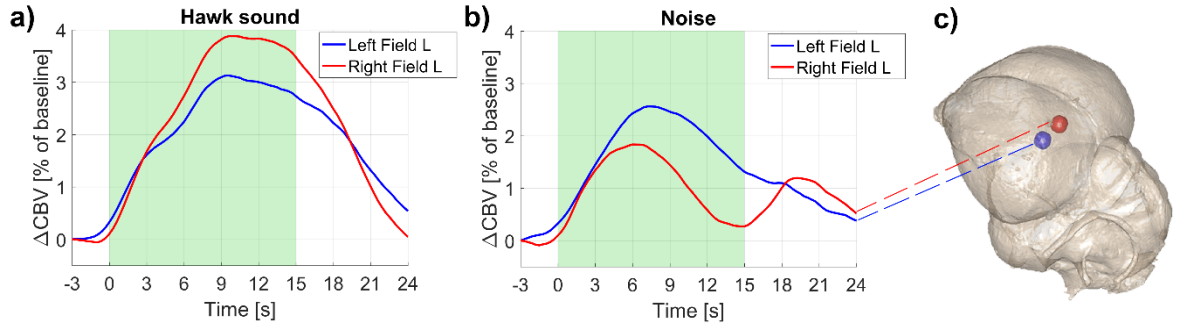


***Figure 42 | Hawk Sound vs. Noise in the Field L***

*The figure shows the average response in a ROI in field L (voxel size 1mm³) evoked by a sound carrying information (**a**, hawk sound) compared to a noise sound with the same power spectrum (**b**, noise). The data is based on single stimulation sequences (i.e. no error bars). **c) T**he location of the ROI in field L mapped to the MRI brain.*

starts similarly within the field L, but levels off earlier and shows a second feature after the sound stops at 15s for the noise case (more prominent in the right field L). This would be expected because there is no variation and/or information during the noise sound, leading to habituation. The only variations causing brain activation are the start and the stop of the noise, thus leading to the two associated peaks approximately five seconds after the start and stop.

The activity evoked by the hawk sound was reproduced in all three pigeons (one anesthetized and two awake) resulting in the same characteristics of the hemodynamic response in terms of shape and localization. However, the amplitude of the signal change in the anesthetized pigeon was about 50% smaller than in the awake subjects, which is believed to be due to the attenuated neurovascular coupling (cf. section 2.1.1).

### 4.3.2 **Zebra Finch**

Because of the similarity to humans in language learning and vocalization, songbirds are the more relevant model in the context of auditory stimulation compared to pigeons. Within the scope of this project, a pilot study was performed to evaluate the potential of HDfUS for zebra finches at the Max Planck Institute for Ornithology in Seewiesen, Germany. HDfUS datasets of the cerebral system were recorded over 17 slices in 250µm steps of a female bird stimulated by the bird's partner song.

Figure 43a shows the response in seven brain slices, measured by HDfUS over an average of six stimulations. The positions of the slices within the brain are indicated on the right of Fig. 43a and the zero position was defined to be the location of the main bifurcation in vascularity as a well recognizable landmark. The angle in the stereotactic coordinates was around 45°, but could not be defined accurately in this pilot study.

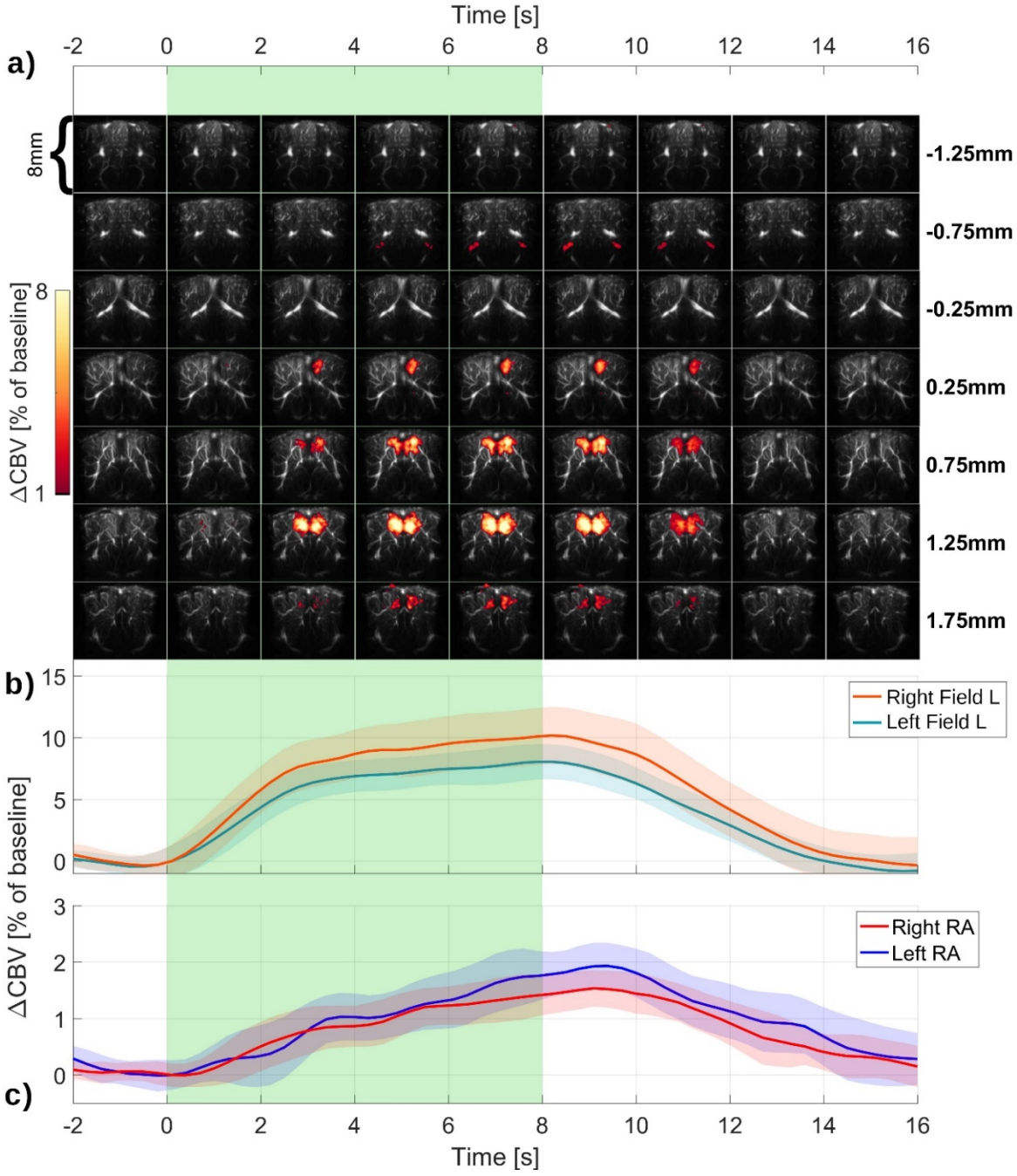


***Figure 43 | Auditory Stimulation of an Anesthetized Zebra Finch***

***a)*** *Seven brain slices showing the temporal course of the response in two sets of nuclei, the field L and the RA.* ***b/c)*** *ΔCBV in the field L and RA regions. Note that the RA has a fivefold smaller signal increase compared to the field L region. Data was obtained at the MPI for Ornithology Seewiesen in collaboration with the group of Prof. Gahr.*

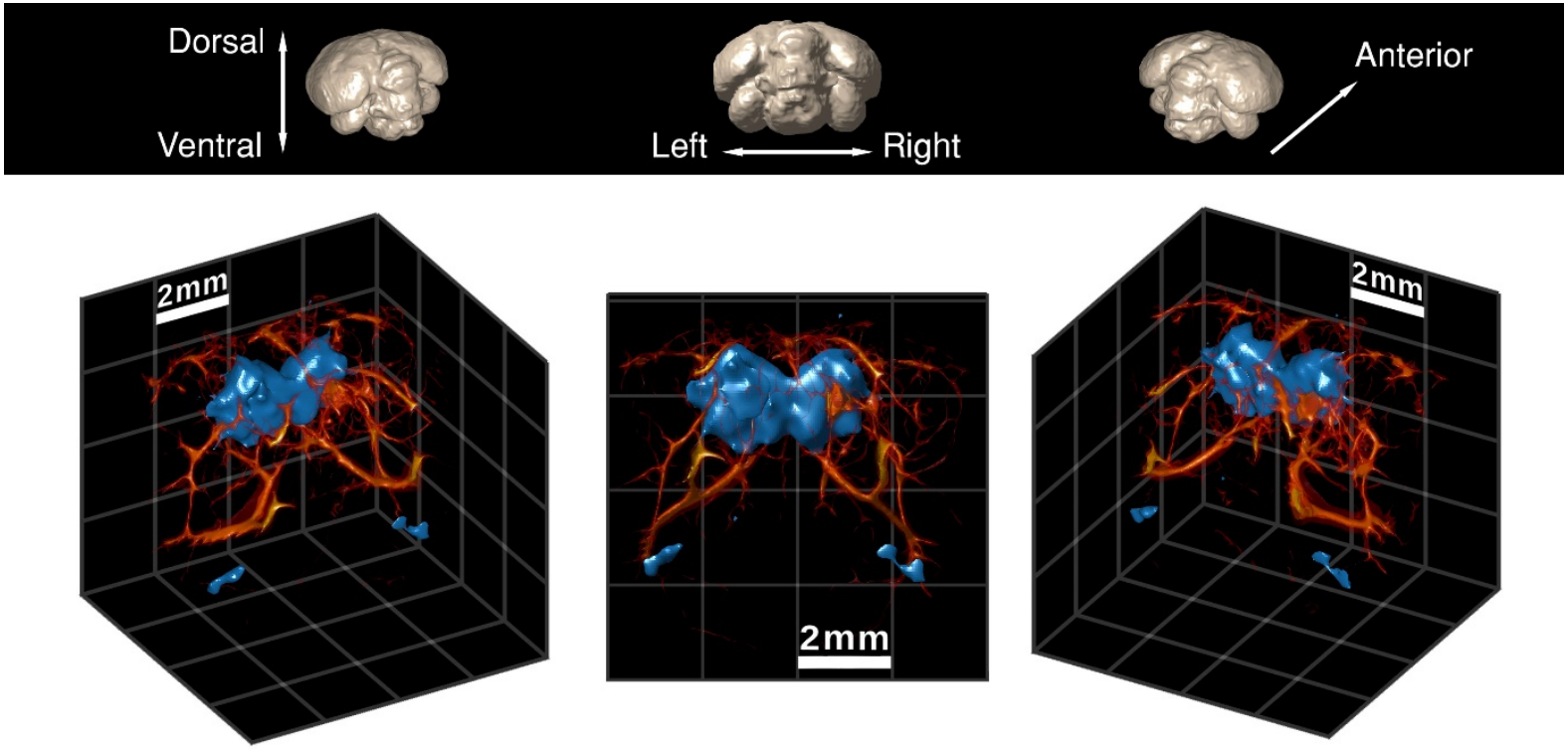


***Figure 44 | 3D Representation of the Activity in Zebra Finch Brain.***

*The 3D reconstruction of the activity in the zebra finch brain with the vascularity shown in red and the activity in blue. MRI brain surfaces from [87] are shown on top for orientation. HDfUS data was obtained at the MPI for Ornithology Seewiesen in collaboration with the group of Prof. Gahr.*

The large activated region in Fig. 43a corresponds to a strong activity of up to 10% in the field L, which stretches from 0.25mm to 1.75mm in the coordinate system. The smaller, further separated region at -0.75mm represents the robust nucleus of the arcopallium (RA) in the zebra finch with a smaller response of up to 2%. The $\Delta$CBV in the field L and RA regions is additionally depicted in Fig. 43b and c, respectively. It is resolved that the response within the RA has a different shape compared to the field L, which exhibits a steeper signal increase and earlier saturation, whereas in the RA, the ΔCBV is continuously increasing with a lower saturation level.

Figure 44 shows a 3D reconstruction of the HDfUS datasets in the 17 brain slices for better comprehension of the spatial integration. The vascularity is depicted in red (derived from 3D skeletonizing the PD images and not the tomography approach from section 2.2.7) and the activity in blue with the correlation coefficient above $|r| > 0.45$ (cf. section 2.2.6). The main areas of activation are the field L as well as the deeper and laterally more separated symmetric regions within the RA of the zebra finch brain. Above the vascularity maps, an MRI brain surface dataset of a zebra finch brain from [87] is shown for orientation. A mapping onto the MRI datasets could not be carried out, because the positions and angle were not measured accurately enough within this experiment. This and the fact that only one animal was studied also make it difficult to validate the neural pathway structure introduced in section 2.1.2.2 for songbirds. Still, the results clearly show the great potential of HDfUS for zebra finch studies, allowing to resolve different responses in spatially separated brain areas at excellent spatiotemporal resolution.

### 4.3.3 Auditory Stimulation - Discussion and Outlook

With the study of the auditory stimulation, the advantage of HDfUS in terms of spatiotemporal resolution was utilized to investigate general hemodynamic response characteristics of different nuclei. This allows a more profound understanding about the associated tasks and the purpose of certain brain areas. This is especially useful in the context of primary and secondary processing in the brain, i.e. direct projections of the sensory input to certain nuclei vs. neural substrates that integrate the information of several associated nuclei. First experiments on this issue were carried out on an awake pigeon stimulated by varying sound patterns, such as hawk sound vs. noise (section 4.3.1). It was found that the response in the field L (the equivalent to the auditory cortex in mammals) exhibits different characteristics, depending on the type of sound. Thus, it can be assumed that the field L with the surrounding nuclei is composed of neural substrates corresponding to the sensory input of sound in general and additional substrates processing known sound patterns. To study this issue in depth, pigeons are a suitable model, because the only neural substrate related to auditory sensory input is the field L (cf. section 2.1.2.2), thus the necessary imaging volume is smaller. For future studies, the datasets would need to be extended to more animals and a larger set of stimulation patterns. A possible approach would be to first map certain frequency bands or even single frequencies of a noise sound to corresponding nuclei, which would be the most basic information retrievable from the system. Subsequently, the sound amplitude of certain frequency band stimulations as well as the band itself could be modulated over time to continually increase the resemblance to a known sound pattern. Typically, such a thorough analysis is too cumbersome, because standard

neuroimaging/ sensing methods, such as fMRI or electrophysiological recordings do not offer the spatiotemporal resolution. With HDfUS such studies become feasible and thus the general knowledge about auditory processing in the brain could be extensively enhanced.

The possibilities with auditory stimulation in the context of songbirds are even manifolded, because of the corresponding wide network of neural substrates in a complex pathway structure (cf. section 2.1.2.2). This allows songbirds to learn their own vocalization and to accurately discriminate between songs of the partner and unknown conspecifics. In a pilot study at the MPI for Ornithology Seewiesen, Germany, an individual zebra finch was stimulated with the partner song, resulting in an HDfUS measured activity in two brain areas, the RA and the field L (section 4.3.2). It was found that the response in the RA is smaller and increasing slower compared to the field L, which can be attributed to different aspects: First, that the vascular anatomy around the RA is differently assembled, thus leading to an attenuated response, or second, that the RA is associated to different tasks, thus resulting in a deviating response. Most likely both aspects contribute to the differences, which could be thoroughly analyzed in a feasible way with HDfUS similar to how it was described for the pigeons. Current functional studies at the MPI for Ornithology Seewiesen have mostly focused on electrophysiological recordings, which is cumbersome due to the restricted field of view. Future HDfUS studies in this collaboration would allow to investigate the brain activity of several relevant neural substrates in zebra finches simultaneously, thus contributing to a profound knowledge about the neural basis of vocalization perception and adaptation.

## 4.4 Functional Ultrasound - Magnetic Stimulation

To study magnetoreception in birds, HDfUS measurements were carried over the top central area of the cerebrum (see Fig. 45). Within the imaged volume, the recorded hemodynamics exhibited no variations that would indicate functional response, i.e. no brain activity could be resolved that corresponds to magnetoreception. It was, however, observed that the PD signal

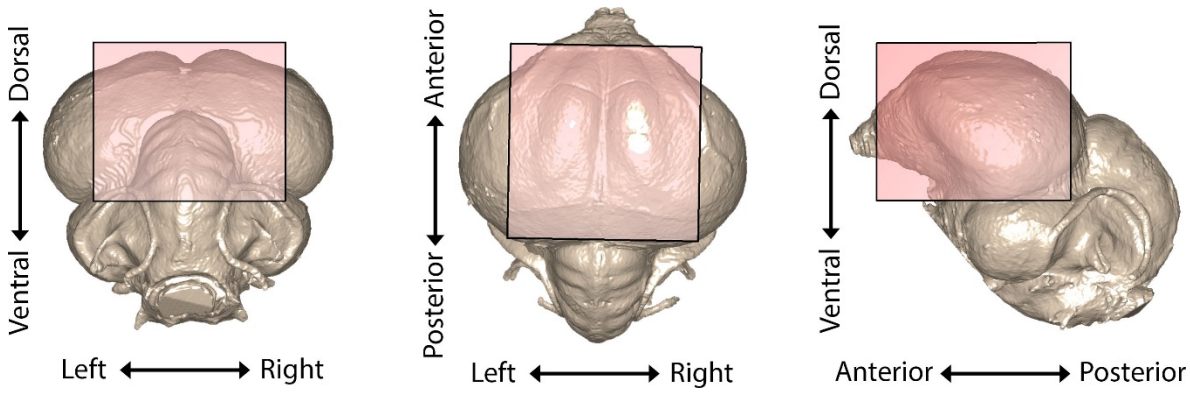


***Figure 45 | Pigeon Brain Volume Studied with HDfUS***

*Three perspectives (back, top and side view) of the pigeon brain. The red overlay indicates the volume that was studied with HDfUS in the context of magnetic stimulation.*

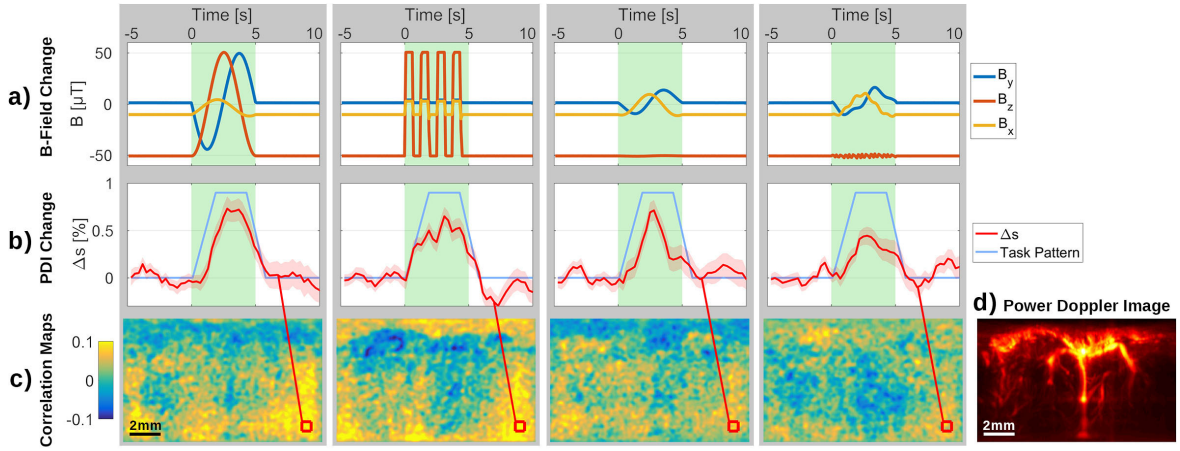


***Figure 46 | Artefactual HDfUS Results on Pigeons with Different Magnetic Field Changes***
***a)*** *The four different magnetic field changes.* ***b)*** *The corresponding PD signal from a noise region.* ***c)*** *The Pearson correlation maps with values ranging from -0.1 to 0.1 (task pattern used for correlation shown in blue in* ***b****). The noise regions from* ***b*** *are indicted in the maps.* ***d)*** *PD image with the same scaling as images in* ***c****.*

is in general slightly modulated with a change of the magnetic field vector. Interestingly, such effects were also detected in static phantom measurements, where the PD signal is solely composed of noise. As such, PD signal modulations can easily be mistaken for an actual neurovascular response in pigeon HDfUS experiments and the observations will be briefly discussed in the following.

Figure 46a shows four different magnetic field changes over the time course of 5s with the different axis direction of the magnetic field $B_{x,y,z}$ (cf. section 3.1.5.3). The absolute field amplitude is constant at 51.8µT, only the direction of the vector is changed in various ways. From the pigeon's point of view, the magnetic field changes pattern should be perceived as motions of barrel roll flying in combination with a looping, being flipped around or circle flying without and circle flying with a slight wobbling modulation (in this order). The average effect of those patterns on the PD signal within a noise region (30 stimulations for each dataset) is shown in Fig. 46b with the same time scaling. Depending on the magnetic field change, the PD amplitude is differently modulated with relative signal increases up to 0.8% from the baseline level. The Pearson correlation maps in Fig. 46c indicate that the responses are located at the edges of the image area, which represent the low amplitude regions in the PD image (Fig. 46d), i.e. noise.

In Fig. 47, the data from the first magnetic field change pattern from Fig. 46 is analyzed more detailed with a plot of the correlation coefficient values vs. the PD amplitude for all the pixels in the image. Higher values on the x-axis represent larger PD amplitudes in a pixel, i.e. more CBV. The lower values correspond to a lesser amount of CBV and from a certain threshold (< 5dB) onwards noise. From Fig. 47, it can be seen that the higher correlation coefficient values correspond to noise PD pixels and that there is no response in the actual blood vessels. Thus, the response is categorized as an artefact. The cause of this artefact could be an induction or crosstalk effect, but was not further investigated, because it can be easily filtered out by

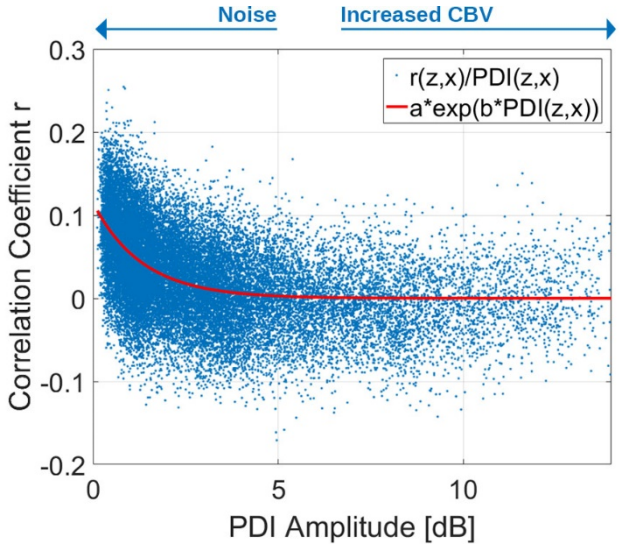


***Figure 47 | Correlation Coefficient vs. PD Amplitude***
*In the scatter plot (blue) the correlation coefficient values vs. the PD signal amplitude for all the pixels in the image from the first dataset in Fig. 46 are shown. Clearly, higher correlation values correspond to lower PD amplitudes, i.e. noise. The first degree exponential fit (a = 0.11, b = -0.75) in red supports this argument.*

masking the correlation maps to only include PD pixels with a certain amplitude (for instance > 5dB). To suppress these artefactual responses in HDfUS datasets, especially for magnetic stimulation, it is advised to thoroughly analyze the corresponding signal amplitudes of the PD image and exclude the noise pixels.

### 4.4.1 Magnetic Stimulation - Discussion and Outlook

The HDfUS measurements in the context of magnetic stimulations were performed on pigeons in the central cerebral parts and anterior sections of the cerebellum. No actual responses in the vascular system were observed that would indicate the type of magnetoreceptive mechanism used by navigational birds. Possible reasons are manifold: First, a response occurs in the brain, but is located in an area that has not been imaged by HDfUS. Second, the magnetoreceptive sense of the pigeons was degenerated, because they have been spending most of their lives in the loft without continual training of the navigational performance. Third, the parameters for the magnetic stimulation have not been optimal leading to an attenuated response that is below the sensitivity of HDfUS (a similar effect has been observed in a rat at electrical forelimb stimulation, see appendix 8.1).

Thus, future experiments on this issue should first of all concentrate on imaging the remaining brain areas, i.e. tectum and cerebellum, to determine if the neural processing of the magnetoreception is located in those areas. The tectum and the cerebellum were not yet investigated in detail, because they are challenging to penetrate through the selected trepanation area. Performing a trepanation at the sides or further back is necessary, but is also more involved, because of the muscle tissue layer between the skull and skin at those areas. In principle, however, nothing speaks against performing measurements in these regions.

Additionally, future experiments should be carried out on animals with excellent navigational performance to ensure that the neural substrates corresponding to magnetoreception have not degenerated. Another idea would be to perform measurements on long-distance-migration birds in the migration period. The processing capabilities in the corresponding neural substrates

should be enhanced in this season and thus leading to an increase response measurable by HDfUS.

Finally, the stimulation patterns could be optimized in future studies to induce a stronger response in the bird brain. One idea here would be to combine visual and magnetic stimulations to better resemble the natural sensory input. A point-of-view-shot movie of a bird flying in a circle could for instance be projected on the screens with the corresponding magnetic field vector change as a stimulation. An interesting study would be to compare the responses of magnetic field vector rotation in correspondence with the expectation or in an unexpected manner (i.e. the other way around). A difference map of the neural activation from the two stimulations could give first indications on the involvement of certain nuclei with respect to magnetoception.

## 4.5 General Concluding Remarks

In this chapter, the neural activation has been studied by the means of HDfUS with evoked responses in the visual and auditory system of pigeons and zebra finches. Additionally, first HDfUS measurements are presented towards studying magnetoreception in birds. In terms of open questions in the field of the avian neurobiology, it is too early to draw conclusions about the revelation of unknown pathways or cerebral nuclei associations. For this, the number of animals and acquisitions per animal were insufficient and did not allow an in-depth evaluation including robust statistics to compensate individual differences or outliers. Still, these pioneering results of fUS in the scope of avian brain imaging already demonstrate the huge potential based on several proof of concept experiments.

Concluding comments and possible future studies have already been discussed for each stimulation pattern above. In a more general context about HDfUS as a novel neuroimaging method as well data analysis and setup improvements, some additional remarks are worth a deeper consideration.

### 4.5.1 HDfUS as a Novel Neuroimaging Method

As discussed in the context of visual stimulation, one outstanding feature of the HDfUS is the possibility to investigate temporal spreading of the response in defined single brain areas of individual animals. Additionally, HDfUS is especially beneficial with respect to drainage effects, where neighboring areas exhibit positive as well as negative responses. This was demonstrated with the response in field L of a pigeon evoked by an auditory stimulation (cf. section 4.3.1), where the supplying arteriole showed a significant drop of the CBV. Functional neuroimaging techniques based on the measurement of CBV in large voxels would suffer from an averaging effect of the positive and negative signal contributions within a sampling volume. This has also

validity for the gold standard in neuroimaging, fMRI, which measures a composite of CBV and the deoxyhemoglobin concentration (cf. section 2.1.1).

A novel possibility of studying the brain connectivity is also offered by the excellent spatiotemporal resolution of HDfUS in combination with the placement of an electrode at a defined brain area. An electrical stimulation could be induced by the electrode locally and responses resulting from functional connectivities of distant brain areas could be directly observed using HDfUS. A pilot study of such a measurement was performed on a mouse (appendix 8.3) and delivered results of great potential.

To quantify the benefit of HDfUS, an essential future study is to benchmark its sensitivity, SNR and resolution with established neuroimaging methods, such as fMRI, using the same stimulation setup and animals. Due to the different physiological parameters measured by the two methods, it is otherwise impossible to accurately compare the SNR, sensitivity and spatiotemporal resolution. The Güntürkün group from the Ruhr University Bochum, Germany, has expertise in fMRI imaging of birds and a collaboration directed towards benchmarking HDfUS is planned.

### 4.5.2 Data Analysis and Setup Improvements

In terms of data analysis, the measured CBV is so far only correlated with the induced stimulation, imposing that the evoked response is strong enough to exceed all the other CBV variations, i.e. the baseline value. All the intrinsic (change in heartrate, breathing rate, eye and eyelid movement, etc.) or extrinsic (ambient sound and light, etc.) parameters are not taken into account, even though a lot more data is recorded with the experimental setup established at the University of Konstanz (cf. section 3.1). With extended datasets of more animals and acquisitions in the future, it is potentially rewarding to evaluate those characteristics with respect to the recorded CBV. Finding the typical responses in the CBV to certain intrinsic or extrinsic parameters would then allow to stabilize the baseline values. Consequently, the SNR of the fUS measurements is enhanced, leading to a better detection of weak functional responses. In a very rudimental way, such an approach has been used in the context of HDfUS mice experiments (appendix 8.2), where the dataset was separated depending on the eyelid movement of the mouse.

In terms of experimental setup improvements, a next step would be to install the ultrasound transducer temporarily directly on the skull, allowing free movement of the animal, as it has been demonstrated for rats in [19] and [25]. Such systems reduce the stress level of the animal and enable measurements in a semi-natural habitat, which has special significance for studies where the animal is required to perform a task. An interesting experiment would be for instance the investigation of the auditory system and vocalization, when a zebra finch is singing its song. For the freely moving fUS measurements, the motion will be first of all restricted to two dimensions, because the datastream of several GB/s still requires a cable. With the advancements of wireless technology and extended bandwidths, future studies on completely free animals will be feasible.

Another possible improvement of the transducer setup would be to utilize two transducers to image two brain slices simultaneously. This is feasible, because a single Verasonics Vantage ultrasound apparatus offers up to 256 channels in transmit and receive and thus has the capacity for two 128 channel transducers. Such a system would allow to study distant brain areas at the same time or can be used to increase the sensitivity at an overlap region. The principle feasibility of such a dual transducer system was evaluated at the beginning of the project in the context of velocity vector estimation in carotid artery imaging with two low frequency transducers (appendix 8.4).

Another outlook for the improvement of the experimental setup is the introduction of matrix array transducers for fUS imaging. Such arrays already show excellent results of directly recording 4D dynamics in larger vessels[75] and an expansion of the technology to small animal imaging in the near future is foreseeable. For this application, lower frequencies are advisable as a starting point, which impairs the spatial resolution by increasing the imaging voxel size, but also leads to a larger field of view at a limited channel number.

# 5 SUMMARY

The objective of this thesis was to establish a functional ultrasound (fUS) setup capable of detecting cerebral hemodynamic changes evoked by neural activity in the avian brain. To accomplish successful studies, the fUS method was advanced in this project with the introduction of a new data acquisition scheme to enhance the spatiotemporal resolution. For the first time, this enabled successful studies of species with unfavorable physiological characteristics for fUS, such as pigeons. The new acquisition scheme developed in this project was termed high definition fUS (HDfUS) and was established on a commercial ultrasound research system.

The implementation of HDfUS utilized parallel processing on two GPUs and allowed real time processing of a raw datastream of up to ∼3GB/s. Live imaging and data evaluation was realized in order to obtain instantaneous information about the neurovascular response of the animal, which is especially important for studies of stimulations where the localization of the response is unknown. The latest HDfUS version additionally used C++/CUDA algorithms to optimize frame rates and bypass the parallel computing limitations of MATLAB. This facilitated saving the datastream at 1kHz frame rate and $(100\mu m)^2$ resolution for an in-depth post-acquisition analysis.

To illustrate the necessity for HDfUS in pigeons, the implications of different physiological parameters were analyzed by modelling the cerebral blood volume (CBV) and defining a signal-to-noise ratio (SNR) for fUS measurements. It was found that due to the slower heartrate of pigeons, SNR values were a factor of 3+ impaired compared to rats. With the introduction of HDfUS, high SNR values were retrieved for pigeons and an improvement of about 6 compared to conventional fUS was evaluated.

To validate the hypothesis of the strong heartrate influence in the model, in vivo data was acquired and compared for a rat (wistar) and a pigeon (columba livia domestica). Similar to the CBV model, an SNR was defined for functional responses evoked by stimulations that are known to be strong for the respective species. For the rat, it was shown that the SNR can be slightly improved with the new HDfUS acquisition scheme compared to the conventional case. For the pigeon, an SNR gain of about four was observed, which indicates that for certain species, HDfUS makes all the difference between success and failure.

The potential of HDfUS in the context of avian neurobiology was demonstrated in this project by analyzing the activated regions of an anesthetized pigeon with a stimulation of a static light source. Exploiting the high spatiotemporal resolution offered by HDfUS, it was possible to resolve in detail the 3D temporal spreading of the complex hemodynamics within the activated visual wulsts, which has not been revealed previously by any other method.

To determine how HDfUS can be utilized in the research field of brain asymmetry[54], awake pigeons were studied with a stimulation of a dynamic light source. In accordance with previous studies, it was found that the right entopallium is inferior to the left entopallium, which is integrating the sensory input from both eyes to enhance performance in tasks where the binocular information is beneficial[31]. The study with the moving light source also demonstrated the advantage of the enhanced spatiotemporal resolution of HDfUS, which allowed to image the temporal spreading of complex responses at a large field of view. Typical other neuroimaging/sensing methods such as functional magnetic resonance imaging or electrophysiological recordings either do not offer the necessary frame rate or field of view, such that brain asymmetry studies with such complex stimulation patterns are not feasible.

The second sensory system studied in this project was aimed at the auditory perception of avian species. The first study in this context was focused on the neural substrate field L of awake pigeons, which is believed to be the equivalent to the auditory cortex of mammals[56]. With a single stimulation of a hawk sound and a noise sound in the same frequency spectrum, it was found that a habituation occurs when the sound does not contain any information (i.e. noise). The difference in response between the two stimulations was observed to be very small (1%-2% in $\Delta CBV$), thus demonstrating that a high definition neuroimaging method is essential. Studies in this context are relevant to differentiate between neural substrates solely corresponding to the sensory input of the sound (i.e. noise sound) and those related to a sound that is known to the animal (i.e. hawk sound for pigeons).

With the study of the neural substrate field L in the awake pigeon brain, an additional feature was observed, which can be crucial for functional neuroimaging methods that rely on the neurovascular coupling. The artery/arteriole neighboring and supplying the vascularity in the field L area showed a strong negative response, most likely as a cause of drainage during activation. With HDfUS, the vessel was clearly discriminable from the activation area, which demonstrates that in such cases a high spatial resolution is essential. Thus it was shown that neuroimaging methods sampling larger voxels can lead to attenuated or even false negative results due to averaging of positive and negative signal contributions.

In the context of functional studies of the auditory systems, the feasibility of HDfUS was additionally evaluated on zebra finches, a songbird species, in collaboration with the Gahr group from the MPI for Ornithology Seewiesen, Germany. Two responding sets of neural substrates were detected in the anesthetized zebra finch when stimulated with the partner song, the RA and the field L. It was observed that the field L response was five times larger compared to RA and exhibited a different temporal course. This demonstrated that studies on zebra finches could benefit from HDfUS imaging by investigating several neural substrates

simultaneously, which is challenging to achieve with the typically used electrophysiological recording method. Thus, HDfUS could contribute to a profound knowledge about the neural basis of vocalization perception and development.

With respect to studying the mechanism of magnetoreception, no HDfUS response was observed in the central cerebral areas with a stimulation changing the magnetic field vector direction in different patterns. A list of suggestions about optimizing the experimental setup to facilitate the detection of a possible response in the context of magnetoreception was given in this thesis. In addition, an artefactual signal influence due to magnetic stimulations was discussed in order to prevent false positive results in future HDfUS studies.

In summary, this thesis was devoted to establishing, advancing and validating an fUS system capable of imaging functional responses in the avian brain. The enhancements of the fUS method led to the development of a high definition fUS scheme, termed HDfUS. This new algorithm paves the way for in-depth research of numerous aspects in the field of avian neurobiology, including brain asymmetry, vocalization learning and magnetoreception. HDfUS as a novel neuroimaging scheme was discussed in this thesis to be advantageous in several facets compared to established methods. Especially the excellent spatiotemporal resolution of HDfUS was shown to be particularly beneficial in the context of imaging the temporal spreading of a complex response in the cerebral microvasculature.

# 6 ZUSAMMENFASSUNG

Das Ziel der vorliegenden Arbeit war es, ein funktionelles Ultraschall (fUS) Setup zu entwickeln. Dies sollte ermöglichen, die Änderungen der zerebralen Hämodynamik von Vogelarten als Reaktion auf äußere Reizen zu detektieren. Für den Erfolg der Studie war die Weiterentwicklung und Optimierung der fUS Methode maßgeblich entscheidend. Im Verlauf dieses Projektes wurde dazu ein neues Datenerfassungsprotokoll mit einer höheren raumzeitlichen Auflösung erarbeitet. Dieses neue Protokoll wurde auf einem kommerziell vertriebenen Ultraschallgerät für Forschungszwecke entwickelt und *high definition* fUS (HDfUS) benannt. Im Rahmen dieser Arbeit wurden mit HDfUS erstmalig erfolgreiche Studien an einer Tierart mit für fUS unvorteilhafter Physiologie durchgeführt.

Der HDfUS Algorithmus basiert auf paralleler Datenverarbeitung und setzt zwei GPUs (graphics processing units) voraus. Dies ermöglicht eine Echtzeit-Prozessierung von einem Rohdatenfluss von bis zu ∼3GB/s. Des Weiteren erhält man durch die Echtzeit-Bildgebung und -Datenanalyse sofortige Information über die neurovaskuläre Antwort. Dies ist besonders wichtig in Studien, bei welchen die Lokalisierung der Antwort noch unbekannt ist. Die aktuelle Version des HDfUS Algorithmus basiert auf C++/CUDA, wodurch zum einen die Bildwiederholrate weiter optimiert werden konnte und zum anderen die Einschränkungen zur parallelen Prozessierung innerhalb MATLABs umgangen werden können. Dies ermöglicht die Speicherung der Ultraschallbilder bei einer Bildwiederholrate von 1kHz und einer räumlichen Auflösung von $(100\mu m)^2$ für eine detaillierte Nachverarbeitung der Daten.

Um die Notwendigkeit von HDfUS bei Brieftaubenstudien zu illustrieren, wurden in dieser Arbeit zunächst die Auswirkungen der Physiologie betrachtet. Dazu wurde ein Modell zur Dynamik des zerebralen Blutvolumens (englisch: cerebral blood volume, CBV) aufgestellt und das Signal-zu-Rausch Verhältnis (englisch: signal-to-noise ratio, SNR) für fUS Datenerhebungen analysiert. Durch das Modell wurde vorausgesagt, dass die langsamere Herzfrequenz von Brieftauben im Vergleich zu Ratten die fUS SNR Werte um einen Faktor 3+ verschlechtern. Weiterhin konnte gezeigt werden, dass die SNR Werte für Brieftauben mit dem HDfUS Algorithmus gegenüber konventionellem fUS um einen Faktor 6 verbessert werden konnten.

Um die im Modell aufgestellte Hypothese des Herzfrequenzeinflusses zu validieren, wurden in vivo Messungen an einer Ratte (Wistar) und einer Brieftaube (columba livia domestica) durchgeführt und verglichen. Die Stimulation bestand aus einem von der jeweiligen Spezies stark empfundenen Reiz. Ähnlich zum CBV Modell wurde auch hier das SNR bei der

funktionalen Antwort analysiert. Es konnte gezeigt werden, dass die SNR Werte bei der Ratte durch HDfUS gegenüber konventionellem fUS leicht verbessert werden konnten. Bei der Brieftaube hingegen wurde eine SNR Anhebung von einem Faktor 4 beobachtet, was darauf hindeutet, dass HDfUS für bestimmte Tierarten unumgänglich ist.

Das Potenzial von HDfUS im Hinblick auf Studien zur Neurobiologie von Vögeln wurde in dieser Arbeit zunächst an anästhesierten Brieftauben untersucht. Als Stimulation wurde eine statische Lichtquelle verwendet. Es konnte gezeigt werden, dass die exzellente raumzeitliche Auflösung von HDfUS ermöglicht, die zeitliche Ausbreitung der Aktivität im visuellen Wulst in 3D zu verfolgen. Die detaillierte Auflösung einer solch komplexen hämodynamischen Antwort innerhalb des visuellen Wulstes konnte so bisher durch keine andere Methode gemessen werden.

Um zu ermitteln, wie HDfUS in Bezug auf funktionale Asymmetrien des Gehirns[54] angewandt werden kann, wurden Wachmessungen an Brieftauben durchgeführt, die mit einer sich bewegenden Lichtquelle stimuliert wurden. In Übereinstimmung mit bisherigen Funden konnte gezeigt werden, dass das rechte Entopallium gegenüber dem linken Entopallium eine untergeordnete Funktion hat. Als Grund dafür wird angenommen, dass im linken Entopallium der sensorische Input beider Augen integriert wird, um die Leistung bei Aufgaben zu verbessern, bei welchen die binokulare Information nutzbringend ist[31]. Die Studie mit der sich bewegenden Lichtquellen zeigte weiterhin den enormen Vorteil der verbesserten raumzeitlichen Auflösung von HDfUS, die ermöglichte, den zeitlichen Verlauf der komplexen neurovaskulären Antwort in einem großen Bildfeld aufzunehmen. Gewöhnlichen anderen neurobildgebenden Verfahren, wie z.B. funktionale Magnetfeldresonanztomographie oder elektrophysiologisches Ableiten, ermangelt es im Vergleich zu HDfUS entweder an der benötigten hohen Bildwiederholrate oder aber an einem ausreichend großen Bildausschnitt, sodass Studien zu funktionalen Gehirnasymmetrien mit komplexen Reizmustern nicht umsetzbar sind.

Das zweite in dieser Arbeit diskutierte sensorische System bezog sich auf die auditorische Wahrnehmung von Vögeln. Die erste Studie in diesem Kontext war auf den Nucleus Field L in wachen Brieftauben fokussiert. Vom Field L wird angenommen, dass es das Vogeläquivalent zum auditorischen Kortex in Säugern darstellt[56]. Mit einem Reiz eines Habichtschreis und eines Rauschgeräusches in demselben Frequenzspektrum konnte gezeigt werden, dass ein Gewöhnungseffekt im Field L eintritt, wenn das Geräusch keine Informationen beinhaltet (d.h. Rauschen). Der Unterschied zwischen den beiden Reaktionen im Field L betrug jedoch lediglich 1-2% im CBV, sodass auch hier demonstriert werden konnte, wie wichtig eine hohe Definition und Auflösung des neurobildgebenden Verfahrens ist. Studien in diesem Kontext haben Relevanz in Bezug auf eine genaue Differenzierung und Lokalisierung der neuronalen Substrate, die nur für den sensorischen Input (d.h. Rauschen) verantwortlich sind und für jene, die zudem bekannte Geräusche (d.h. Habichtschrei) verarbeiten.

Mit der Studie des Nucleus Field L in wachen Brieftauben konnte des Weiteren eine Eigenschaft beobachtet werden, die die Güte anderer neurobildgebender Verfahren maßgeblich

beeinflussen kann. Die dem Field L benachbarte und zuliefernde Arterie/Arteriole wies während des Reizes eine starke negative Reaktion auf, wahrscheinlich als Folge der starken CBV Erhöhung im aktivierten Nucleus. Mit der guten räumlichen Auflösung von HDfUS war das Gefäß klar vom aktiviertem Bereich differenzierbar. Bei neurobildgebenden Verfahren, die mit größeren Volumenelementen samplen, könnten solche Vorkommnisse jedoch zu Falschaussagen führen, da die Amplitude der CBV Erhöhung im aktivierten Bereich durch die angrenzende CBV Erniedrigung in der zuliefernden Arterie/Arteriole abgeschwächt ist. Im äußersten Fall kann dies auch zu falsch-negativen Resultaten führen.

Neben den Brieftauben wurde im Rahmen einer Kooperation mit der Gahr Gruppe vom MPI für Ornithologie Seewiesen auch das auditorische System von Zebrafinken, einer Singvogel-Spezies, untersucht. Dabei wurden zwei Sätze von aktivierten Nuclei in einem anästhesiertem Zebrafinken mit HDfUS untersucht, RA und Field L. Es konnte gezeigt werden, dass die Reaktion im Field L gegenüber dem RA um das Fünffache erhöht war und dass der Verlauf der Antwort in den Nuclei verschiedene Charakteristiken aufwies. Dies belegt, dass Studien an Zebrafinken mit der HDfUS Bildgebung stark dadurch profitieren könnten, dass die Reaktion in mehreren Nuclei simultan beobachtet werden kann. Dies ist mit dem gewöhnlich eingesetzten Verfahren des elektrophysiologischen Ableitens nur sehr schwer zu verwirklichen. Folglich könnte HDfUS erheblich dazu beitragen, ein tiefgreifendes Verständnis über die Wahrnehmung und Entwicklung von Vokalisierung zu erlagen.

In Hinblick auf die Studie zur Ergründung der Magnetorezeption von Vögeln konnte mit HDfUS bislang noch keine neurovaskuläre Reaktion detektiert werden. Als Reize wurden mehrere verschiedene Änderungen des Magnetfeldvektors gesetzt und dabei der gesamte zentrale zerebrale Bereich des Brieftaubenhirns untersucht. Um in zukünftigen Studien die Thematik der Magnetorezeption weiter zu ergründen, wurde in dieser Arbeit ein Satz an möglichen Setupoptimierungen vorgeschlagen. Zudem wurde ein artifizielles Signal in Folge der Änderung des Magnetfeldvektors ausgemacht und diskutiert, sodass potenziellen zukünftigen falsch-positiven Aussagen vorgebeugt werden kann.

Zusammenfassend war die Arbeit der Einrichtung, Weiterentwicklung und Validierung eines fUS Setups gewidmet, mit dem funktionale Antworten auf äußere Reize in Vogelspezies aufgelöst werden können. Die Optimierungen des fUS Verfahrens haben zu einer neuen Datenerfassungsmethode mit verbesserter Auflösung geführt, welche HDfUS benannt wurde. Dies ebnet den Weg für umfassende Studien im Wissenschaftsfeld der Neurobiologie von Vögeln, wie z.B. die funktionale Gehirnasymmetrie, das Lernen der Vokalisierung und die Magnetorezeption. Es wurde in dieser Arbeit gezeigt, dass HDfUS als neues neurobildgebendes Verfahren gegenüber etablierten Methoden in vielen Aspekten vorteilhaft ist. Vor allem die exzellente raumzeitliche Auflösung von HDfUS wurde als besonders herausragend aufgezeigt. So konnte in dieser Arbeit dargelegt werden, dass HDfUS den zeitlichen Verlauf von komplexen Reaktionen mit äußerster Genauigkeit auflösen kann.

# 7 ACKNOWLEDGEMENT

First of all, I would like to thank Prof. Georg Maret for giving me the opportunity to work on this project. Throughout the time I was part of his group, he was quintessentially supportive and did everything to make our research a success. I especially appreciate his attitude towards novel and original ideas, which led to this exotic project. For the ultrasound part, this meant getting into a new field of research, where little expertise was given in the lab. His mindset that even those subjects can be mastered as well as his trust in his students is something that shines out.

Secondly, I want to thank Dr. Pieter Kruizinga from the Thorax Center, Erasmus MC, Rotterdam, on whom the success of this project significantly depended. I met Pieter in Edinburgh in 2014 at the beginning of my PhD and that was the foundation to a rich and efficient collaboration. Him inviting me to Rotterdam for three months to spend time in a leading ultrasound research group as well as ongoing Skype meetings throughout my PhD allowed us to develop a state-of-the-art ultrasound acquisition.

Furthermore, I would like to thank Dr. Wolfgang Scheffer, who supervised me during my master thesis and convinced me of the potential of this PhD project. Together, we've spend uncountable hours of discussions in the lab and the office to optimize the experimental setup. With Wolfgang's focused and accurate attitude, we've developed a fun targeted-oriented teamwork that led to the results presented in this thesis.

In addition, many thanks go to the whole pigeon group from the LS Maret, namely Dr. Markus Belau for numerous discussions and ideas about the project as well as his input on this thesis; Moritz Schlötter, an immensely friendly office and flat mate with unconventional and creative ideas to approach problems; and Annika Schoe, for her helpful and kind attitude.

I also want to thank everyone else from the whole LS Maret group for the excellent atmosphere inside and outside of the university and particularly during the group excursions. A special thanks goes to Sabine Lucas and Doris Drexler for their extensive help with the bureaucracy.

Additionally, I would like to thank Prof. Paul Leiderer for his interest in this project and for writing the second review of this thesis.

From the collaborations that emerged from this project, I would like to thank the ultrasound research group from the Thorax Center, Erasmus MC, Rotterdam, Netherlands, where I've spent months of my PhD during several visits. Besides gaining knowledge in several aspects of

ultrasound, I've always felt welcome and appreciated in the group. Along with Pieter who was mentioned above, I would like to additionally thank Prof. Antonius van der Steen, Dr. Hans Bosch, Prof. Nico de Jong and Dr. Verya Daeichin. They made the visits to Rotterdam possible, were contributing to this project with their enormous knowledge of ultrasound and made my time in Rotterdam fun and much valued.

I also would like to thank Prof. Gahr and his group, especially Lisa Trost, from the Max Planck Institute for Ornithology in Seewiesen, Germany, where the zebra finch experiments of this thesis were carried out. Additionally, I want to thank the people of the Neuroscience Department of Prof. de Zeeuw from the Erasmus MC, Rotterdam, Netherlands, namely Dr. Sebastiaan Koekkoek and Dr. Henk-Jan Boele, for the collaboration with mice studies in this thesis. Furthermore, my thanks go to Prof. Faber and co-workers from the University of Münster, who carried out the MRI measurements of the pigeon brain.

Finally, I want to massively thank my family for the continuous support and advise throughout my whole studies. To have such an amazing family is always heartwarming and makes me a very lucky and happy person. Last but not least, I would like speak out a huge thanks to my girlfriend Olga Schüle, who immensely supported me especially during the final phase of this PhD project.

# 8 APPENDIX

## 8.1 FUNCTIONAL ULTRASOUND OF THE RAT BRAIN

At an early stage of the project, the feasibility of HDfUS was evaluated with animals known for strong neurovascular responses[18], in this case rats. The left forelimb was stimulated for 10s with two needle electrodes (conductive cannulas) and different repetition frequencies and voltages. The study resulted in stimulus pattern dependent neuronal activations that demonstrate the potential of HDfUS to resolve these.

In Fig. 48a, the activity is found in the barrel cortex of the rat brain at bregma +0mm for different stimulation frequencies (2.5, 5 and 10Hz) at the left forepaw with 18V. The greyscale image shows the PD image, the colored overlay represents the area of activation with a correlation coefficient of $r > 0.2$ over five stimulations. The higher frequency stimulations project to larger activated areas in the rat brain.

In Fig. 48b, the response in the barrel cortex is shown when different voltages from 9V to 45V were applied at a 10Hz frequency. Interestingly, a voltage increase of the stimulation does not lead to enhanced brain activation after a certain threshold at ~27V. This indicates that the responses in the brain can be highly variant and the best set of parameters has to be finetuned. It furthermore demonstrates how HDfUS can assist in finding the best set of parameters and thus study the reasons of the different responses in vivo from a neurobiological point of view.

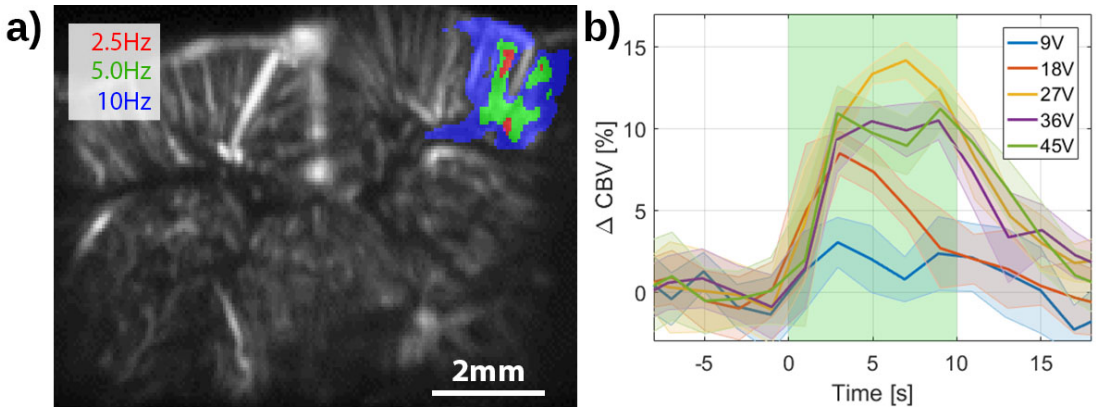


***Figure 48 | Left Forepaw Stimulation of the Rat***

***a)*** *PD image (grey) and activity map (colored overlay) in the barrel cortex of the rat brain for different stimulation frequencies.* ***b)*** *The temporal course of the hemodynamic response in the barrel cortex at different voltage levels (mean and standard deviation of two stimulations for each line).*

## 8.2 FUNCTIONAL ULTRASOUND COMBINED WITH MICE CONDITIONING

During this project, a collaboration with the Neuroscience Department of Prof. de Zeeuw from the Erasmus MC, Rotterdam, Netherlands, emerged, where the plasticity of cerebellar nuclei is studied with so-called eyeblink conditioning experiments on mice[88,89]. The underlying idea is to stimulate an awake mouse with a low intensity LED flash, followed 250ms later by an airpuff on the eye. The airpuff is an unpleasant stimulation for the mouse and causes an eyelid movement. In unconditioned mice, the LED flash does not cause any visible response in the animals, however with several training stimulations (typically several hundred) over a number of days, the mice are conditioned to close the eyes before the airpuff is set due to recognition of the LED flash.

To study the plasticity of the cerebellar nuclei, the neural activity is typically analyzed locally with electrophysiological recordings by placing an electrode at a defined spot in the brain. The eyelid movement is recorded by attaching a small magnet at the eyelid. Within this collaboration, the idea was to investigate the cerebellar nuclei by the means of HDfUS, which has the advantage of a large field of view compared to electrophysiological recordings.

In Fig. 49, the HDfUS results are shown for stimulations with airpuff and LED flash (Fig. 49b) as well as only LED (Fig. 49c). The strong correlation in the airpuff and LED case also corresponds to movement of the awake mouse, which sometimes occurred when the airpuff was set. For the LED only stimulation, there is only sometimes a response given (see also error bar and smaller average eyeblink response in the bottom of Fig. 49c). To evaluate the brain activity in case of an actual eyeblink response vs. no eyeblink response, the datasets are furthermore separated. For the no eyeblink case, a neural response is lacking (Fig. 49d) and a brain activity is only observed when there is an eyelid movement. This is further studied by plotting the neural activity amplitude (i.e. correlation coefficient) against the amount of eyelid movement in three ROIs (Fig. 50). Two ROIs (green and blue in Fig. 50) are within the nuclei that were determined to be responsive (see from Fig. 49c) and one control ROI (black in Fig. 50) within an irresponsive area. The corresponding linear fits in Fig. 50b clearly show that a stronger eyeblink response is associated with an amplified brain activity in the responsive nuclei. The control ROI does not exhibit this characteristic.

This shows that HDfUS is in principle capable of studying the plasticity of small cerebellar nuclei at a defined detail. The method also allows to investigate how neural processes correlate to sensory output at a large imaging field of view. To draw more conclusions about this, larger datasets would be necessary, which is planned for future work.

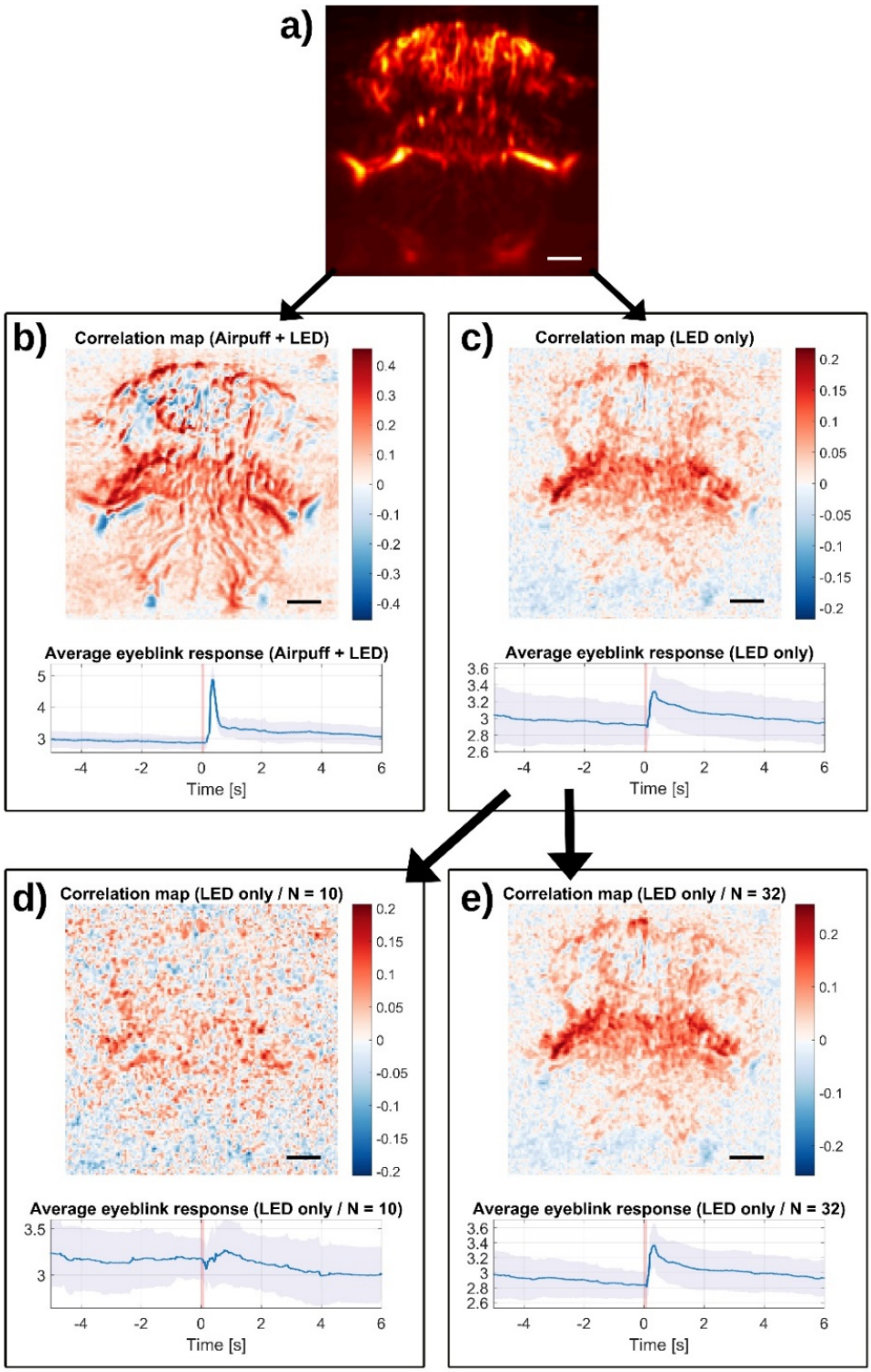


***Figure 49 | HDfUS with Eyeblink Conditioning in Mice***

***a)*** *Vascularity from PD Image.* ***b-e)*** *Correlation maps with a three second hemodynamic response (color represents $r$-values in different ranges). The correlation maps represent the brain activity to the stimulations with airpuff and LED (**b**) and LED only (**c**), each at 50 stimulations. The corresponding average eyeblink response is shown below (with standard deviation as error bar). The dataset from the LED only stimulation is further separated into **d**) eyeblink irresponsive (N=10) and **e**) eyeblink responsive (N=32). The eight left stimulations were excluded due to movement. The scalebar is 1mm in all figures. Data was obtained at the Neuroscience department of Prof. de Zeeuw from the Erasmus MC, Rotterdam.*

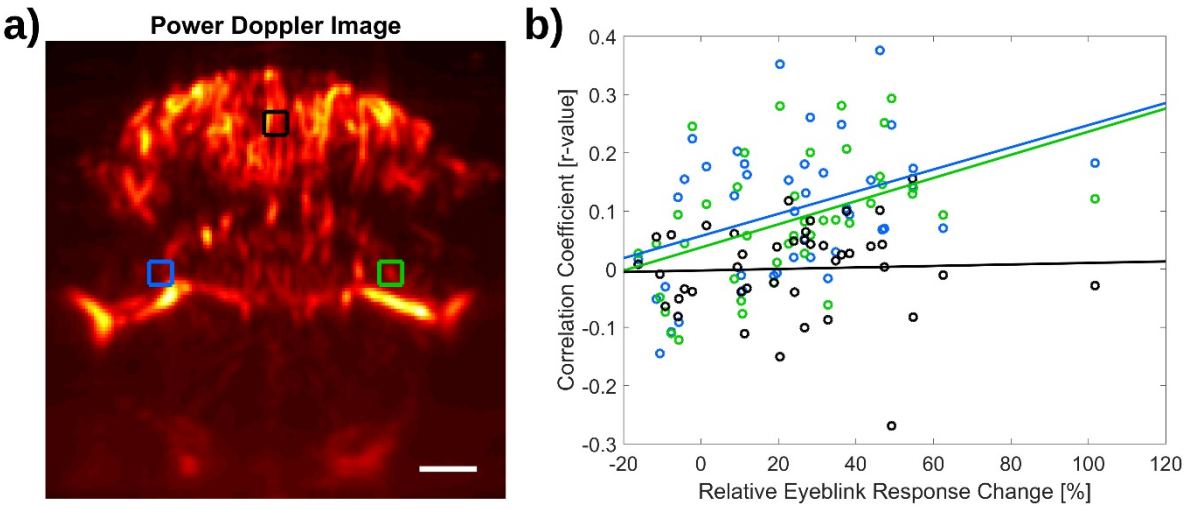


***Figure 50 | Correlation Coefficient from PD imaging vs. Eyeblink Response***

***a**) PD image with ROIs within the cerebellar nuclei and a scalebar of 1mm. **b**) $r$-values (≈ 'nerual activity amplitude') from the color matching ROIs vs. relative eyeblink response change shows that the activity measured by HDfUS is proportional to the amount of eyelid movement. Solid lines represent the linear fit. Data was obtained at the Neuroscience department of Prof. de Zeeuw from the Erasmus MC, Rotterdam.*

## 8.3 FUNCTIONAL ULTRASOUND TO STUDY BRAIN CONNECTIVITY IN MICE

A case where the excellent spatiotemporal resolution of HDfUS can be thoroughly exploited could be demonstrated in another pilot study at the Neuroscience Department of Chris de Zeeuw from the Erasmus MC, Rotterdam, Netherlands. The idea here was to place an electrode, which is typically used for electrophysiological recordings, at a certain nucleus in the brain and record the evolution of the neural activity in the brain, revealing unknown connectivities. This is shown in Fig. 51b, where the activity of neural substrates is shown at different times after stimulation. Fig. 51a shows the placement of the electrode in the brain, which is also the spot exhibiting enhanced activity at $t$ = 0.8s. Interestingly, deeper regions and locally not connected regions also response shortly after the stimulation ($t = 1.8s$), followed by a widespread activation within the cerebellum and deeper brain structures below the cortex.

The potential of this study is enormous, as it can lead to temporally resolved investigation of brain connectivities in vivo. Typically, the pathway structure in the brain is obtained by staining and histology, which requires the sacrifice of the animal and cannot resolve temporal dynamics. fMRI does not offer a sufficient spatiotemporal resolution to study such dynamics and electrophysiological recordings cannot image a large field of view. Thus, HDfUS has the potential to lead to a number of new insights about the brain connectivity.

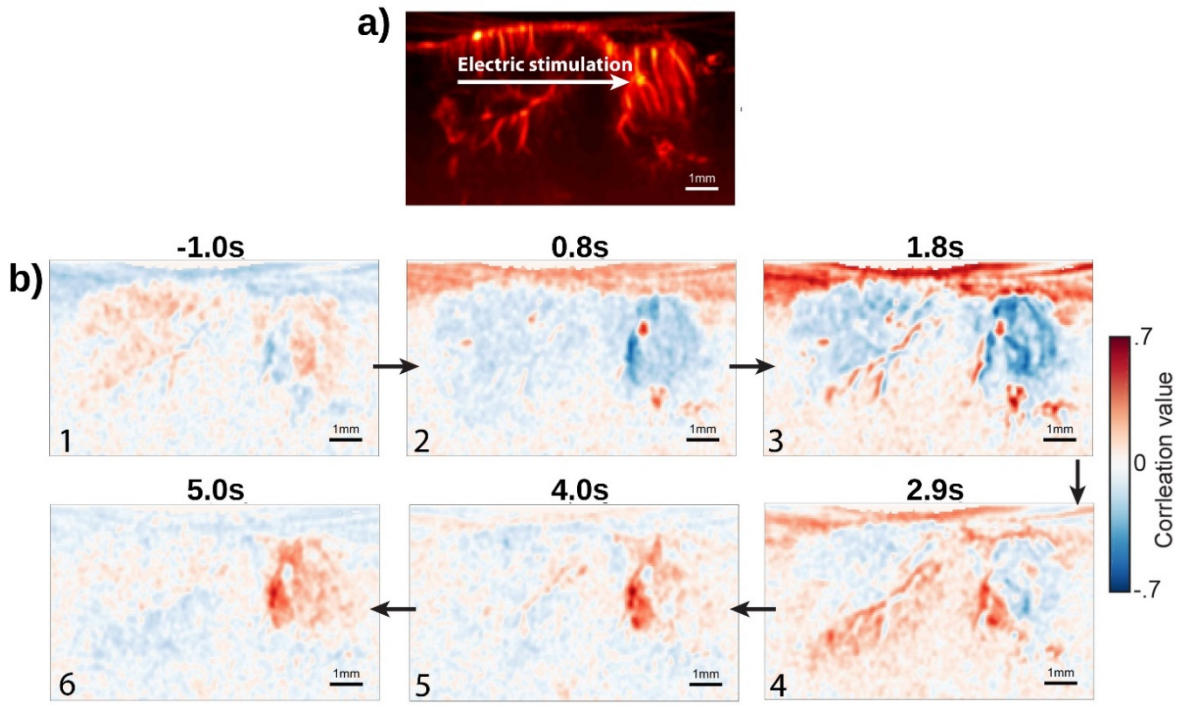


***Figure 51 | Neurovascular Coupling Reveals Brain Connectivity in Mice***

***a)*** *PD image obtained from an awake mouse. The brain slice is in this case 90 degree shifted to image the cortical and cerebellar structures at the same time. The arrow indicates the point where the current is injected.* ***b)*** *A series of subsequent correlation images obtained by correlating every pixel over time with the known stimulation signal. The lag-time of the correlation signal is used to extract information on the temporal response of the brain to the electric stimulation. Data was obtained at the Neuroscience department of Prof. de Zeeuw from the Erasmus MC, Rotterdam.*

## 8.4 VELOCITY VECTOR ESTIMATION USING A DUAL TRANSDUCER SETUP

At the beginning of my PhD, I spent for about three months at a leading ultrasound research group at the Thorax Center, Erasmus MC, Rotterdam, Netherlands, to gain a deeper knowledge on the current state of research in the ultrasound community. Along with the productive collaboration throughout this whole project, the utilization of two 128 element transducers with the Verasonics Vantage 256 channel System was investigated within these three months stay. For fUS studies, such a dual transducer system could in principle image simultaneously different brain regions that are not within one plane or the same region could be imaged to get a better SNR and sensitivity due to the differently angled beams out of plane velocity components. At the state of studying this issue, the fUS setup was however not established and the dual transducer system was realized in the scope of carotid artery imaging with the group at the Thorax Center. The following discussion is based on the proceeding[90] that emerged from this side project.

Carotid arteries supply the brain with oxygenated blood. When these arteries are affected by atherosclerosis, which causes plaques to grow inside the artery wall, the blood flow may be compromised. When these plaques cause narrowing of the lumen, the peak systolic velocity of the blood flow in this stenotic region will change. The measure of this velocity seems to be an important indication in the clinical evaluation of carotid stenosis[91]. The blood flow velocity inside the carotid artery can be measured noninvasively using ultrasound Doppler. In the recent years, progress has been made to further increase the reproducibility and sensitivity of ultrasound Doppler. A major improvement in terms of sensitivity has been accomplished by the application of high frame rate imaging (cf. section 2.2).

Despite the success of ultrasound Doppler as a major clinical tool, the difficulty of measuring true user-independent blood flow velocities is still an unresolved problem. This problem is mainly due to the fact that Doppler signals are normally acquired within a 2D imaging plane whereas the flow velocity vector is intrinsically 3D. The third component of the flow velocity vector that cannot be measured directly, named the out-of-plane motion, contaminates the velocity estimation in the 2D plane. This especially happens around large stenotic lesions and around the bifurcation in the carotid artery where the flow can be very complex.

Possibly the best method for measuring the full 3D velocity field is using a 2D array which would enable full 3D high frame rate imaging[75]. However, these arrays are not abundantly available, especially not for carotid imaging, and the scanners that could deal with these high volume rates are also not yet available for clinical use. One of the best attempts proposed to address the out-of-plane motion problem using conventional linear arrays is the technique of intrinsic spectral broadening[94–96]. The main principle underlying this technique is the correction of the received Doppler spectrum (shape) with an estimated or predicted spectrum. The reasoning here is that out-of-plane motion causes the spectrum to broaden with respect to the predicted spectrum. Obviously this technique relies strongly on the characterization of the estimated spectrum. When, for instance, the flow becomes complex and cannot be modelled a priori, these methods fail.

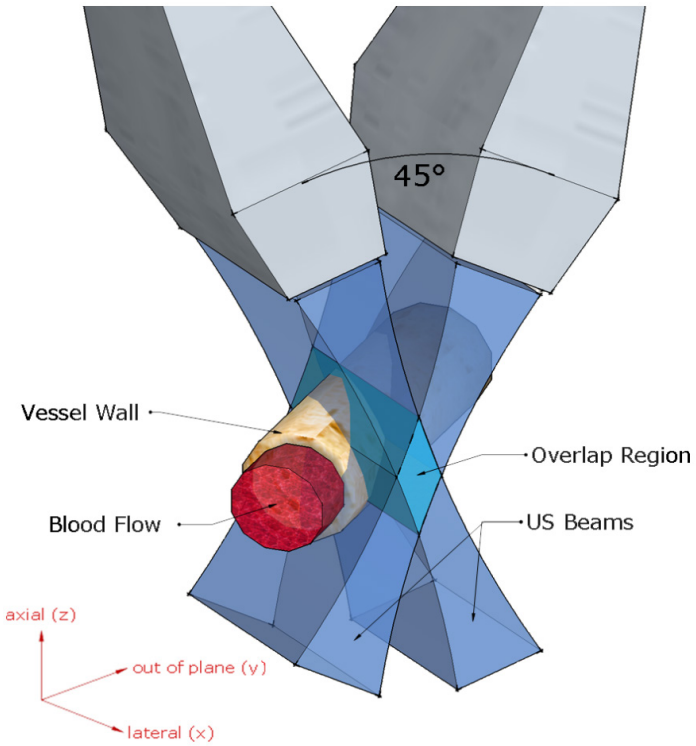


***Figure 52 | Schematic of the Dual Transducer Setup***
*Experimental setup with two transducers scanning the carotid artery at an angle arrangement of 45◦. The overlap of two plane wave emissions (transparent blue) is shown to be in the region of the carotid artery. Image created with SketchUp Make.*

Here, a new and robust method for deriving the 3D velocity vector field is explored using two conventional linear arrays that are connected to a commercially available ultrasound machine. The two arrays are joined in such a manner that the imaging planes intersect under a 45 degree angle inside the carotid artery lumen.

For each imaging plane, a 2D velocity vector field is obtained using tilted plane-wave transmissions and conventional triangulation of the received Doppler signals[93]. The two, 2D velocity vector fields are then combined to obtain the 3D velocity vector field using again triangulation between the different angled observations. Figure 52 shows a schematic representation of the proposed dual-transducer Doppler method.

To show the proof of concept of this dual-transducer method, two relatively low-frequency linear array transducers are used (5MHz, ATL L7-4, Philips, MA, USA). A custom made holder kept the transducers at a 45 degree angle. The transducers are connected to a commercial ultrasound research system (Verasonics Vantage 256). The Verasonics system has two active connectors and allows two transducers to be connected and accessed at the same time. The interleaved Doppler acquisitions for both transducers involve an ensemble length of 150, three angled plane-wave beams (-7, 0, + 7 degree) and a Doppler pulse repetition rate of 2.5kHz at a 5MHz transmission frequency (2.5 cycle Gaussian modulated). After clutter rejection the velocity signal is derived for the three angled beams of each transducer with the first lag autocorrelation. The lateral and axial flow components are derived by triangulation as described in [93].

Using the dual-transducer method, an additional triangulation step for the out-of-plane axis can be performed in the overlap region. The overlap region (light-blue region in Fig. 52) can be

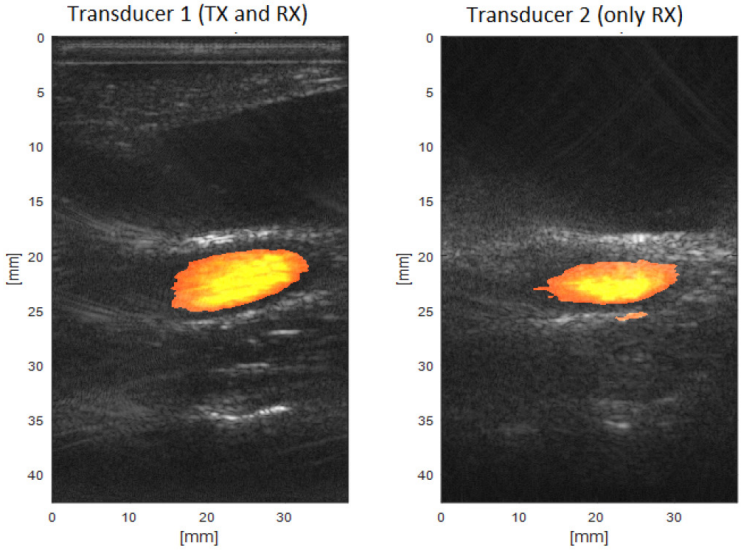


***Figure 53 | Two Images from the Dual Transducer Setup*** *Combined greyscale and Doppler images showing the received (RX) PD signal of both transducers when only one transducer is transmitting (TX).*

confirmed by measuring the Doppler signal of the carotid artery, using one transducer in transmit and both in receive mode.

If the blood flow in the lumen is imaged well for both transducers, it is justified to triangulate the signal along the out-of-plane axis, given that a homogeneous flow profile is abundant. This is verified in Fig. 53, where it can be seen that the spatial dimensions and magnitude of the measured PD signal are the same for both transducers. If – for the non-transmitting transducer – only a limited region within the carotid artery results in Doppler signal, the data can only be triangulated in this limited region. As the Doppler signal in Fig. 53 shows the same lumen sizing for both transducers, the out-of-plane triangulation is justified within the whole lumen.

In order to quantify the 3D blood flow velocities with lateral (x), out-of-plane ($y$) and axial ($z$) components it can be derived that

$$v_{n,m}^{(x)} = \frac{c}{8 f_0 \sin(\theta_{n,m})} \left[ (\hat{f}_n^{(1)} - \hat{f}_m^{(1)}) + (\hat{f}_n^{(2)} - \hat{f}_m^{(2)}) \right] \quad (33)$$

$$v_{n,m}^{(y)} = \frac{c}{8 f_0 \cos(\theta_{n,m}) \sin(\phi)} \left[ (\hat{f}_n^{(1)} + \hat{f}_m^{(1)}) + (\hat{f}_n^{(2)} + \hat{f}_m^{(2)}) \right] \quad (34)$$

$$v_{n,m}^{(z)} = \frac{c}{8 f_0 \cos(\theta_{n,m}) \cos(\phi)} \left[ (\hat{f}_n^{(1)} + \hat{f}_m^{(1)}) + (\hat{f}_n^{(2)} + \hat{f}_m^{(2)}) \right] \quad (35)$$

where $f_0$ is the center frequency of the transmitted pulse and $\hat{f}_{n,m}^{i}$ is the Doppler shifted frequency of transducer $i$ with $n$ or $m$ being the corresponding angled plane-wave transmission of each transducer. $\phi = 22.5°$ is the half angle opening of the angled transducer setup and $\theta_{n,m} = (\theta_n - \theta_m)/2$ the half angle opening of two triangulated angled beams for each transducer with $n \neq m$. The overall velocity is then averaged over all calculations to

$$v^{(i)} = \frac{2}{N_a(N_a - 1)} \sum_{1 \leq n < m \leq N_a} v_{n,m}^{(i)} \quad (36)$$

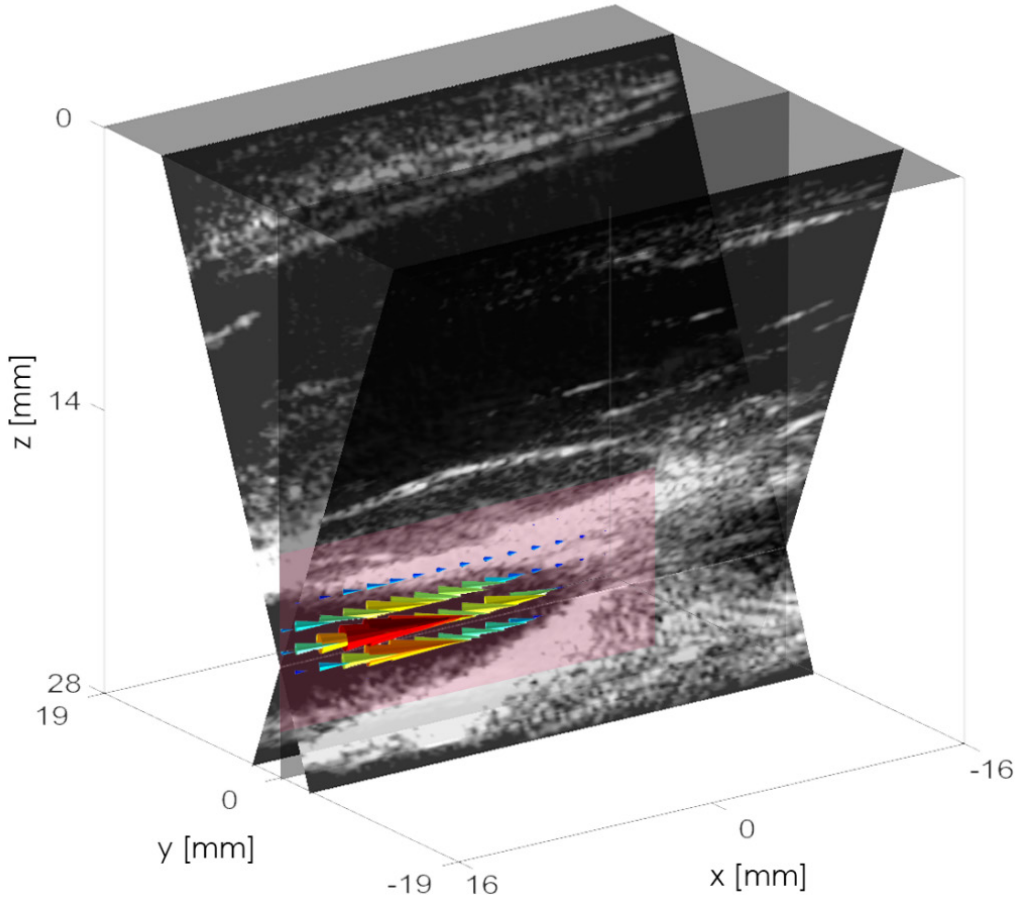


***Figure 54 | 3D Velocity Vector Measurement***

*B-mode images of the two transducers, superimposed by the 3D velocity vector cones in the beam overlap region (purple overlay). The cone colors indicate the magnitude of the velocity component.*

for all components $i = [x, y, z]$ with $N_a = 3$ being the number of angled beams for each transducer.

The results of the dual-transducer velocity estimation setup for a carotid artery measurement are shown in Fig. 54 and Fig. 55. The B-Mode images of the two transducers as well as the overlaid velocity vectors in three dimensions are depicted in Fig. 54. The region of interest is marked purple in the image and shown in detailed 2D color Doppler maps in Fig. 55 for all separate velocity components. The velocity in the lumen center is estimated to be v = (−31±1, 725±34, −299±8)mm/s in axial, lateral and out-of-plane direction, respectively. The uncertainty is derived by the 2D standard deviation of the 75 pixels in the lumen center, which resembles an approximate area of (1.5mm)². These values yield an RMS absolute flow velocity of 785 ± 53mm/s, which is mainly oriented in the lateral (x) direction.

Thus, the determination of blood flow velocities in all three dimensions with a simple setup of two transducers is possible. Compared to other recent 3D vector flow measurement techniques, which require complicated matrix array transducers, this method can be

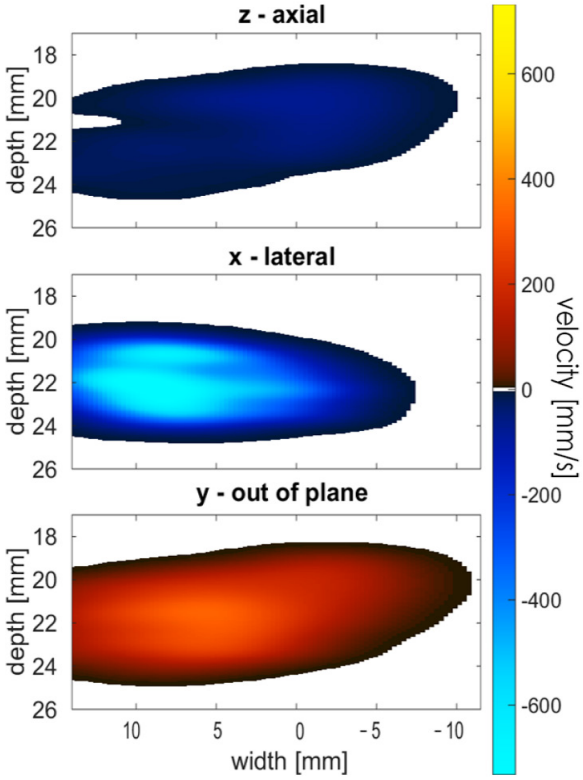


***Figure 55 | The Three separate Components of the 3D Velocity Vector***
*Velocity maps of the three separate components in the overlap region (marked in purple in Fig. 54).*

accomplished with only two conventional linear array transducers and still results in robust data for in vivo measurements.

One limitation of this technique is that the imaging area is restricted by the overlap of the fixed foci of the two transducers. This results in two problems: A limited depth range and a finite sizing of the sample volume. The limitation of depth range can be overcome dynamically for example by wobbling one transducer and thereby moving the sample volume in depth along the other transducer beam or statically by decreasing the separation distance as well as the angle $\phi$ between the two transducers. The latter solution would stretch the sample volume in axial direction, however with the drawback that the out-of-plane triangulation becomes more error prone, because of the inverse proportionality of $\sin\phi$ in the out-of-plane velocity estimation (see equation (34)).

For the proposed dual-transducer setup, homogeneous flow inside the overlap region is assumed in order to justify the triangulation of the two transducer beams. This assumption can be challenged in real-life situations. Further study needs to be carried out to see whether the straightforward triangulation can be adapted to account for inhomogeneous flow inside the overlap region. One such advancement could be to correct the received spectrum as proposed in the spectral broadening correction techniques[95,96]. The benefit of having two identical transducers sampling the same volume under different angles may just provide the information needed to lead to a unique solution to correct for the spectral broadening.

In conclusion of this study, proof is provided that 3D flow fields with realistic flow velocities inside the CA can be measured in-vivo using a simple setup of two conventional linear array transducers. With respect to fUS acquisitions, the system would need to be adapted for higher

frequency transducers and the processing algorithms would need to be optimized. Focusing on parallel processing of two GPUs to cope with the doubled datastream would be a first approach to implement such a setup.

## 8.5 SETTINGS FOR THE HDFUS EXPERIMENTS

The HDfUS acquisition algorithms were under constant development and different parameter settings were used for the various experiments. To facilitate reproducibility of the results, the settings for all the discussed HDfUS studies in this thesis are listed in the following table. The structure is based on the explanation of the different acquisition parameters in section 3.2.3.

| | Parameter | Rat<br>Rats vs. Pigeons (4.1.2 & 8.1) | Pigeon<br>Rats vs. Pigeons (4.1.2) | Pigeon<br>Static Light Source (4.2.1) | Pigeon<br>Moving Light Source (4.2.2) | Pigeon<br>Auditory Stimulation (4.3.1) | Zebra Finch<br>Auditory Stimulation (4.3.2) | Pigeons<br>Magnetic Field (4.4) | Mice<br>Conditioning (8.1) |
|---|---|---|---|---|---|---|---|---|---|
| Plane Wave Frame | Transmit Frequency $f_0$ | 15.6MHz | 15.6MHz | 15.6MHz | 15.6MHz | 15.6MHz | 15.6MHz | 15.6MHz | 15.6MHz |
| | Pulse Length | 2.5 | 2.5 | 2.5 | 2.5 | 2.5 | 2.5 | 2.5 | 2.5 |
| | Transmit Voltage | 14.0V | 15.0V | 15.0V | 15.0V | 15.0V | 15.0V | 15.0V | 9.7V |
| | Aperture Apodization | $12.8mm$ | $12.8mm$ | $12.8mm$ | $12.8mm$ | $12.8mm$ | $\sim 9mm$ | $12.8mm$ | $\sim 9mm$ |
| | Range of Depth in Samples $N_s$ | 640 | 640 | 640 | 640 | 640 | 640 | 640 | 640 |
| Compounded Frame | Number of Angled Beams $N_a$ | 36 | 36 | 36 | 20 | 20 | 20 | 20 | 20 |
| | Angle Opening | 16° | 16° | 16° | 16° | 16° | 16° | 16° | 16° |
| PD Image | Doppler PRF $f_{PRF}$ | $350Hz$ | $300Hz$ | $300Hz$ | $1000Hz$ | $1000Hz$ | $1000Hz$ | $1000Hz$ | $1000Hz$ |
| | Acquisition Time per PD image | $400ms$ | $533ms$ | $533ms$ | $300ms$ | $300ms$ | $300ms$ | $300ms$ | $200ms$ |
| | Ensemble Length $N_e$ | 140 | 160 | 160 | 300 | 300 | 300 | 300 | 200 |
| | SVD Parameters | [56 115] | [54 131] | [54 131] | [120 246] | [120 246] | [120 246] | [120 246] | [80 164] |
| Stimulation Sequence | Stimulation Type | Tactile (forepaw) | Visual (static) | Visual (static) | Visual (dynamic) | Hawk sound | Partner song | Different magnetic | Visual & tactile |
| | Number of Stimulations | 12 | 8 | $4-5$ | 2 | 1 | 6 | 30 | 50 |
| | Stimulation Time | $10s$ | $15s$ | $15s$ | $15s$ | $15s$ | $8s$ | $5s$ | $< 1s$ |
| Software | Version | MATLAB-GPU | MATLAB-GPU | MATLAB-GPU | C++/CUDA | C++/CUDA | C++/CUDA | C++/CUDA | C++/CUDA |

# 9 NOMENCLATURE

| | |
|---|---|
| BF | beamformed |
| BOLD | blood oxygenation level dependent |
| CBV | cerebral blood volume |
| CNR | contrast-to-noise ratio |
| CPU | central processing unit |
| DWS | diffusing wave spectroscopy |
| fMRI | functional magnetic resonance imaging |
| fUS | functional ultrasound |
| GPU | graphics processing unit |
| HDfUS | high definition functional ultrasound |
| MRI | magnetic resonance imaging |
| PD | power Doppler |
| PRF | pulse repetition frequency |
| PW | plane wave |
| RA | robust nucleus of the arcopallium |
| RMS | root mean square |
| ROI | region of interest |
| Rt | nucleus rotundus |
| SNR | signal-to-noise ratio |
| SSD | solid-state-drive |
| SVD | singular value decomposition |
| TO | optical tectum |

# 10 LIST OF FIGURES

# 11 BIBLIOGRAPHY


[1] T. L. Szabo, *Diagnostic Ultrasound Imaging: Inside Out*. Academic Press, 2013.

[2] K. T. Dussik, "Über die Möglichkeit, hochfrequente mechanische Schwingungen als diagnostisches Hilfsmittel zu verwerten," *Z. Für Gesamte Neurol. Psychiatr.*, vol. 174, no. 1, pp. 153–168, Dec. 1942.

[3] J. J. Wild, "The use of ultrasonic pulses for the measurement of biologic tissues and the detection of tissue density changes," *Surgery*, vol. 27, no. 2, pp. 183–188, Feb. 1950.

[4] D. H. Howry and W. R. Bliss, "Ultrasonic visualization of soft tissue structures of the body," *J. Lab. Clin. Med.*, vol. 40, no. 4, pp. 579–592, Oct. 1952.

[5] J. A. Jensen, *Estimation of Blood Velocities Using Ultrasound: A Signal Processing Approach*. Cambridge University Press, 1996.

[6] S. Satomura, "Ultrasonic Doppler Method for the Inspection of Cardiac Functions," *J. Acoust. Soc. Am.*, vol. 29, no. 11, pp. 1181–1185, Nov. 1957.

[7] D. W. Baker, "Pulsed Ultrasonic Doppler Blood-Flow Sensing," *IEEE Trans. Sonics Ultrason.*, vol. 17, no. 3, pp. 170–184, Jul. 1970.

[8] M. Brandestini, "Topoflow - A digital full range Doppler velocity meter," *IEEE Trans. Sonics Ultrason.*, vol. 25, no. 5, pp. 287–292, Sep. 1978.

[9] J. Bercoff, "Ultrafast Ultrasound Imaging," in *Ultrasound Imaging - Medical Applications*, InTech, 2011.

[10] G. Montaldo, M. Tanter, J. Bercoff, N. Benech, and M. Fink, "Coherent plane-wave compounding for very high frame rate ultrasonography and transient elastography," *IEEE Trans. Ultrason. Ferroelectr. Freq. Control*, vol. 56, no. 3, pp. 489–506, Mar. 2009.

[11] E. Macé, G. Montaldo, B. F. Osmanski, I. Cohen, M. Fink, and M. Tanter, "Functional ultrasound imaging of the brain: theory and basic principles," *IEEE Trans. Ultrason. Ferroelectr. Freq. Control*, vol. 60, no. 3, pp. 492–506, Mar. 2013.

[12] E. Macé, G. Montaldo, I. Cohen, M. Baulac, M. Fink, and M. Tanter, "Functional ultrasound imaging of the brain," *Nat. Methods*, vol. 8, no. 8, pp. 662–664, Aug. 2011.

[13] X. Yang, F. Hyder, and R. G. Shulman, “Activation of single whisker barrel in rat brain localized by functional magnetic resonance imaging,” *Proc. Natl. Acad. Sci.*, vol. 93, no. 1, pp. 475–478, Jan. 1996.

[14] J. Goense, Y. Bohraus, and N. K. Logothetis, “fMRI at High Spatial Resolution: Implications for BOLD-Models,” *Front. Comput. Neurosci.*, vol. 10, 2016.

[15] G. H. Glover, “Overview of Functional Magnetic Resonance Imaging,” *Neurosurg. Clin. N. Am.*, vol. 22, no. 2, pp. 133–139, Apr. 2011.

[16] N. K. Logothetis, “What we can do and what we cannot do with fMRI,” *Nature*, vol. 453, no. 7197, pp. 869–878, Jun. 2008.

[17] B.-F. Osmanski, S. Pezet, A. Ricobaraza, Z. Lenkei, and M. Tanter, “Functional ultrasound imaging of intrinsic connectivity in the living rat brain with high spatiotemporal resolution,” *Nat. Commun.*, vol. 5, p. 5023, Oct. 2014.

[18] A. Urban, E. Mace, C. Brunner, M. Heidmann, J. Rossier, and G. Montaldo, “Chronic assessment of cerebral hemodynamics during rat forepaw electrical stimulation using functional ultrasound imaging,” *NeuroImage*, vol. 101, pp. 138–149, Nov. 2014.

[19] A. Urban, C. Dussaux, G. Martel, C. Brunner, E. Mace, and G. Montaldo, “Real-time imaging of brain activity in freely moving rats using functional ultrasound,” *Nat. Methods*, vol. 12, no. 9, pp. 873–878, Sep. 2015.

[20] C. Errico, B.-F. Osmanski, S. Pezet, O. Couture, Z. Lenkei, and M. Tanter, “Transcranial functional ultrasound imaging of the brain using microbubble-enhanced ultrasensitive Doppler,” *NeuroImage*, vol. 124, Part A, pp. 752–761, Jan. 2016.

[21] E. Tiran *et al.*, “Transcranial Functional Ultrasound Imaging in Freely Moving Awake Mice and Anesthetized Young Rats without Contrast Agent,” *Ultrasound Med. Biol.*, May 2017.

[22] M. Gesnik *et al.*, “3D Functional Ultrasound Imaging of the cerebral visual system in rodents,” *NeuroImage*, Apr. 2017.

[23] B. F. Osmanski *et al.*, “Functional ultrasound imaging reveals different odor-evoked patterns of vascular activity in the main olfactory bulb and the anterior piriform cortex,” *NeuroImage*, vol. 95, pp. 176–184, Jul. 2014.

[24] R. L. Rungta, B.-F. Osmanski, D. Boido, M. Tanter, and S. Charpak, “Light controls cerebral blood flow in naive animals,” *Nat. Commun.*, vol. 8, p. 14191, Jan. 2017.

[25] L.-A. Sieu *et al.*, “EEG and functional ultrasound imaging in mobile rats,” *Nat. Methods*, vol. 12, no. 9, pp. 831–834, Sep. 2015.

[26] C. Demene *et al.*, “Functional ultrasound imaging of brain activity in human newborns,” *Sci. Transl. Med.*, vol. 9, no. 411, p. eaah6756, Oct. 2017.

[27] E. D. Jarvis, “Learned Birdsong and the Neurobiology of Human Language,” *Ann. N. Y. Acad. Sci.*, vol. 1016, pp. 749–777, Jun. 2004.

[28] L. Van Ruijssevelt, A. Van der Kant, G. De Groof, and A. Van der Linden, “Current state-of-the-art of auditory functional MRI (fMRI) on zebra finches: Technique and scientific achievements,” *J. Physiol.-Paris*, vol. 107, no. 3, pp. 156–169, Jun. 2013.

[29] H. U. Voss *et al.*, “Functional MRI of the zebra finch brain during song stimulation suggests a lateralized response topography,” *Proc. Natl. Acad. Sci.*, vol. 104, no. 25, pp. 10667–10672, Jun. 2007.

[30] M. Manns and J. Römling, “The impact of asymmetrical light input on cerebral hemispheric specialization and interhemispheric cooperation,” *Nat. Commun.*, vol. 3, p. 696, Feb. 2012.

[31] O. Güntürkün *et al.*, “Asymmetry pays: visual lateralization improves discrimination success in pigeons,” *Curr. Biol.*, vol. 10, no. 17, pp. 1079–1081, Sep. 2000.

[32] T. Ritz, S. Adem, and K. Schulten, “A Model for Photoreceptor-Based Magnetoreception in Birds,” *Biophys. J.*, vol. 78, no. 2, pp. 707–718, Feb. 2000.

[33] W. Wiltschko and R. Wiltschko, “Magnetic orientation and magnetoreception in birds and other animals,” *J. Comp. Physiol. A*, vol. 191, no. 8, pp. 675–693, Aug. 2005.

[34] “The Neural Basis of Long-Distance Navigation in Birds,” *Annu. Rev. Physiol.*, vol. 78, no. 1, pp. 133–154, 2016.

[35] C. Martin, “Contributions and complexities from the use of in vivo animal models to improve understanding of human neuroimaging signals,” *Front. Neurosci.*, vol. 8, Aug. 2014.

[36] K. Masamoto and I. Kanno, “Anesthesia and the Quantitative Evaluation of Neurovascular Coupling,” *J. Cereb. Blood Flow Metab.*, vol. 32, no. 7, pp. 1233–1247, Jul. 2012.

[37] C. Martin, Y. Zheng, N. R. Sibson, J. E. W. Mayhew, and J. Berwick, “Complex spatiotemporal haemodynamic response following sensory stimulation in the awake rat,” *Neuroimage*, vol. 66, pp. 1–8, Feb. 2013.

[38] K. L. Moore, A. F. Dalley, and A. M. R. Agur, *Clinically Oriented Anatomy*. Lippincott Williams & Wilkins, 2013.

[39] L. Z. Garamszegi, A. P. Møller, and J. Erritzøe, “Coevolving avian eye size and brain size in relation to prey capture and nocturnality,” *Proc. Biol. Sci.*, vol. 269, no. 1494, pp. 961–967, May 2002.

[40] D. M. Kelly, W. F. Bischof, D. R. Wong-Wylie, and M. L. Spetch, “Detection of Glass Patterns by Pigeons and Humans: Implications for Differences in Higher-Level Processing,” *Psychol. Sci.*, vol. 12, no. 4, pp. 338–342, Jul. 2001.

[41] S. Watanabe and N. F. Troje, “Towards a ‘virtual pigeon’: A new technique for investigating avian social perception,” *Anim. Cogn.*, vol. 9, no. 4, pp. 271–279, Oct. 2006.

[42] H. Sun and B. J. Frost, “Computation of different optical variables of looming objects in pigeon nucleus rotundus neurons,” *Nat. Neurosci.*, vol. 1, no. 4, pp. 296–303, Aug. 1998.

[43] B. J. Frost, D. R. Wylie, and Y. C. Wang, “The Analysis of Motion in the Visual Systems of Birds,” in *Perception and Motor Control in Birds*, Springer, Berlin, Heidelberg, 1994, pp. 248–269.

[44] A. G. Palacios and F. J. Varela, “Color mixing in the pigeon (Columba livia) II: A psychophysical determination in the middle, short and near-UV wavelength range,” *Vision Res.*, vol. 32, no. 10, pp. 1947–1953, Oct. 1992.

[45] M. Remy and J. Emmerton, “Behavioral spectral sensitivities of different retinal areas in pigeons,” *Behav. Neurosci.*, vol. 103, no. 1, pp. 170–177, Feb. 1989.

[46] J. J. Vos Hzn, M. A. J. M. Coemans, and J. F. W. Nuboer, “The photopic sensitivity of the yellow field of the pigeon’s retina to ultraviolet light,” *Vision Res.*, vol. 34, no. 11, pp. 1419–1425, Jun. 1994.

[47] S. A. McFadden and J. M. Wild, “Binocular Depth Perception in the Pigeon,” *J. Exp. Anal. Behav.*, vol. 45, no. 2, pp. 149–160, Mar. 1986.

[48] D. R. W. Wylie, C. Gutierrez-Ibanez, J. M. P. Pakan, and A. N. Iwaniuk, “The optic tectum of birds: mapping our way to understanding visual processing,” *Can. J. Exp. Psychol. Rev. Can. Psychol. Exp.*, vol. 63, no. 4, pp. 328–338, Dec. 2009.

[49] N. Freund, C. E. Valencia-Alfonso, J. Kirsch, K. Brodmann, M. Manns, and O. Güntürkün, “Asymmetric top-down modulation of ascending visual pathways in pigeons,” *Neuropsychologia*, vol. 83, pp. 37–47, Mar. 2016.

[50] P. D. Sturkie, *Avian Physiology*. Springer Science & Business Media, 2012.

[51] H.-O. Nalbach, F. Wolf-Oberhollenzer, and K. Kirschfeld, “The pigeon’s eye viewed through an ophthalmoscopic microscope: Orientation of retinal landmarks and significance of eye movements,” *Vision Res.*, vol. 30, no. 4, pp. 529–540, Jan. 1990.

[52] B. S. W. Ng, A. Grabska-Barwińska, O. Güntürkün, and D. Jancke, “Dominant vertical orientation processing without clustered maps: early visual brain dynamics imaged with voltage-sensitive dye in the pigeon visual Wulst,” *J. Neurosci. Off. J. Soc. Neurosci.*, vol. 30, no. 19, pp. 6713–6725, May 2010.

[53] M. Manns and F. Stroeckens, “Functional and structural comparison of visual lateralization in birds - similar but still different,” *Front. Psychol.*, vol. 5, Mar. 2014.

[54] N. Freund, C. E. Valencia-Alfonso, J. Kirsch, K. Brodmann, M. Manns, and O. Güntürkün, “Asymmetric top-down modulation of ascending visual pathways in pigeons,” *Neuropsychologia*, vol. 83, pp. 37–47, März 2016.

[55] J. J. Bolhuis and M. Gahr, “Neural mechanisms of birdsong memory,” *Nat. Rev. Neurosci.*, vol. 7, no. 5, pp. 347–357, May 2006.

[56] Y. Wang, A. Brzozowska-Prechtl, and H. J. Karten, “Laminar and columnar auditory cortex in avian brain,” *Proc. Natl. Acad. Sci.*, vol. 107, no. 28, pp. 12676–12681, Jul. 2010.

[57] R. Wiltschko and W. Wiltschko, “The magnetite-based receptors in the beak of birds and their role in avian navigation,” *J. Comp. Physiol. A*, vol. 199, no. 2, pp. 89–98, Feb. 2013.

[58] L.-Q. Wu and J. D. Dickman, “Neural Correlates of a Magnetic Sense,” *Science*, vol. 336, no. 6084, pp. 1054–1057, May 2012.

[59] M. Belau, “Magnetoreception,” Universität Konstanz, 2015.

[60] W. Scheffer, “Novel functional techniques to investigate magnetoreception in pigeons,” Universität Konstanz, 2016.

[61] J. Bercoff *et al.*, “Ultrafast compound doppler imaging: providing full blood flow characterization,” *IEEE Trans. Ultrason. Ferroelectr. Freq. Control*, vol. 58, no. 1, pp. 134–147, Jan. 2011.

[62] M. Tanter and M. Fink, “Ultrafast imaging in biomedical ultrasound,” *IEEE Trans. Ultrason. Ferroelectr. Freq. Control*, vol. 61, no. 1, pp. 102–119, Jan. 2014.

[63] B. Angelsen, *Ultrasound imaging: waves, signals, and signal processing*. Trondhejm, Norway: Emantec, 2000.

[64] N. M. Tole and H. Ostensen, *Basic Physics of Ultrasonographic Imaging*. World Health Organization, 2005.

[65] J.-Y. Lu, “2D and 3D high frame rate imaging with limited diffraction beams,” *IEEE Trans. Ultrason. Ferroelectr. Freq. Control*, vol. 44, no. 4, pp. 839–856, Jul. 1997.

[66] J. Cheng and J. Lu, “Extended high-frame rate imaging method with limited-diffraction beams,” *IEEE Trans. Ultrason. Ferroelectr. Freq. Control*, vol. 53, no. 5, pp. 880–899, May 2006.

[67] P. Kruizinga, F. Mastik, N. de Jong, A. F. W. van der Steen, and G. van Soest, “Plane-wave ultrasound beamforming using a nonuniform fast fourier transform,” *IEEE Trans. Ultrason. Ferroelectr. Freq. Control*, vol. 59, no. 12, Dezember 2012.

[68] J. A. Jensen, “An Analysis of Pulsed Wave Ultrasound Systems for Blood Velocity Estimation,” in *Acoustical Imaging*, Springer, Boston, MA, 1996, pp. 377–384.

[69] C. Demené *et al.*, “Spatiotemporal Clutter Filtering of Ultrafast Ultrasound Data Highly Increases Doppler and fUltrasound Sensitivity,” *IEEE Trans. Med. Imaging*, vol. 34, no. 11, pp. 2271–2285, Nov. 2015.

[70] N. B. Hamilton, D. Attwell, and C. N. Hall, “Pericyte-mediated regulation of capillary diameter: a component of neurovascular coupling in health and disease,” *Front. Neuroenergetics*, vol. 2, 2010.

[71] Urban, Alan, Brunner, Clément, Dussaux, Clara, Chassoux, Francine, Devaux, Bertrand, and Montaldo, Gabriel, “Functional Ultrasound Imaging of Cerebral Capillaries in Rodents and Humans,” *Acobs J. Mol. Transl. Med.*, Nov. 2015.

[72] P. H. J. Karten, *A Stereotaxic Atlas of the Brain of the Pigeon*. The Johns Hopkins University Press, 1967.

[73] E. Cohen, T. Deffieux, E. Tiran, C. Demene, L. Cohen, and M. Tanter, "Ultrasensitive Doppler based neuronavigation system for preclinical brain imaging applications," in *2016 IEEE International Ultrasonics Symposium (IUS)*, 2016, pp. 1–4.

[74] C. Demené *et al.*, "4D microvascular imaging based on ultrafast Doppler tomography," *NeuroImage*, vol. 127, pp. 472–483, Feb. 2016.

[75] J. Provost *et al.*, "3D ultrafast ultrasound imaging in vivo," *Phys. Med. Biol.*, vol. 59, no. 19, pp. L1–L13, Oct. 2014.

[76] O. Güntürkün, M. Verhoye, G. D. Groof, and A. V. der Linden, "A 3-dimensional digital atlas of the ascending sensory and the descending motor systems in the pigeon brain," *Brain Struct. Funct.*, vol. 218, no. 1, pp. 269–281, Jan. 2013.

[77] E. Jonckers, R. Delgado y Palacios, D. Shah, C. Guglielmetti, M. Verhoye, and A. Van der Linden, "Different anesthesia regimes modulate the functional connectivity outcome in mice," *Magn. Reson. Med.*, vol. 72, no. 4, pp. 1103–1112, Oktober 2014.

[78] P. S. Sharp *et al.*, "Comparison of stimulus-evoked cerebral hemodynamics in the awake mouse and under a novel anesthetic regime," *Sci. Rep.*, vol. 5, p. 12621, Jul. 2015.

[79] R. Merritt, C. Purcell, and G. Stroink, "Uniform magnetic field produced by three, four, and five square coils," *Rev. Sci. Instrum.*, vol. 54, no. 7, pp. 879–882, Jul. 1983.

[80] H. J. Hedrich, *The Laboratory Mouse*. Academic Press, 2012.

[81] M. A. Suckow, S. H. Weisbroth, and C. L. Franklin, *The Laboratory Rat*. Academic Press, 2005.

[82] G. De Groof, E. Jonckers, O. Güntürkün, P. Denolf, J. Van Auderkerke, and A. Van der Linden, "Functional MRI and functional connectivity of the visual system of awake pigeons," *Behav. Brain Res.*, vol. 239, pp. 43–50, Feb. 2013.

[83] R. F. Burton, "The scaling of eye size in adult birds: Relationship to brain, head and body sizes," *Vision Res.*, vol. 48, no. 22, pp. 2345–2351, Oktober 2008.

[84] P. K. Kuhl, "Early language acquisition: cracking the speech code," *Nat. Rev. Neurosci.*, vol. 5, no. 11, pp. 831–843, Nov. 2004.

[85] J. J. Bolhuis, G. G. O. Zijlstra, A. M. den Boer-Visser, and E. A. V. der Zee, "Localized neuronal activation in the zebra finch brain is related to the strength of song learning," *Proc. Natl. Acad. Sci.*, vol. 97, no. 5, pp. 2282–2285, Feb. 2000.

[86] Y. Mandelblat-Cerf, L. Las, N. Denisenko, and M. S. Fee, "A role for descending auditory cortical projections in songbird vocal learning," *eLife*, vol. 3, Jun. 2014.

[87] C. Poirier *et al.*, "A three-dimensional MRI atlas of the zebra finch brain in stereotaxic coordinates," *NeuroImage*, vol. 41, no. 1, pp. 1–6, May 2008.

[88] H.-J. Boele, S. K. E. Koekkoek, and C. I. De Zeeuw, "Cerebellar and Extracerebellar Involvement in Mouse Eyeblink Conditioning: the ACDC Model," *Front. Cell. Neurosci.*, vol. 3, Jan. 2010.

[89] M. M. ten Brinke *et al.*, "Evolving Models of Pavlovian Conditioning: Cerebellar Cortical Dynamics in Awake Behaving Mice," *Cell Rep.*, vol. 13, no. 9, pp. 1977–1988, Dec. 2015.

[90] R. Rau *et al.*, "Velocity vector in three dimensions using a high-frame-rate dual-transducer setup," in *2015 IEEE International Ultrasonics Symposium (IUS)*, 2015, pp. 1–4.

[91] E. G. Grant *et al.*, "Carotid Artery Stenosis: Gray-Scale and Doppler US Diagnosis—Society of Radiologists in Ultrasound Consensus Conference," *Radiology*, vol. 229, no. 2, pp. 340–346, Nov. 2003.

[92] M. Tanter, J. Bercoff, L. Sandrin, and M. Fink, "Ultrafast compound imaging for 2-D motion vector estimation: application to transient elastography," *IEEE Trans. Ultrason. Ferroelectr. Freq. Control*, vol. 49, no. 10, pp. 1363–1374, Oct. 2002.

[93] I. K. Ekroll, A. Swillens, P. Segers, T. Dahl, H. Torp, and L. Lovstakken, "Simultaneous quantification of flow and tissue velocities based on multi-angle plane wave imaging," *IEEE Trans. Ultrason. Ferroelectr. Freq. Control*, vol. 60, no. 4, pp. 727–738, Apr. 2013.

[94] V. L. Newhouse, D. Censor, T. Vontz, J. A. Cisneros, and B. B. Goldberg, "Ultrasound Doppler Probing of Flows Transverse with Respect to Beam Axis," *IEEE Trans. Biomed. Eng.*, vol. BME-34, no. 10, pp. 779–789, Oct. 1987.

[95] P. Tortoli, L. Bessi, and F. Guidi, "Bidirectional Doppler signal analysis based on a single RF sampling channel," *IEEE Trans. Ultrason. Ferroelectr. Freq. Control*, vol. 41, no. 1, pp. 1–3, Jan. 1994.

[96] B. F. Osmanski, G. Montaldo, and M. Tanter, "Out-of-plane Doppler imaging based on ultrafast plane wave imaging," *IEEE Trans. Ultrason. Ferroelectr. Freq. Control*, vol. 62, no. 4, pp. 625–636, Apr. 2015.